

AD 737282

**BEST
AVAILABLE COPY**

UNCLASSIFIED

3200.8 (Att 1 to Encl 1)
Mar 7, 66

Security Classification

DOCUMENT CONTROL DATA - R & D

(Security classification of title, body of abstract and indexing annotation must be entered when the overall report is classified)

1. ORIGINATING ACTIVITY (Corporate author) Marine Minerals Technology Center (U.S. Dept. of Commerce) 3150 Paradise Drive, Tiburon, Ca. 94920		2a. REPORT SECURITY CLASSIFICATION Unclassified	
3. REPORT TITLE Geological Prediction: Developing Tools and Techniques for Geophysical Identification and Classification of Sea-Floor Sediments		2b. GROUP N/A	
4. DESCRIPTIVE NOTES (Type of report and inclusive dates) Annual Report, January 19 through October 19, 1971			
5. AUTHOR(S) (First name, middle initial, last name) Burton B. Barnes Robert F. Corwin John T. Beyer T. G. Hildenbrand			
6. REPORT DATE January 1972		7a. TOTAL NO. OF PAGES x1, 202 202	7b. NO. OF REFS 76
8a. CONTRACT OR GRANT NO. H0210016		9a. ORIGINATOR'S REPORT NUMBER(S) NOAA TR ERL 224-MMTC 2	
8b. PROJECT NO.		9b. OTHER REPORT NO(S) (Any other numbers that may be assigned this report)	
10. DISTRIBUTION STATEMENT DDC REF 94 1977 UNCLASSIFIED		DISTRIBUTION STATEMENT A Approved for public release; Distribution Unlimited	
11. SUPPLEMENTARY NOTES This contract was monitored by the U. S. Bureau of Mines		12. SPONSORING MILITARY ACTIVITY Advanced Research Project Agency Dept. of Defense Washington, D. C. 20301	
13. ABSTRACT The experiments described in this report were developed to test and evaluate prototype tools and advanced techniques to predict geologic conditions on the sea floor. Emphasis has been placed on determining the mass physical properties of sea-floor sediments and rocks using geophysical tools for the identification of associated parameters. A direct current resistivity system, fashioned after the land-oriented Wenner array, was successfully developed. It has been shown, through theoretical studies, that it is feasible to use electromagnetic sounding to measure conductivity and thereby deduce porosity at shallow depths below the sea floor-water interface. A seismic shear wave generator prototype tool was built and successfully tested to produce the transverse wave form in saturated marine sediments. The reflectivity experiment to classify sea-floor sediments, by a ship underway, has verified previous field measurements by Breslau (1967) and others. A relatively high degree of correlation links acoustic absorption (bottom loss) to parameters of porosity, density, median grain size, fine-grained sediment types (silt and clay) and sorting coefficients. These parameters are shown to have a decided interdependence, and more importantly, prove necessary information for practical application to engineering problems relating to underwater tunneling operations and/or excavation of the sea floor.			

DD FORM 1473
1 NOV 65

UNCLASSIFIED

Security Classification

**U.S. DEPARTMENT OF COMMERCE
National Oceanic and Atmospheric Administration
Environmental Research Laboratories**

**GEOLOGIC PREDICTION: DEVELOPING TOOLS
AND TECHNIQUES FOR THE GEOPHYSICAL IDENTIFICATION
AND CLASSIFICATION OF SEA-FLOOR SEDIMENTS**

**Burton B. Barnes, Principal Investigator
(Telephone: 415 435-3145)
Robert F. Corwin, Project Engineer
John H. Beyer, Jr., Project Engineer
T. G. Hildenbrand, Project Engineer
(Telephone: 415 435-3145)**

**Advanced Research Projects Agency
Purchase Order No. H0210016
Amount: \$45,000**

To be published as NOAA TR ERL 224-MMTC 2

**Boulder, Colorado
February 1972**



The Marine Minerals Technology Center does not approve, recommend, or endorse any proprietary product or proprietary material mentioned in this publication. No reference will be made to the Marine Minerals Technology Center or to this publication furnished by the Marine Minerals Technology Center in any advertising or sales promotion which would indicate or imply that the Marine Minerals Technology Center approves, recommends or endorses any proprietary product or proprietary material mentioned herein, or which has as its purpose an intent to cause directly or indirectly the advertised product to be used or purchased because of this Marine Minerals Technology Center publication.

The views and conclusions contained in this document are those of the authors and should not be interpreted as necessarily representing the official policies, either expressed or implied, of the Advanced Research Projects Agency or the U. S. Government.

TABLE OF CONTENTS

	Page
ABSTRACT	v
1. INTRODUCTION	1
2. DETERMINATION OF SEDIMENT PROPERTIES BY ELECTRICAL METHODS	4
2.1 Relationship Between Electrical Resistivity and Other Properties of Marine Sediments	4
2.2 The Effect of Sulfate Ion Removal on the Conductivity of Seawater	6
2.3 Resistivity Meter for Seawater and Unconsolidated Sediment Samples	15
2.3.1 Description	15
2.3.2 Use of Marine Sediment Resistivity Meter for Resistivity-Porosity Correlations	20
2.3.2 Experimental Results: Analysis of Dolomite and Silica Sands	21
2.4 Initial Analysis of a Marine Electromagnetic Sounding System	31
2.4.1 System Description	32
2.4.2 Analysis	32
2.4.3 Conclusions	36
2.5 Resistivity Measurement by Direct Current Methods	36
2.5.1 Well Logging Method	37
2.5.2 Horizontal Array Method	39
2.5.3 Conclusions and Recommendations	61
3. DETERMINATION OF SEDIMENT PROPERTIES BY ACOUSTIC METHODS	62
3.1 Refraction Methods	62
3.1.1 Relationship Between Seismic Parameters and Other Soil Properties	62
3.1.2 Experimental Methods	62
3.1.3 Viscoelastic Model	64
3.1.4 Time-Distance Curves	65
3.1.5 Experimental Results	72
3.1.6 Data Acquisition and Results	77
3.1.7 Conclusions and Recommendations	92
3.2 Classification of Sea-Floor Sediments by a Ship Underway	95
3.2.1 Concept	95
3.2.2 Procedure	96
3.2.3 Previous Investigations	97

	Page
3.2.4 Theory Developed	98
3.2.5 Description of Geophysical Instrumentation and Equipment	105
3.2.6 Sediment Sampling Equipment	128
3.2.7 Research Vessel	134
3.2.8 Field Operations	136
3.2.9 Data Analysis	143
3.2.10 Results and Conclusions	146
4. ACKNOWLEDGEMENTS	152
5. REFERENCES	153
APPENDIX	159
A-1 Data for Resistivity vs Porosity Measurements	159
A-2 Calculation of the Potential Field Due to a Point Source of Current Over a Two-Layered Sea Floor	162
A-2-1 Introduction	162
A-2-2 General Solution	164
A-2-3 Particular Solution	165
A-2-4 Deep Water, Single Layer Approximation	168
A-2-5 Computer Solution	170
A-3 Relationships for Viscoelastic Model	172
A-3-1 Notation Summary	172
A-3-2 Measured Parameters	173
A-3-3 Sediment Properties	174
A-4 Derivations of Rayleigh Reflection Coefficient Equations and Bottom Loss	176
A-5 Core Site Locations	180
A-6 Sediment Sample Processing Summary and Related Acoustic Data	182

ABSTRACT

The experiments described in this report were developed to test and evaluate prototype tools and advanced techniques to predict geologic conditions on the sea floor. Emphasis has been placed on determining the mass physical properties of sea-floor sediments and rocks using geophysical tools for the identification of associated parameters. A direct current resistivity system, fashioned after the land-oriented Wenner array, was successfully developed. It has been shown, through theoretical studies, that it is feasible to use electromagnetic sounding to measure conductivity and thereby deduce porosity at shallow depths below the sea floor-water interface. A seismic shear wave generator prototype tool was built and successfully tested to produce the transverse wave form in saturated marine sediments. The reflectivity experiment to classify sea-floor sediments, by a ship underway, has verified previous field measurements by Breslau (1967) and others. A relatively high degree of correlation links acoustic absorption (bottom loss) to parameters of porosity, density, median grain size, fine-grained sediment types (silt and clay) and sorting coefficients. These parameters are shown to have a decided interdependence, and more importantly, provide necessary information for practical application to engineering problems relating to underwater operations and/or excavation of the sea floor.

LIST OF FIGURES

Figure		Page
2-1	Conductivity of Seawater Versus Percent $\text{SO}_4^{=}$ Removed, including the Effects of Dilution	14
2-2	Instrument for Measuring the Conductivity of Seawater and Unconsolidated Sediment Samples	17
2-3	Formation Factor vs Porosity for Dolomite Sand	23
2-4	Formation Factor vs Porosity for Ottawa Sand	24
2-5	Dolomite Particles	25
2-6	Conductivity of Sediment vs Conductivity of Interstitial Water	27
2-7	Formation Factor vs Porosity for Quartz Sand	28
2-8a,b	Formation Factor vs Porosity for Dolomite Sand	29, 30
2-9	Horizontal Magnetic Field vs Frequency	35
2-10	Well Logging Probe Used to Measure Resistivity of Marine Sediments	38
2-11	Wenner Resistivity Array on Land	40
2-12	Wenner Resistivity Curves for a 3-Layer Model	42
2-13	Surface and Sea-Floor Wenner Arrays	43
2-14	$\Delta V/I$ vs a for a Surface and a Bottom Wenner Array	47
2-15	$\Delta V/I$ vs a for a Bottom Wenner Array, with Varying Basement Depth and Resistivity	48
2-16	Square Wave Current Source	50
2-17	High Impedance Rectifying Voltmeter	51
2-18	Field Test Arrangement for 20-centimeter Wenner Array	53
2-19	Test Site for Resistivity Experiment	54
2-20	$\rho_{\text{sed}}/\rho_{\text{water}}$ vs $\Delta V/I$ for $h \gg a$ and $a=20$ cm	55
2-21	Towed Array Field Test	57
2-22	Non-polarizing Silver-Silver Chloride Electrode	58

Figure	Page
2-23 ΔV between potential electrodes, $I=0$ amps	59
2-24 ΔV between potential electrodes, $I=5.4$ amps	60
3-1 Theoretical time-distance graph for a source on the water surface and receiver on bottom	67
3-2 Theoretical time-distance graph for both source and receiver on bottom	68
3-3 Theoretical time-distance graph for S_H -source and receiver both on bottom	69
3-4 Two proposed seismic methods	71
3-5 Method of generating S_H -waves for experiments conducted on land	74
3-6 Marine S_H -source	76
3-7 Time-distance records from unconsolidated sand	78
3-8 Time distance records from unconsolidated sand	81
3-9 Time-distance records from beach experiments	82
3-10 Geophone records -- unconsolidated sand	83
3-11 Time-distance plots -- unconsolidated sand	84
3-12 Time-distance plots -- unconsolidated sand	86
3-13 Geophone records -- unconsolidated sand	88
3-14 Time-distance plots -- unconsolidated sand	89
3-15 Time-distance plots -- unconsolidated sand	90
3-16 Geophone output -- submarine sediments	91
3-17 Probe for measurement of shear wave and compressional wave velocity	94
3-18 Seafloor scattering - specular energy	99
3-19 Typical curves for bottom backscattering strength	100
3-20 Transmitted sound pulse	102

Figure	Page
3-21 Shipboard recording and sound source equipment	106
3-22 Shore station rack mounted reproducing equipment	107
3-23 Directional multiple electrode sound source	108
3-24 Raytheon Model DE-731 Precision Depth Recorder	110
3-25 Impulse Hydrophone and No. 1 Main Hydrophone Receiver Arrays	110
3-26 DMSS Unit and Impulse Hydrophone Receiver -- Tow Configuration	111
3-27 7-Channel Analog Tape Recorder (Ampex Model SP-300) and Receiver-Amplifier	113
3-28 No. 2 Main Hydrophone Array	113
3-29 Signal Wave Forms	118, 119
3-30 Shore-based Playback Console	120
3-31 Diver-Operated Corer (Retracted Position)	130
3-32 Diver-Operated Corer (Extended Position)	131
3-33 Core Retainer - Modified Shelby Tube	132
3-34 Diver-Operated Corer Piping Diagram	133
3-35 R/V DOODLEBUG	135
3-36 Block Diagram - Basic Navigation System and Subsystem	137
3-37 Hardware - Navigation Positioning System	138
3-38 San Francisco Bay Test Site - Proposed Program	139
3-39 San Francisco Bay Test Site - Actual Survey	140a
3-40 Diagram with Associated Bottom Loss Values (dB)	150
3-41 Bottom Sediments Composition - San Francisco Bay Test Area	151

LIST OF TABLES

Table		Page
2-1	Conductivity of Seawater with SO_4^{2-} Removed	8
2-2	Partial Equivalent Ionic Conductance of Major Ions in Seawater at 23°C , Assuming the Cation Transference Number of KCl in Seawater is 0.49	10
2-3	Calculation of Partial Equivalent Ionic Conductance of SO_4^{2-} in Seawater	11
2-4	Percentage Contribution of Major Ions in Seawater to its Overall Electrical Conductance at 35° and 23°C	12
2-5	Size Distribution for Sand Samples	21
2-6	Tortuosity Values	26
3-1	Wave Velocities in Unconsolidated Sand Using Refraction Unit	79
3-2	Results in Unconsolidated Sand Using Oscilloscope	85
3-3	Correlation between Bottom Loss and Sediment Grain Size	147
3-4	Correlation between Bottom Loss and Sediment Mass Physical Properties	149
3-5	Comparison of Correlative values -- MMTC vs Breslau (1967)	149

I. INTRODUCTION

This report is a compilation of investigations performed by four individuals working in two separate fields of endeavor. The overall project objective is to determine the mass physical properties of sea-floor sediments and rock types to predict the geological implications involved in excavation of the sea floor and subsurface tunneling. Studies are directed to defining the geophysical methods most applicable to the problem. The two fields of investigation encompass application of electrical and acoustical methods, and determining whether the tools and techniques representing these methods have application in a marine environment.

The in situ measurement of sea-floor properties, using electrical prospecting methods, has shown promise for determining varying conductivity within the near surface geologic section. The work described by J. H. Beyer and R. Corwin indicates that conductivity, as a function of depth, may be determined by direct current resistivity measurements and, according to Beyer, it is theoretically feasible to employ electromagnetic sounding to determine sediment conductivity. Corwin has further shown that land-oriented direct current resistivity tools may be modified for use in the marine environment.

Acoustic experiments in this report were designed and tested by T. Hildenbrand and B. Barnes. Hildenbrand's investigations included evaluation of mathematical models to ascertain whether shear waves could be generated and theoretically detected in saturated material. He developed a prototype instrument for generating shear waves to test

his theory. The results from field tests in marine environment confirm the presence of the transverse wave form.

Based on previous investigations, it has been proven that acoustic echoes reflected from the sea floor and substrata are influenced by the geologic nature of the media and, furthermore, it is reasonable to assume that the respective attenuation and energy loss may be correlated to parameters which depict the mass physical properties of sea-floor sediments. The work by Barnes consisted of a field exercise to verify this latter assumption and to apply the results to a practical engineering problem.

In each task of the overall project a systematic research approach was applied; first, with an inventory of previous work in the area followed by an analysis of the theories applied to a marine situation and last, where applicable, prototype development to test the feasibility for application. Much effort was made to personally consult prominent authorities with years of experience in each of the respective fields. These individuals are appropriately referenced in the text and the list of references.

The philosophy for first approaching the sea floor interface before considering the prediction of subbottom properties has resulted from a preliminary inventory of previous work accomplished to measure the properties of the sea floor and a knowledge of its practical application. It was discovered very early how little has actually been accomplished toward development of tools and techniques for making measurements of sea-floor sediments and rock. Several "firsts" in this regard have resulted from the effort to date. These are reported in detail in the text.

As research and development progresses, the objectives will be extended to include the lithologic variations of both consolidated and unconsolidated materials at depth as well as on the sea floor. The ability to predict the geologic situation in advance of borehole drilling and/or excavation of the ocean bottom and beneath the sea floor is the ultimate objective of each of the tasks described in this report.

2. DETERMINATION OF SEDIMENT PROPERTIES BY ELECTRICAL METHODS

2.1 Relationship Between Electrical Resistivity and Other Properties of Marine Sediments

Electrical conduction in saturated unconsolidated sediments occurs through the interstitial water, the mineral grains being several orders of magnitude more resistive. The resistivity is determined, then, mainly by the amount of water present, its salinity, and by the way the water is distributed through the sediment. The volume percentage of pore space, or porosity ϕ of the material determines the maximum amount of water which can be present. Thus, in a saturated sediment the resistivity is primarily a function of the salinity of the interstitial water. In order to compare the resistivities of various samples it is necessary to normalize the values. This generally is done by calculating the formation factor, F (Archie, 1942), where

$$F = \frac{\text{bulk resistivity of sample}}{\text{resistivity of interstitial water}} = \frac{\rho_s}{\rho_w}$$

Kullenberg (1952) showed that for some deep-sea sediments the difference in salinity between the interstitial water in the sediments and the bottom water is, on the whole, rather small, so that ρ_w is easily obtainable.

The formation factor is a complex function of grain-size distribution, grain shape, packing arrangement (see Section 2.3.3), and the degree of cementation; or looked at in another sense, formation factor is a function of porosity, permeability, and capillarity (Schopper, 1966), all of which determine the manner by which electrical current passes through

the material. In unconsolidated sediments the pore spaces are well interconnected so that the formation factor is primarily dependent upon porosity.

An empirical relationship between formation factor and porosity has been developed by Archie (1942):

$$F = \phi^{-m}$$

where he believed m to be a function of cementation. However, Erchui and Nacci (1971) have demonstrated that for clean laboratory samples m ranges from 1.6 for sand to 3.28 for sodium montmorillonite. In measuring unconsolidated marine sediments Kermabon et al. (1969) have found a more limited range:

$$m = 1.8 \text{ to } 2.0.$$

Wyllie and Gregory (1953) demonstrated that Archie's Law should be modified to

$$F = a\phi^{-m}$$

where a , an empirical constant in the range 0.4 to 1.4, is a measure of the effective path length through the material. In unconsolidated marine sediments the constant a is near unity.

Thus it appears that a knowledge of the formation factor of an unconsolidated marine sediment could yield a reliable estimate of porosity. From 2,500 measurements made on ocean bottom cores, Kermabon et al. (1969) display data indicating that the formation factor is sufficient to predict porosity to ± 6 percent. Porosity, or alternatively void ratio, e , where

$$e = \frac{\phi}{1 - \phi}$$

is quite useful for estimating engineering properties of sediments. For example, in some experiments with clay samples Vees and Winterkorn (1967) demonstrated an inverse straight line relationship between the logarithm of shear strength and the void ratio.

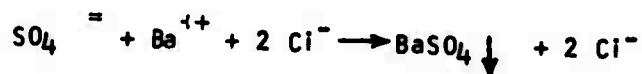
On the basis of empirical analyses of unconsolidated marine sediments it is apparent that porosity can be well correlated with other properties of the material. Hamilton (e.g., 1970a, 1970b) has derived regression equations which describe low scatter plots of porosity versus bulk density, acoustic impedance, the product of density times velocity squared, Rayleigh Reflection Coefficient, and bottom loss. Hamilton's (1970a) data also demonstrate a loose correlation between porosity and mean grain diameter.

2.2 The Effect of Sulfate Ion Removal on the Conductivity of Seawater

As has been discussed above, the resistivity of unconsolidated marine sediments is very highly dependent upon the resistivity of the interstitial water. If resistivity measurements are to be made for the purpose of determining the porosity of the sediments it is necessary to know whether or not the resistivity of the interstitial water is liable to deviate significantly from that of the overlying bottom water. One facet of this problem deals with compositional changes of the interstitial water with time. As a result of interaction of the interstitial water with the mineral grains and plant and animal life in the sediment, ions will be selectively added to or removed from the water. This will alter the ionic concentrations and therefore the resistivity of the interstitial water.

An experiment has been conducted to determine the effect upon the electrical conductivity (the inverse of resistivity) of seawater of the removal of the sulfate ion. Of the ions in standard seawater, sulfate has the fourth highest concentration, following chlorine, sodium, and magnesium.

Artificial seawater was made according to the recipe of Lyman and Fleming (1940), and was found to have a salinity of 34.87 parts per thousand using a Hysch Portable Laboratory Salinometer to measure conductivity, and the International Oceanographic Tables (1966) to calculate salinity from conductivity. An aqueous solution of barium chloride was used to precipitate the sulfate ion from the sea water as barium sulfate:



The BaCl_2 solution was made to have a Cl^- concentration the same as that of the artificial seawater so that with the addition of the BaCl_2 solution, the Cl^- concentration of the seawater remained unchanged. Assuming that the seawater was Dittmarian, the Cl^- concentration was found from Wilde (1969, p. 62) to be 0.544 formal. The BaCl_2 solution was, then, 0.272 formal in Ba^{++} concentration, or 0.284 molal, based upon an experimentally determined density of 1.045 g/cm^3 .

The SO_4^{2-} concentration in the seawater was 0.0281 formal (Wilde, 1969, p. 63), which is 0.0288 molal for a density of 1.024 g/cm^3 . Thus, to precipitate all the SO_4^{2-} from the seawater as BaSO_4 it was necessary to titrate the seawater with BaCl_2 solution at a ratio of

$$\frac{0.0288 \text{ mole/liter of seawater}}{0.284 \text{ mole/liter of BaCl}_2 \text{ soln}} = 0.1014 \frac{\text{liter of BaCl}_2 \text{ soln.}}{\text{liter of seawater}}$$

Individual samples of the seawater were titrated with different quantities of the BaCl_2 solution such that, respectively, 20, 40, 60, 80, and 100 percent of the $\text{SO}_4^{=}$ would be precipitated. The treated seawater samples were then filtered and the conductivity was measured. The data are shown in Table 2-1. The conductivity ratios were reproducible to within 0.3 percent for all samples.

The addition of the BaCl_2 solution to the seawater has two distinct effects: it significantly reduces the $\text{SO}_4^{=}$ concentration by precipitation, and, to a much lesser degree, it reduces the concentrations of all the other ions, except Cl^- , by dilution.

Table 2-1.--Conductivity of seawater with $\text{SO}_4^{=}$ removed.

Percent $\text{SO}_4^{=}$ removed	Conductivity ratio	Conductivity (mho/cm)
0	0.987	0.0472
20	0.966	0.0462
40	0.944	0.0451
60	0.955	0.0456
80	0.926	0.0443
100	0.939	0.0449

The effects of dilution of these ions can be seen by considering the equivalent conductance, Λ , where

$$\Lambda = \frac{\sigma}{\text{equivalents/cm}^3}$$

and σ is the electrical conductivity. As is described by Tobias (1970), the equivalent conductance of an electrolyte at infinite dilution, Λ_0 , depends upon the contributions from each of the ionic species present, so

$$\Lambda_0 = \Lambda_0^+ + \Lambda_0^-$$

where Λ_0^+ and Λ_0^- are, respectively, the summed conductances of the cations and anions at infinite dilution. Seawater is a complex concentrated solution, but clearly, as the ionic concentrations are reduced by dilution the conductivity will decrease. This is demonstrated by the data in Table 2-1.

The increase in conductivity which was observed in proceeding from 80 to 100 percent removal of $\text{SO}_4^{=}$ could result from the addition of BaCl_2 solution beyond the point of total $\text{SO}_4^{=}$ removal. In this eventuality Ba^{++} ions would remain in solution, with the tendency to increase the conductivity.

The anomalous increase in conductivity at 60 percent removal of $\text{SO}_4^{=}$ is difficult to interpret. Assuming that it is real, and not the result of an error in the laboratory, the explanation must be that the ratios of the complexes of $\text{SO}_4^{=}$ in seawater vary peculiarly in this concentration.

Based upon an extrapolation of work done by Longworth (1932) on the cation transference number $\frac{1}{2}$ of KCl, Park (1964) calculated the partial equivalent conductance, $\bar{\Lambda}$, of major ions in seawater. The results are shown in Table 2-2. (Park defined equivalent conductance in terms of cm^2/ohm rather than $\text{cm}^2/\text{ohm-equivalent}$. A thorough

Table 2-2.^{2/} -- Partial equivalent ionic conductance of major ions in seawater at 23°C, assuming the cation transference number of KCl in seawater is 0.49.

Cation	$\bar{\Lambda}^+$	Anion	$\bar{\Lambda}^-$
Na^+	31	Cl^-	59
K^+	57	$\frac{1}{2}\text{SO}_4^{=}$	21
$\frac{1}{2}\text{Mg}^{++}$	13	HCO_3^-	15
$\frac{1}{2}\text{Ca}^{++}$	19	Br^-	63
$\frac{1}{2}\text{Sr}^{++}$	21	$\frac{1}{2}\text{CO}_3^{=}$	-8

discussion of the significance of this detail is given by Connors and Park, 1967). Park explained the negative conductance value for $\text{CO}_3^{=}$ as resulting from complexing of this ion with some cations in seawater, and he obtained his values for the degree of complexing from Garrels and Thompson (1962). Yet Park did not discuss the complexing of $\text{SO}_4^{=}$, also described by Garrels and Thompson. Table 2-3 displays an analysis

^{1/} The transference number, t , of an ion is the fraction of current carried by that ion.

$$t_i = \frac{c_i z_i u_i}{\sum_j c_j z_j u_j}$$

where c is the concentration, z is the valence, and u is the mobility.

^{2/} From Park (1964, p. 734).

of $\text{SO}_4^{=}$ similar to that performed by Park for $\text{CO}_3^{=}$, and demonstrates that as a result of complexing, the effect of $\text{SO}_4^{=}$ on the conductance of seawater should be almost negligible. However, this is not in accord with the value Park computed for Table 2-2 and has apparently been disregarded.

Table 2-3.-- Calculation of partial equivalent ionic conductance of $\text{SO}_4^{=}$ ion in seawater.

Dissolved species	Composition ^{3/} (Percent)	Equivalent conductance ($\Omega^{-1} \text{ cm}^2$)	Contribution to overall conductance ($\Omega^{-1} \text{ cm}^2$)
$\text{SO}_4^{=}$	54	21	+ 11.
CaSO_4	3	19 for $\frac{1}{2}$ Ca	- 0.5
MgSO_4	21.5	13 for $\frac{1}{2}$ Mg	- 3.
Na_2SO_4	21	31 for $\frac{1}{2}$ Na	- 6.5
Total			+ 1.

Park continued by calculating the contribution of major ions to the overall conductivity of seawater. This information is shown in Table 2-4.

^{3/} From Garrels and Thompson (1962).

Table 2-4.^{4/} --Percentage contribution of major ions in seawater to its overall electrical conductance at 35% and 23°C.

Ion	Equivalent/liter ^{5/}	Weight (%)	Conductance(%)
Na ⁺	0.483	30.7	29.
Mg ⁺⁺	0.109	3.7	2.7
Ca ⁺⁺	0.021	1.2	0.77
K ⁺	0.010	1.1	1.1
Sr ⁺⁺	0.0001	0.0	0.004
Cl ⁻	0.558	55.2	64.
SO ₄ ⁼	0.057	7.7	2.3
HCO ₃ ⁻	0.002	0.1	0.06
Br ⁻	0.001	0.2	0.12

If, in spite of the discrepancy mentioned above, these values are assumed to be correct, they can be used to calculate the decrease in conductivity of the seawater which would be expected from the addition of the BaCl₂ solution.

^{4/} From Park (1964, p. 735).

^{5/} From Harvey (1960, p. 4).

For 100 percent precipitation of $\text{SO}_4^{=}$, the contribution of this ion becomes zero. The other ions, except for Cl^- , undergo a dilution of 10 percent. These ions, which account for 33.7 percent of the conductivity of seawater, have their combined effect reduced to 30.3 percent. This means that for the unchanged value for Cl^- , 64 percent, the conductivity of the seawater should be reduced to 94.3 percent of its initial value upon the addition of the BaCl_2 solution. With all $\text{SO}_4^{=}$ removed, the treated seawater should have a conductivity of 0.0445 mho/cm.

Computations similar to this for lesser quantities of BaCl_2 solution added to seawater would yield conductivities along the dashed line in figure 2-1. This analysis agrees very well with the experimental data.

It must be noted, however, that at least 60 percent of the reduction in conductivity is due to the dilution of the seawater sample, while less than 40 percent is due to the removal of the sulfate ion. The removal of the sulfate ion alone would reduce the conductivity from 0.0472 to 0.0463 mho/cm, a change of 2 percent, which is in agreement with the theoretically obtained value given by Park (1964) in table 2-4. A change in conductivity of 2 percent is well within the range of error of virtually all electromagnetic and resistivity systems, including resistivity probes, and is therefore insignificant. Thus, it is apparent from table 2-4, that ionic replacement of only chloride and sodium is liable to result in substantive changes of marine sediment pore water resistivity. This means that a probe designed to selectively measure the concentrations of only chloride and sodium ions would yield sufficiently accurate information for the calculation of pore water resistivity.

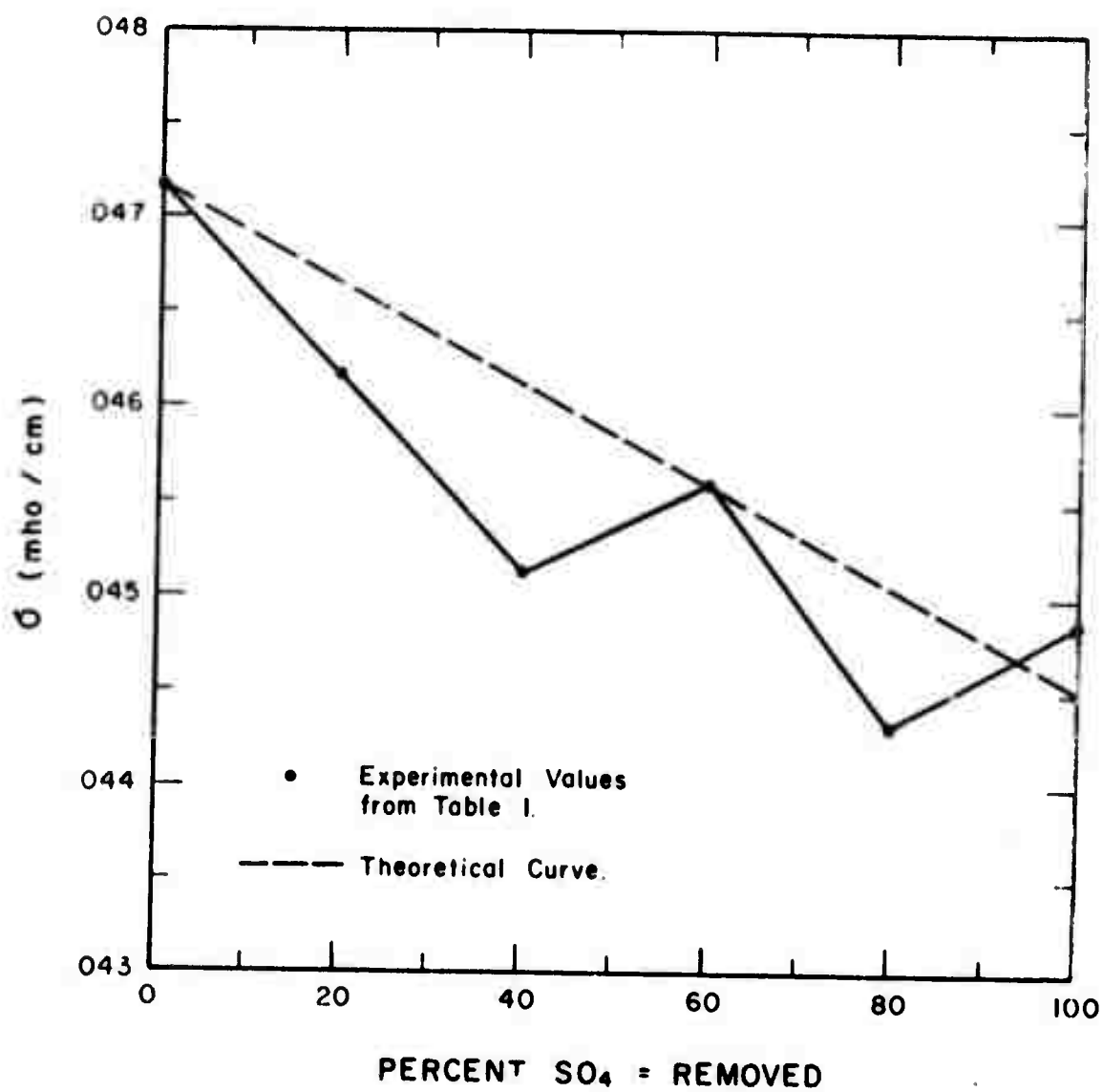


Figure 2-1. Conductivity of sea water vs. percent SO_4 removed, including the effect of dilution.

2.3 Resistivity Meter for Seawater and Unconsolidated Sediment Samples

2.3.1 Description

A four electrode device has been constructed to measure the resistivity of seawater and unconsolidated saturated sediment samples. The sample is poured into a tube one inch in diameter and about one foot long containing the four equispaced electrodes. An electric current is forced through the sample between the two electrodes near the ends of the tube, and a resultant potential difference is measured between the two intermediate electrodes. The resistivity, ρ , of the sample is

$$\rho = K \frac{E}{I}$$

where

K = geometrical constant of the sample holder,

I = current introduced through the current electrodes,

E = voltage drop measured across the potential electrodes.

The term K is a constant for the sample holder, and the current I can be kept constant regardless of sample resistivity. Thus, the sample resistivity is proportional to the voltage drop seen across the potential electrodes. The instrument is calibrated (i.e., the term K/I is determined) on the basis of readings obtained using samples of known resistivity.

There are several criteria which should be met by the current generating and voltage detecting circuits. The current source should meet the following specifications:

1. Square wave output.
2. Constant current regardless of sample resistivity.
3. Current output in the range of 0.1 - 1.0 milliampere.
4. Output current independent of supply voltage to system.

Direct current cannot be used because the potential electrodes will eventually polarize, making the measured potential drop to that existing between the electrodes and the sample. Any a.c. signal could be employed but a square wave has the advantages that it is easy to produce, and when rectified, yields a signal which can easily be measured at low frequencies by a meter.

Figure 2-2 shows the circuit for the instrument. The square wave generator is described in the GE Transistor Manual (1964). It is a modification of a multivibrator circuit with the flip-flop action controlled by a unijunction. The frequency of the output can conveniently be changed by varying the resistance R_1 . With a supply voltage of ± 15 volts the square wave output oscillates between ± 10 volts.

The current, if kept constant regardless of the sample resistivity, does not enter into the determination of resistivity once the instrument has been calibrated, and therefore does not have to be monitored. Constant current is maintained by the circuit which includes operational amplifier 1. The current I in the feedback loop of the amplifier is determined by $I = e_i/R_1$, where e_i is the input voltage to the amplifier, and R_1 is noted in figure 2-2. The amplifier increases the output voltage e_o to whatever value is necessary to maintain the current I . The amplitude of this current, considering the dimensions of the sample

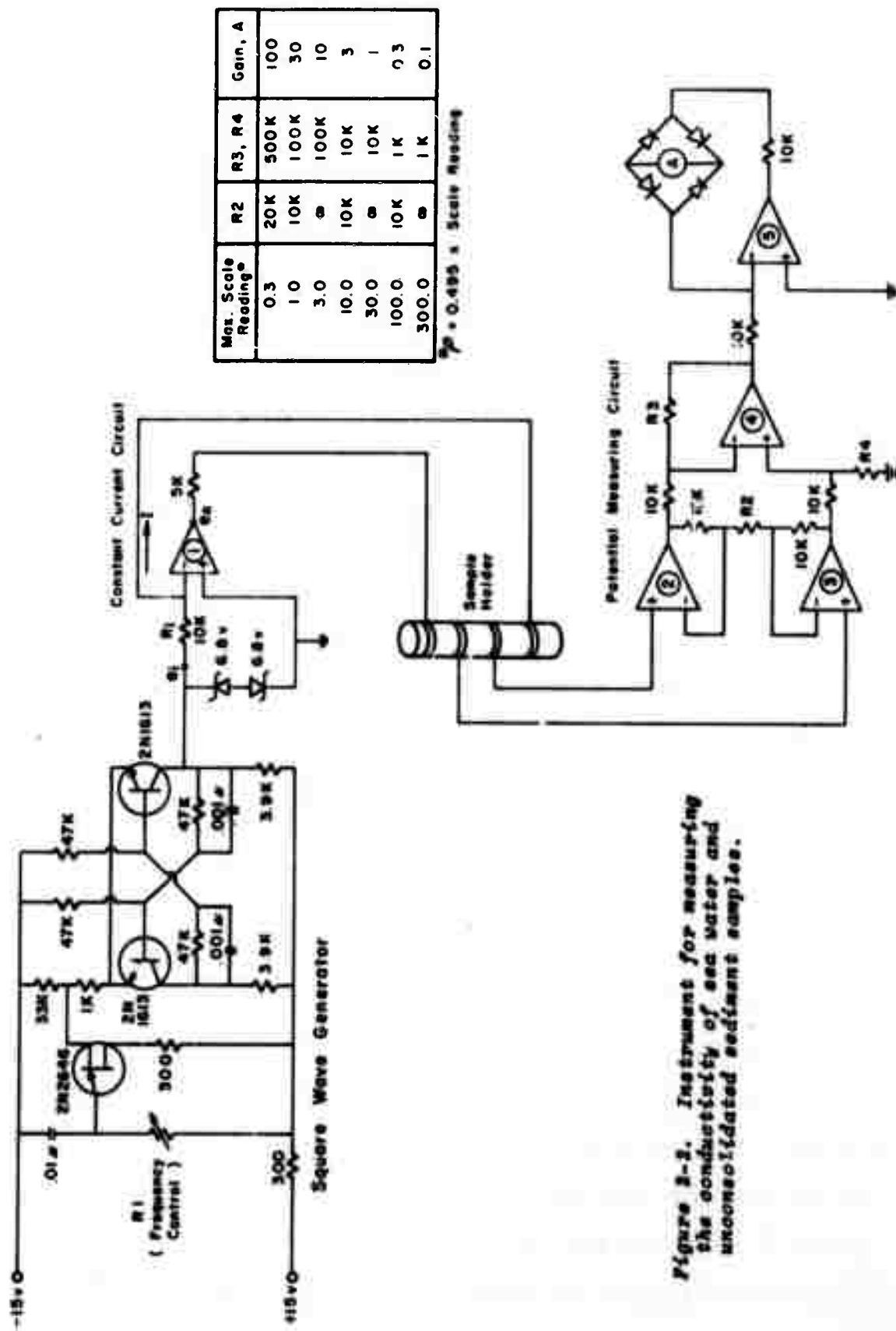


Figure 3-2. Instrument for measuring the conductivity of sea water and unconsolidated sediment samples.

holder, should be in the range of 0.1 to 1.0 milliamperes; below this range the output voltage is too low for reliable measurement of a seawater sample (< 1.0 millivolt), and above this amperage electrolysis of the water might occur, producing bubbles on the electrodes. The constant current circuit is set up to maintain a current of ± 0.68 milliamperes through the sample.

To make the current i independent of the supply voltage, two zener diodes are connected back-to-back across the output of the square wave generator. The amplitude of the output voltage of the square wave generator will vary with the supply voltage. For this reason, were it not for the zener diodes, the voltage e_i seen by the constant current circuit (and therefore the current i) would be dependent upon the supply voltage. The zener diodes maintain e_i constant at ± 6.8 volts for any supply voltage whose absolute value is greater than 10 volts.

Criteria which are important for the detection circuit across the potential electrodes are:

1. High input impedance.
2. Amplification of signal.
3. Common mode rejection.
4. Rectification of a.c. signal to d.c. for meter readout.

It is important that the input impedance of the potential measuring circuit be high so that the potential electrodes will draw virtually no current. This avoids polarization of the electrodes, which can result in potentials higher than the voltage drop across some samples. The potential electrodes are connected to operational amplifiers 2 and 3 (see figure 2-2), which are inexpensive and have input impedances of

2.5×10^7 ohms. At this impedance, frequencies down to 10 hz can be used without significant electrode polarization occurring. Operational amplifiers employing field effect input transistors would allow lower frequencies to be used.

Operational amplifier 4 is necessary for both amplification and common mode rejection; it takes the difference of the voltages of the two potential electrodes (after these voltages have been amplified by the previous stage). The gain, A, of the potential measuring circuit is

$$A = \left(1 + \frac{20,000}{R_2} \right) \times \left(\frac{R_3}{10,000} \right); \quad R_3 = R_4$$

and can be switched to different values as shown in the box in figure 2-2, depending upon sample resistivity.

The amplified voltage difference between the potential electrodes is the input to operational amplifier 5, which contains in its feedback loop, an ammeter in a diode bridge. The bridge circuit rectifies the square wave current flow so that it can be measured by the meter, and the reason for locating the diode bridge in the feedback loop of an operational amplifier is to force the diodes to act ideally. That is, the operational amplifier raises the voltage across the bridge circuit to a level such that the diodes will trigger and current will flow. As a result, very small voltage differences entering the common mode rejection circuit can be detected, and furthermore, the detection circuit is linear. The reading seen on the ammeter is proportional to the difference in potential of the potential electrodes and the resistivity of the sample.

To calibrate the resistivity meter, water samples with different resistivities were prepared and measured on a Hytech Portable Laboratory Salinometer. The resistivity meter proved to be quite linear, as designed; all known samples yielded calibration curves within 2 percent of each other over a range of 0.2 to 30 ohm-meters. For the sample holder presently being used, all scale readings must be multiplied by 0.495 to obtain the sample resistivity.

2.3.2 Use of Marine Sediment Resistivity Meter for Resistivity-Porosity Correlations

The sample holder is a one-inch diameter plastic tube containing four equispaced electrodes at separations of two inches. A field sample is poured into the vertically held tube for measurement. For laboratory experiments with regard to the resistivity of marine sediments as a function of porosity, the sample holder has been modified in the following way: a bottomless graduated cylinder (also, one-inch diameter) has been glued to the top as an extension. With this addition, the porosity of a sample in the holder can be determined simultaneously with the measurement of its resistivity.

Saline water, which will become the interstitial water in the sample, is poured into the sample holder, and its volume (that in the sample holder plus that extending into the graduated cylinder) is noted. At this point the resistivity of the water can be measured. Then the dry, clean (no salts) sample is slowly poured into the holder so as not to entrap air bubbles. The resulting change in water level in the graduated cylinder is the volume displaced by the sample. The position

Of the boundary between the top of the sediment and the clear water above yields the volume of saturated sediment. The porosity, ϕ , of a sediment sample is

$$\phi = \frac{\text{volume of void space}}{\text{volume of saturated sample}}.$$

Thus, the porosity of the sample in the holder is

$$\phi = 1 - \frac{\text{final volume of water and sediment} - \text{initial volume of water}}{\text{volume of saturated sediment}}$$

The resistivity can then be measured without disturbing the sample.

Tapping the sample holder, or shaking it with a mechanical vibrator, will tend to pack the sediment, thereby reducing the volume of the saturated sediment while the total volume of the sediment and water column remains unchanged. The porosity can again be calculated and a new resistivity measurement made.

2.3.3 Experimental Results: Analysis of Dolomite and Silica Sands

Using the resistivity instrument described in 2.3.1 and 2.3.2, resistivity and porosity measurements were performed on samples of well sorted Ottawa (silica) and dolomite sands of the size distributions given in table 2-5. The data is given in Appendix 4.1.

Table 2-5.--Size distributions for sand samples

	Mesh	Particle size in mm		
		Max.	min.	mean
Silica sand	35 x 48	0.420	0.297	0.354
	48 x 65	.297	.210	.251
	100 x 150	.149	.105	.125

Table 2-5 (cont'd)

	Mesh	Particle size in mm		
		max.	min.	mean
Dolomite sand	4 x 6	4.760	3.36	4.00
	9 x 10	2.00	1.68	1.83
	14 x 20	1.19	0.841	1.00
	65 x 100	0.210	0.149	0.177

Figures 2-3 and 2-4 show the formation factors of the samples plotted against porosity. As is to be expected, as the porosity of a sample is reduced, the resistivity increases.

In comparing figures 2-3 and 2-4, it is apparent that the Ottawa sand data is tightly grouped for all particle sizes, while the dolomite sand, for any given porosity, displays increasing resistivity as the particle size is reduced. (This phenomenon might be more easily viewed in figure 2-6 where porosity is held constant.) Figure 2-5 shows magnified photographs of the dolomite particles. Though the photographic reproduction is poor, it is obvious that the smaller particles are considerably more angular than the larger particles, suggesting that particle shape has an effect upon formation factor. This is reasonable because particle shape is a major factor in defining the configuration of pore space, and this determines the effective conduction path length, or tortuosity T , of the material. Tortuosity is related to formation factor and porosity as (Wyllie and Gregory, 1953)

$$T^2 = \phi \times F$$

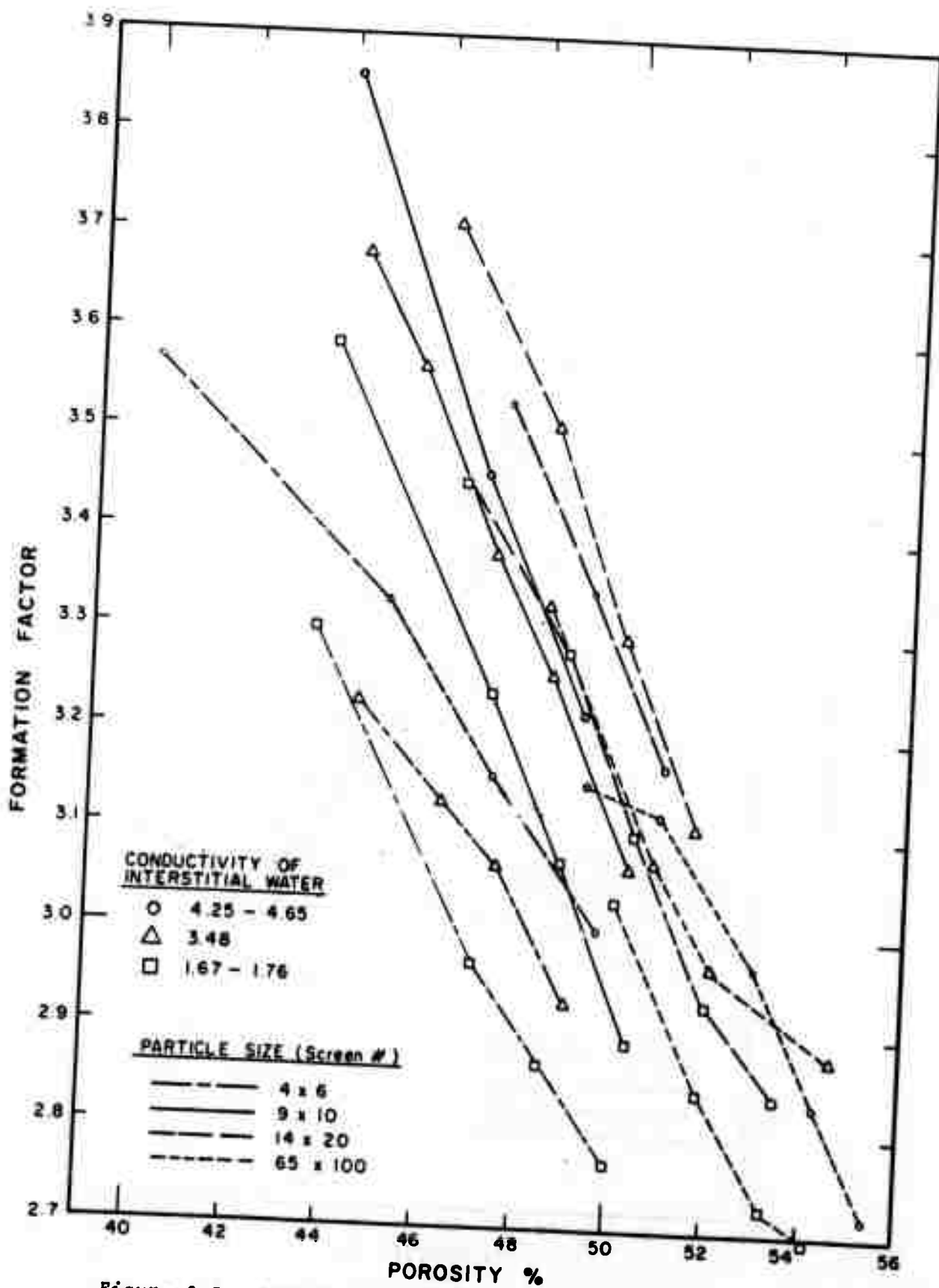


Figure 2-3. Formation factor vs. porosity for Dolomite sand.

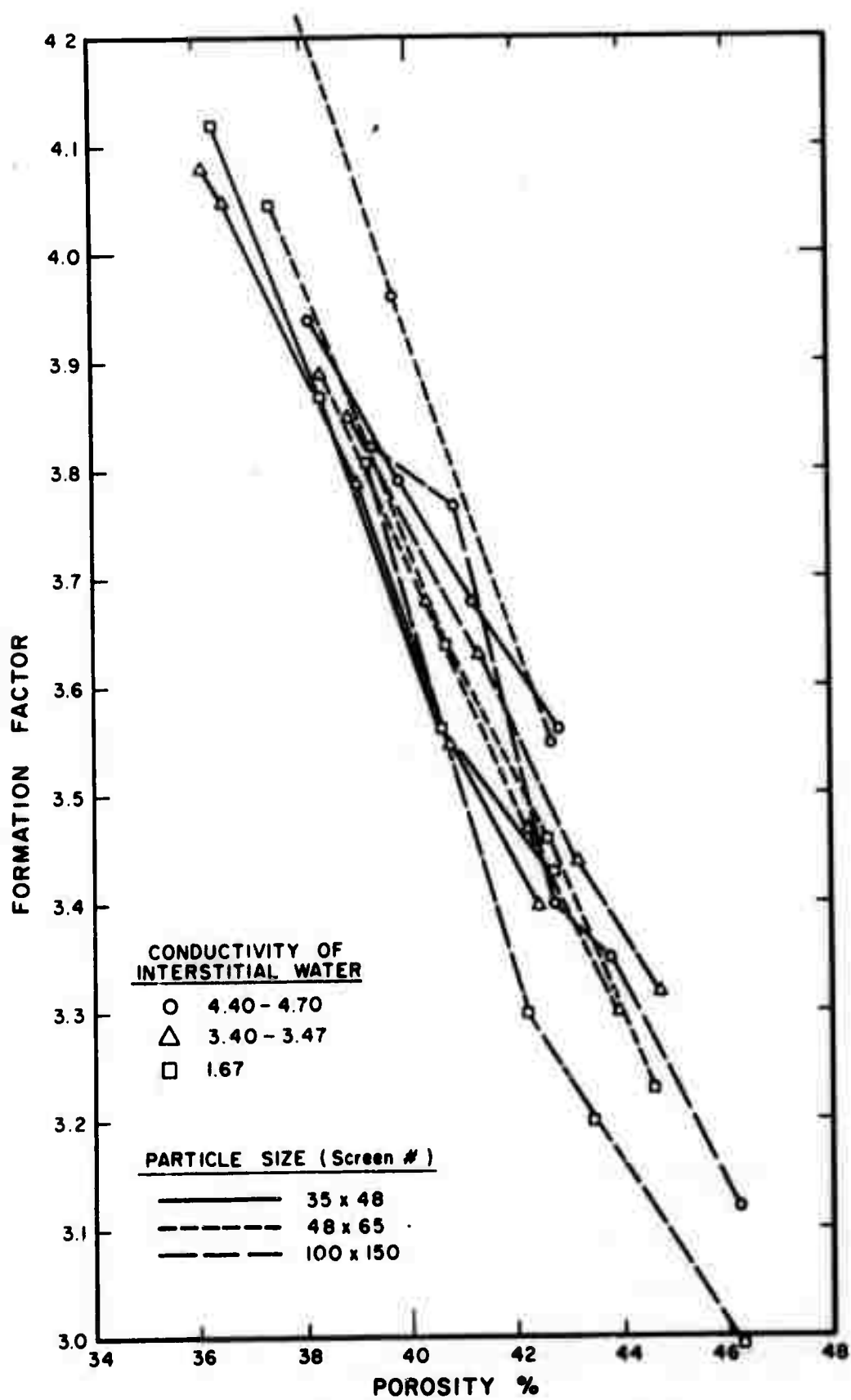
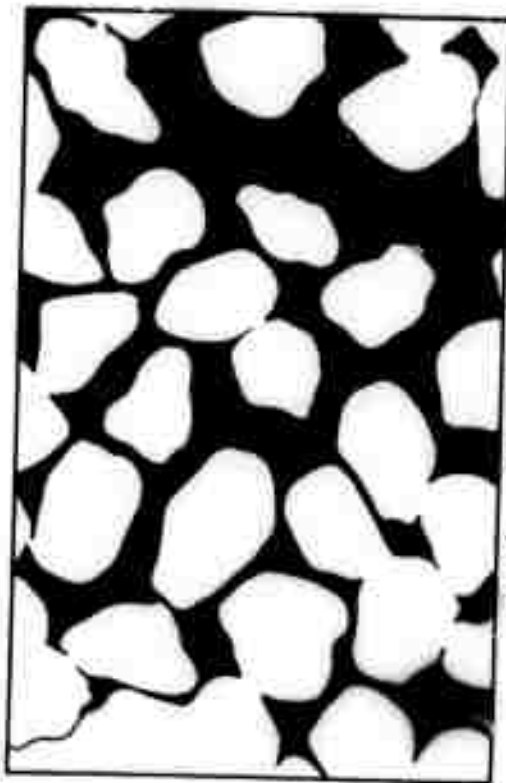
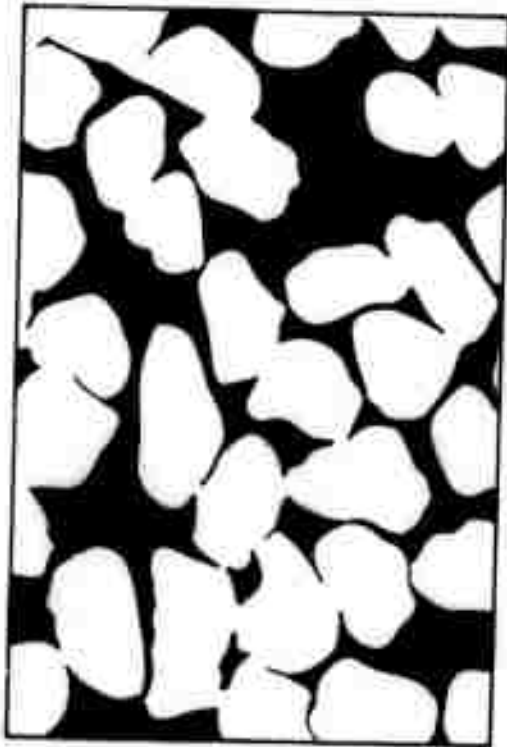


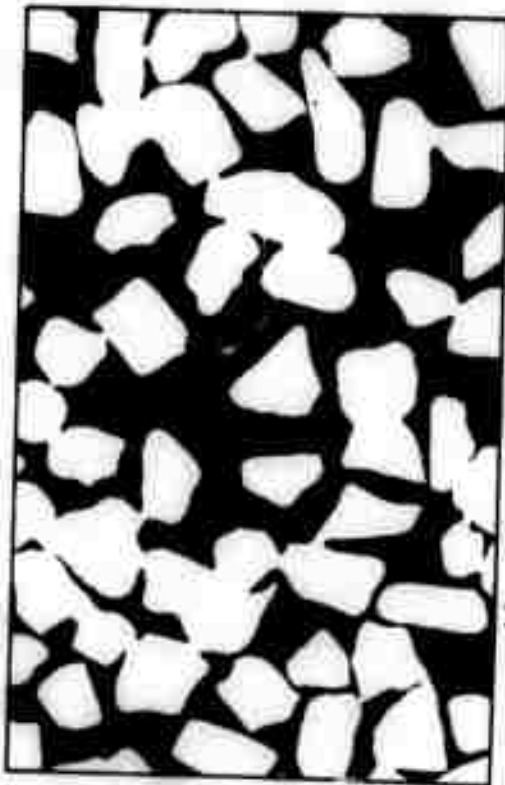
Figure 2-4. Formation factor vs. porosity for Ottawa sand.



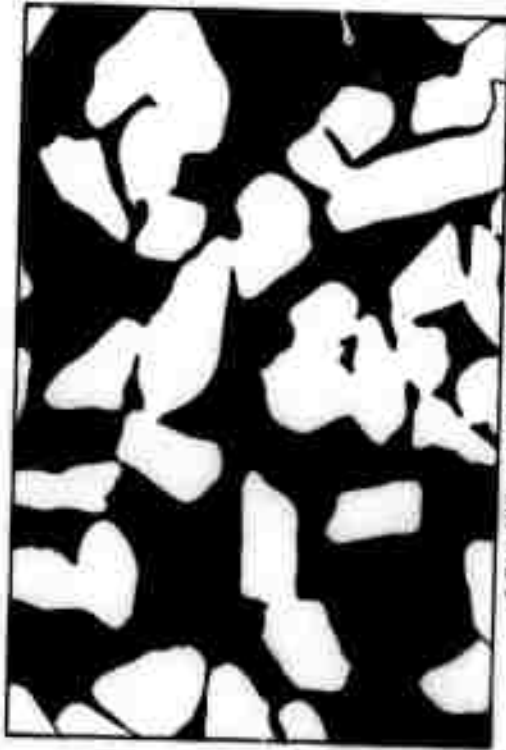
7 x 8 Magnification 4.5



9 x 10 Magnification 6.25



14 x 20 Magnification 7.5



48 x 65 Magnification

Figure 2-5. Dolomite particles.

The dolomite grains become increasingly angular as the particle size is reduced, so in packing the particles to a particular porosity, the tortuosity increases with decreasing grain size. The data displayed in figure 2-6 yields the values shown in table 2-6 for tortuosity.

Table 2-6.--Tortuosity values

	Mesh	ϕ	F	T
Dolomite sand	4 x 6	49	3.01	12.2
	9 x 10	49	3.22	12.6
	14 x 20	49	3.79	13.3
Silica sand	35 x 48	40	3.56	12.0
	48 x 65	40	3.80	12.3
	100 x 150	40	3.81	12.4

The fact that the silica sand yields tightly grouped curves in figures 2-4 and 2-6 and only a slight variation in tortuosity suggests that the different sizes of sand particles are of nearly the same shape.

In Archie's Law ($F = \phi^m$) the exponent m can be found by plotting the logarithm of formation factor versus the logarithm of porosity; m is the slope of the line defined by the data. Figures 2-7, 2-8a, and 2-8b show the data points collected for silica and dolomite, respectively. The data for the silica sand is well grouped about a line which indicates a value of m of about 1.3, which is the value obtained by several researchers for spheres (e.g., Wyllie and Gregory, 1953). This suggests that the grains of silica sand are well rounded for all the sizes tested.

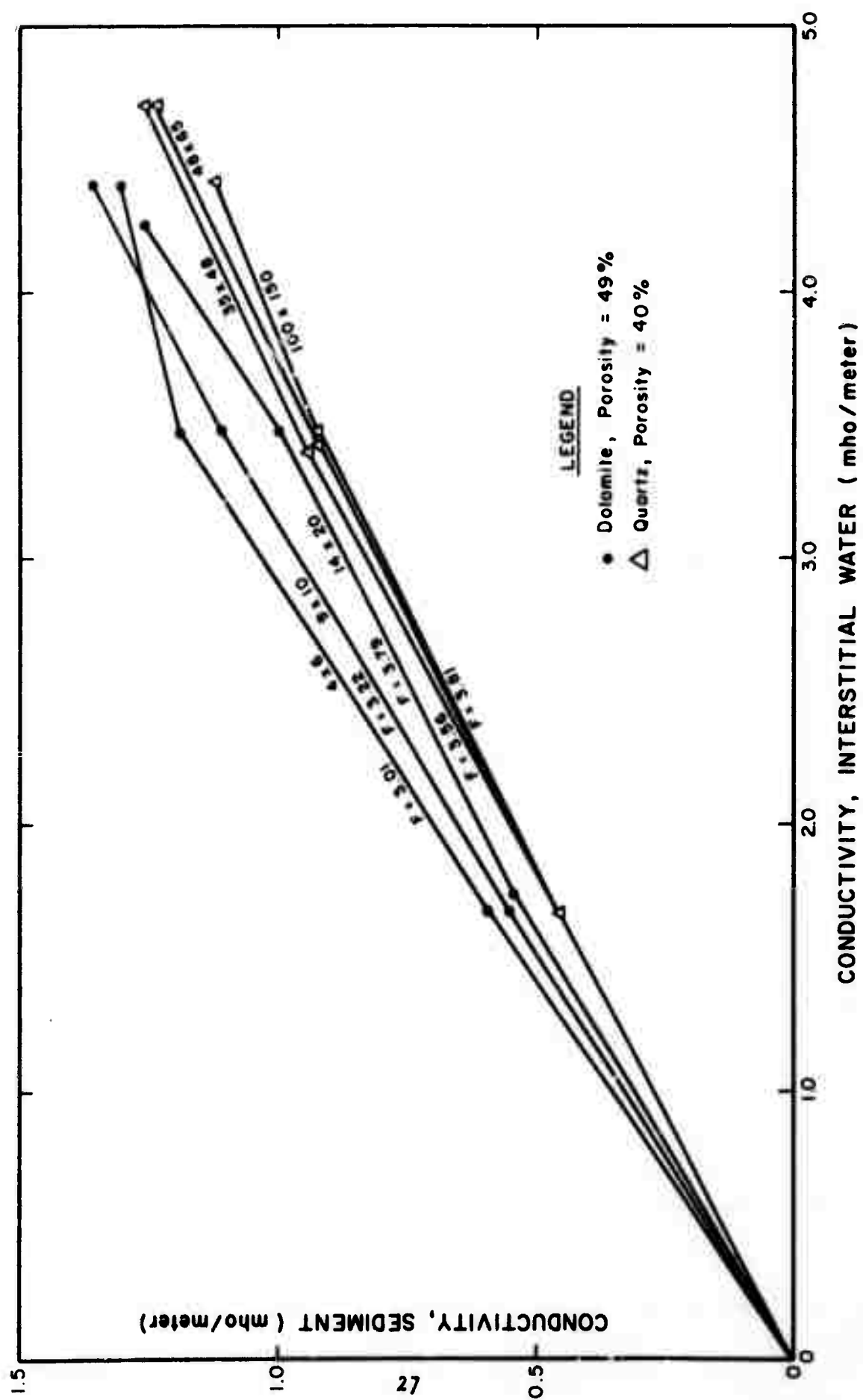


Figure 2-6. Conductivity of sediment vs. conductivity of interstitial water.

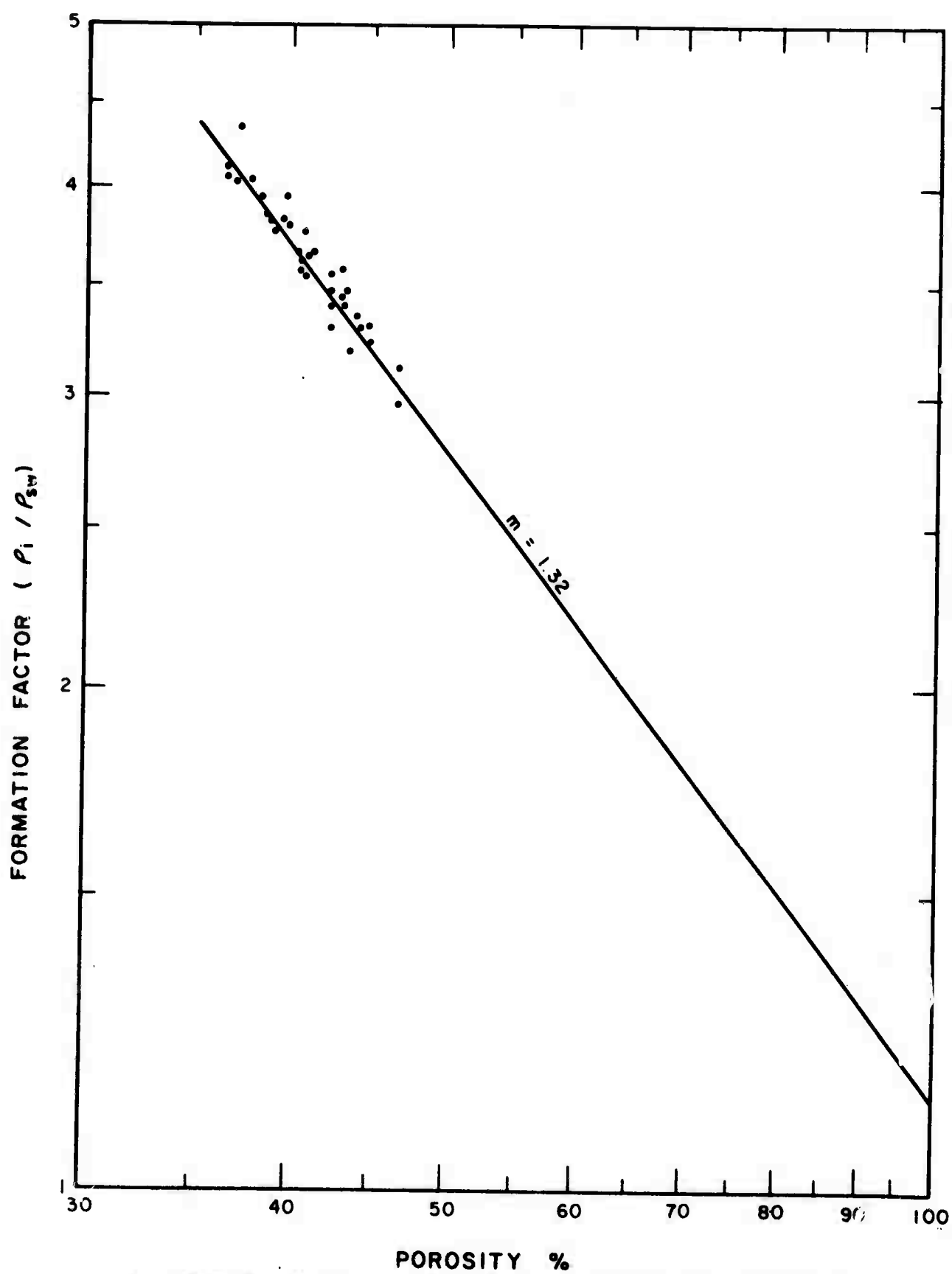


Figure 2-7. Formation factor vs. porosity for quartz sand.

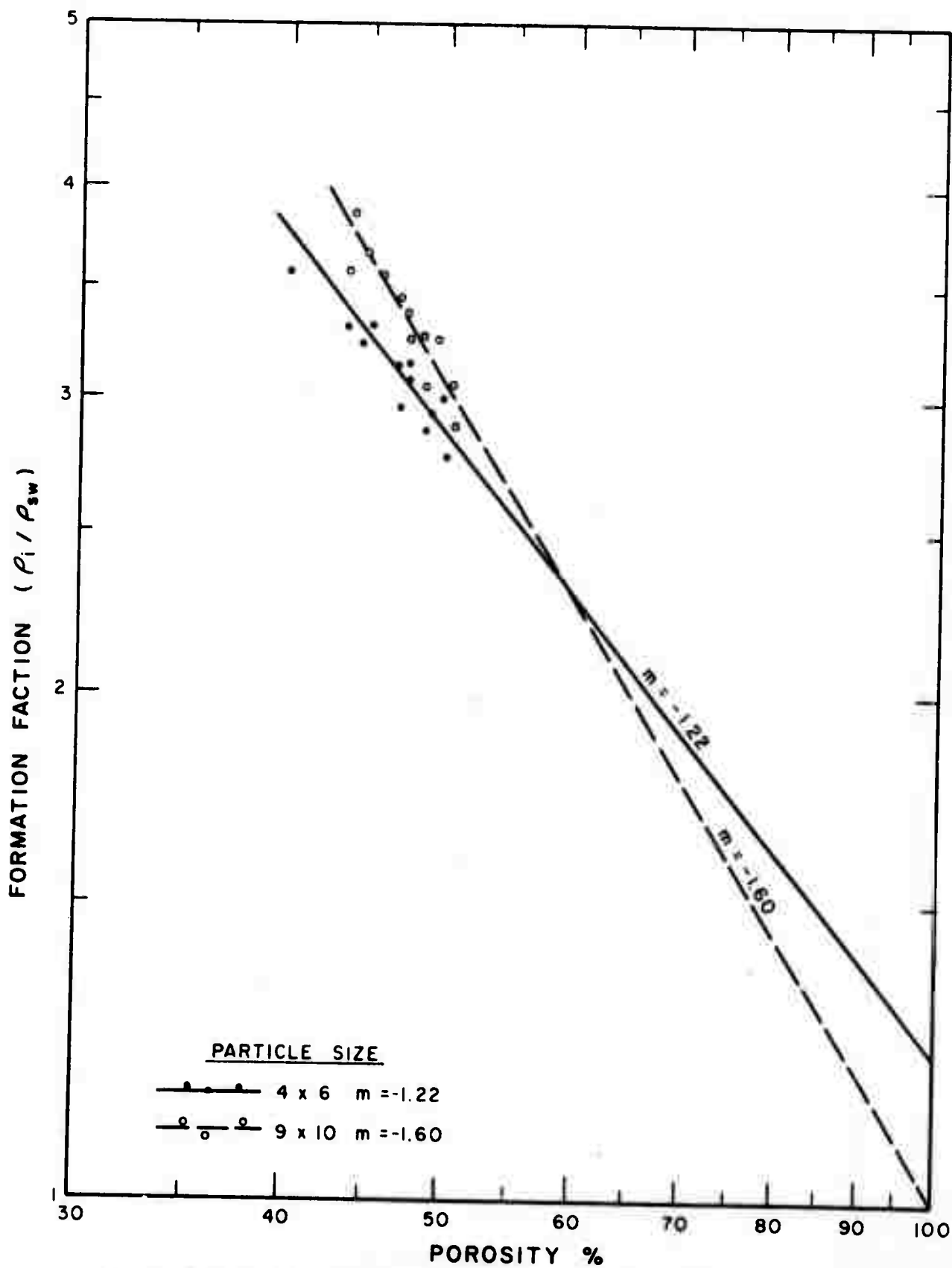


Figure 2-8a. Formation factor vs. porosity for Dolomite sand.

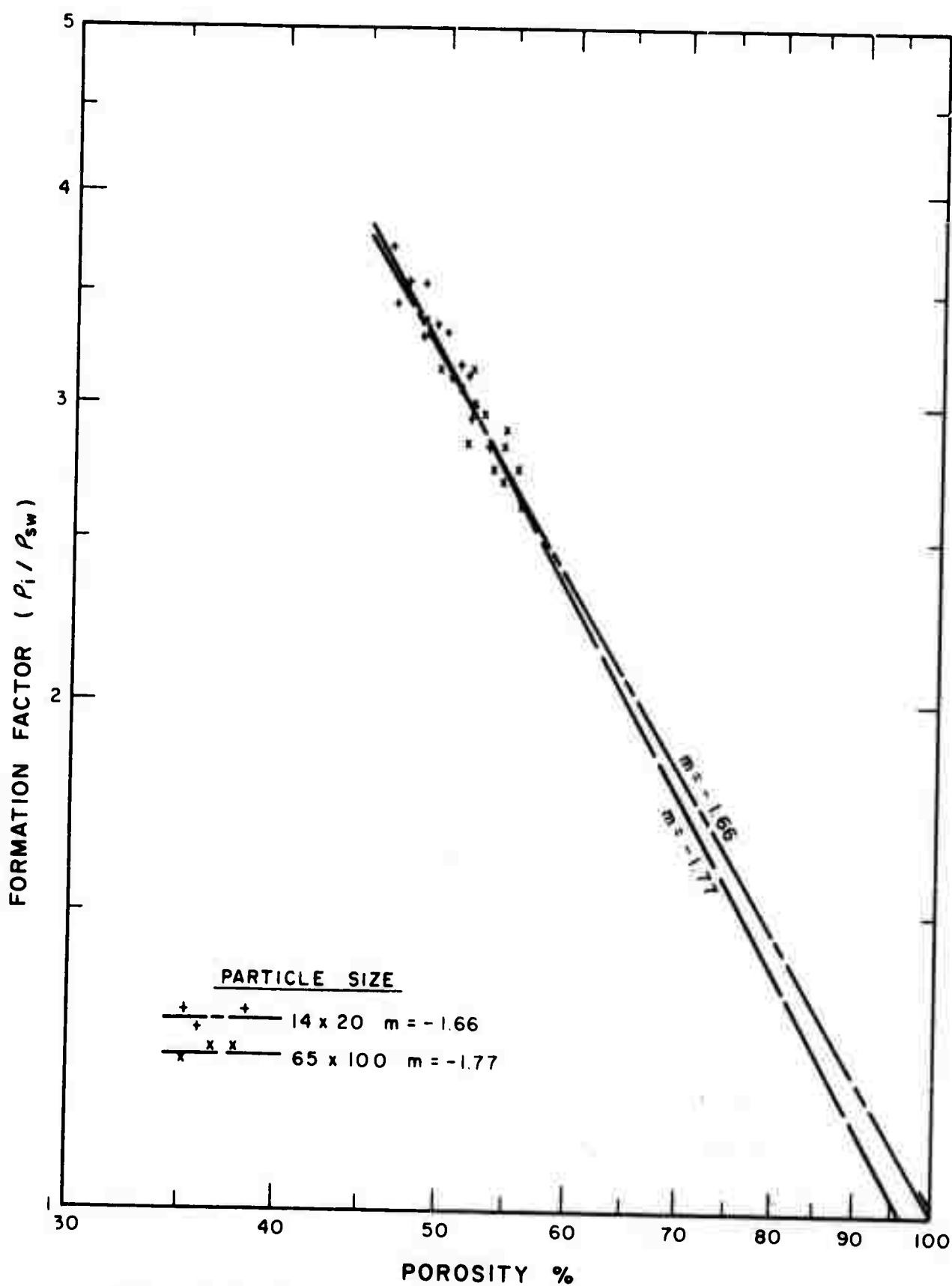


Figure 2-8b. Formation factor vs. porosity for Dolomite sand.

The formation factor versus porosity data points for dolomite are not, as a whole, tightly grouped except for particular particle sizes. As is shown in figures 2-8a and 2-8b, as the particle size decreases the values of m are about -1.2, -1.6, -1.7, -1.8 for the sizes tested. This is consistent with the evidence shown above that the smaller particles are more angular and will yield higher tortuosity values.

These tests of the resistivity instrument using sands were quite encouraging. The curves shown in figure 2-6 of sediment conductivity versus interstitial water conductivity are quite linear, as they should be. The average value of formation factor shown in this figure for 40 percent porosity Ottawa sand is 3.72. The value determined by Erchul and Nacci (1971) was 3.83.

The curves of formation factor versus porosity are quite satisfying given the additional knowledge of the shape of the dolomite grains as a function of size.

2.4 Initial Analysis of a Marine Electromagnetic Sounding System

Probes are presently in use (Kermabon, et al., 1969; Erchul and Nacci, 1971) which measure the resistivity of seafloor sediments. However, these probes disturb the sediment and sample only a small volume of the sediment through which they pass. One method of resistivity surveying which would allow the sampling of a large volume of undisturbed sediment would be electromagnetic sounding.

2.4.1 System Description

The electromagnetic exploration system envisaged employs as a source, a horizontal coil of wire (diameter about one-half meter) to which an alternating current is applied. At known horizontal distances in the plane of the source coil, pairs of small receiving coils are located which measure the horizontal and vertical components of the magnetic field strength. It is essential that the proper orientations of the receiving coils with respect to the transmitting coil be maintained. For this reason they must be secured to a rigid frame, which would limit the maximum coil separation to about 5 meters; a system even this large would be rather unwieldy to handle on shipboard and lower to the seafloor. The coil separation must be made as large as possible to maintain a useful depth of exploration, in this case the upper 1 to 2 meters of bottom material.

2.4.2 Analysis

In a homogeneous medium there would be no horizontal (radial) component of the magnetic field in the plane of the transmitting coil. However, if the coil is at the boundary of a more resistive half space, such as the seafloor, the field will be distorted, and the ratio of the horizontal to vertical components of the field will increase from zero with the resistivity ratio, or formation factor. Thus, the horizontal component of the field is sensitive to bottom resistivity.

The amplitude of the vertical component is, on the other hand, relatively insensitive because deviations due to the bottom material are only a small fraction of the observed vertical field. However, the out-of-phase component of the vertical field is, in the vicinity of the source, due to the damping effect of the conducting media, and is therefore relatively sensitive to bottom resistivity.

The signal seen at the receiving coils is highly dependent upon the frequency of the transmitted signal. At low frequencies there is very little induction (dB/dt) at the detectors, and at very high frequencies the field is severely attenuated as a result of the high conductivity of the sea water and saturated sediment. The amplitude of the field varies as

$$R^{-3} \exp \left(-R \sqrt{\frac{\omega \sigma \mu}{2}} \right)$$

where

R = distance from the source

ω = angular frequency

σ = conductivity = (resistivity) $^{-1}$

μ = permeability

Coggon and Morrison (1970) have calculated the fields due to a vertical dipole (horizontal loop) on a homogeneous sea floor; for a coil separation of 5 meters the frequency range which yields the strongest response is from 300 Hz to 300 kHz. At the upper end of this frequency range, however, it appears that it would be quite difficult to build a transmitting coil of suitable physical size.

With a receiver at a fixed distance from the transmitter parametric sounding can be accomplished to determine the response of the sediment as a function of frequency. A computer program written by J. H. Coggon ^{6/} has been used to calculate the horizontal magnetic field intensity of the sea floor; the curves and sea-floor models are shown in figure 2-9. It is apparent that one-layer and two-layer sea bottom models yield overlapping families of curves. For this reason, using only one detector it would be impossible to distinguish between a one-layer sea floor with, say, formation factor $F = 10$, and a two-layer case with $F = 5$ for the top 1 meter and $F = 100$ beneath that. Clearly, a particular curve represents no unique case.

To overcome this difficulty, it is necessary to conduct geometric sounding: changing the transmitter-receiver separation. This can be easily achieved in a marine electromagnetic system by locating several detectors at intervals along a frame extending from the transmitting coil. The detector nearest to the transmitter would have the shallowest depth of penetration and would yield a resistivity estimate of the uppermost portion of sediment. This information could be used to aid in interpreting the data from successively more distant detectors. Families of curves such as shown in figure 2-9 would have to be computed for interpreting the response. Alternatively, interpretation could be based upon the gradient of the field (actually, the difference of the field strengths seen at two detectors).

It can be noted from figure 2-9 that as the resistivity of the bottom increases, the horizontal magnetic field becomes less sensitive

^{6/} Dept. of Materials Science and Engineering, Univ. of Calif., Berkeley

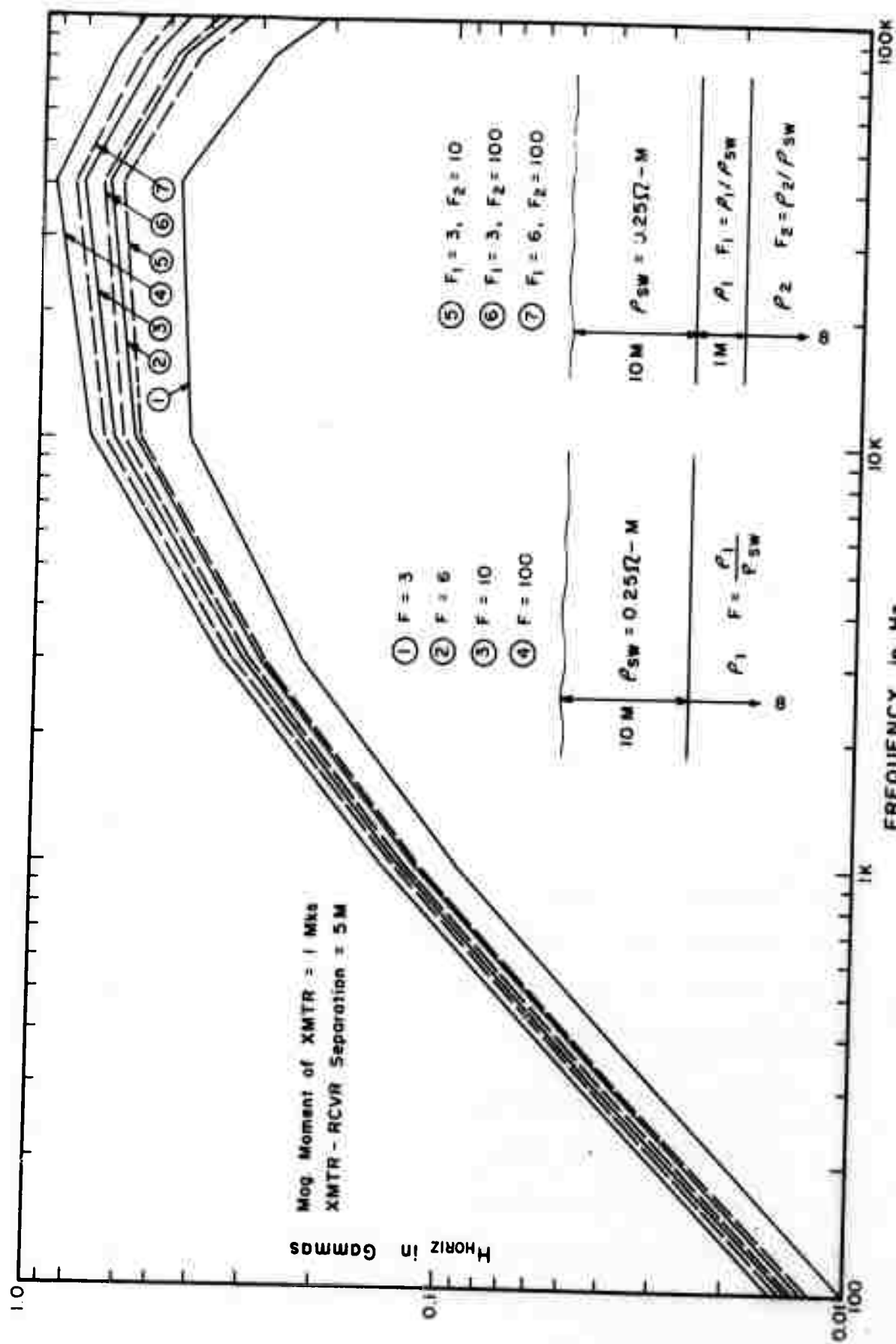


Figure 3-8. Horizontal magnetic field vs. frequency.

to bottom resistivity charges. For formation factors greater than 10 the sensitivity becomes very poor. A similar effect is noticed for the imaginary part of the vertical component of the field.

2.4.3 Conclusions

Further analysis of the marine electromagnetic system needs to be done to determine the utility of measuring gradients of the horizontal field, and to evaluate more fully if there is any advantage to be gained by measuring the imaginary part of the vertical component of the field.

Presently there appear to be two severe limitations on a marine electromagnetic sounding system: (1) depth of exploration greater than 1 to 2 meters would necessitate a frame whose size would be unmanageable, yet the importance of knowing coil separation and relative orientation would seem to require rigid connection; (2) the system would be rather insensitive to formation factors greater than 10.

An electromagnetic sounding system could not distinguish details of layering to the extent possible with a resistivity probe, but if bulk properties of the upper portion of sediment were desired, an electromagnetic system could prove quite useful. It would yield an average resistivity over a large volume of undisturbed sediment, and would reveal gross layering.

2.5 Resistivity Measurement by Direct Current Methods

The "direct current" (D.C.) resistivity methods have been used for many years to obtain information about the structure and porosity of subsurface formations on land. Adapted to marine use, they could provide a valuable geophysical tool for sea-floor investigations.

There are three principal methods of measuring subsurface resistivity:

1. Inductive electromagnetic techniques, in which high frequency alternating electric fields are used to induce currents and magnetic fields in the ground (an application of this is discussed in the previous section).

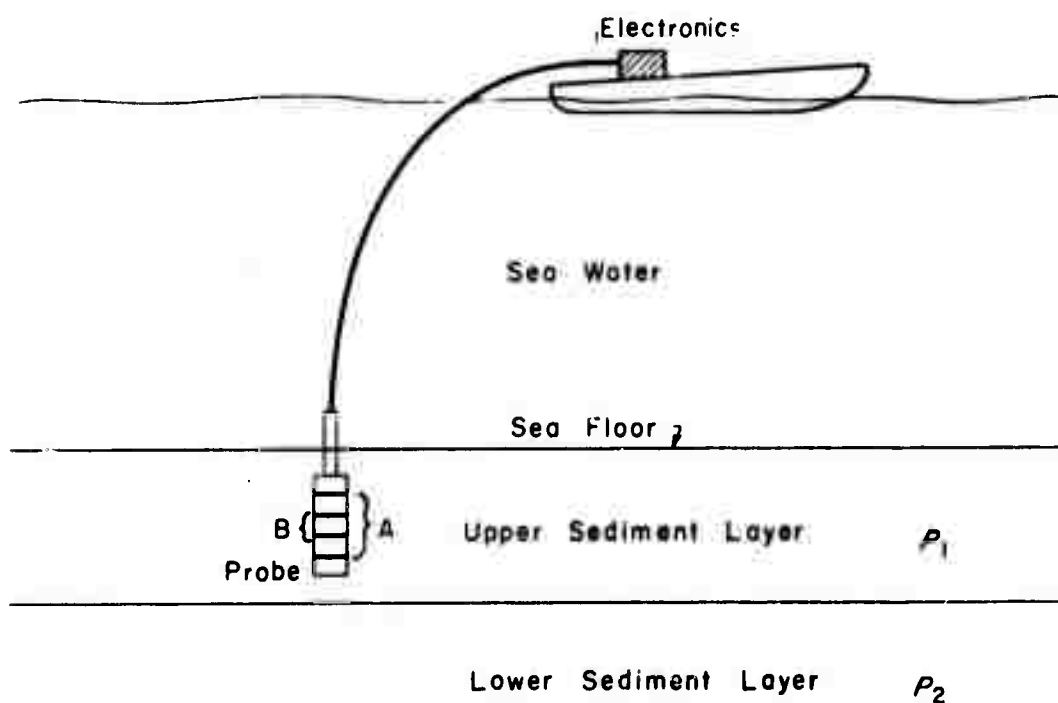
2. Well logging techniques, in which a small probe is lowered into a borehole or pushed into soft sediments.

3. "Direct current" methods, in which direct or low frequency alternating currents are introduced directly into the ground, and potentials are measured by electrodes inserted into the surface of the ground.

2.5.1 Well Logging Method

The well logging method, as described by Dakhnov (1959) and other authors, and shown schematically in figure 2-10, has been used for sea-floor resistivity measurements by Erchul and Nacci (1971), Kermabon, et al (1969), and Bouma, et al (1971). Their results indicate that the porosity and density of marine sediments may be obtained from the measured electrical resistivity. (The relation between electrical and other physical properties of sediments is discussed more fully in section 2.1).

The use of a logging probe gives a relatively precise determination of resistivity as a function of depth, but does offer some drawbacks. Measurements cannot be made while the ship is underway, and no measurement can be obtained if the probe is unable to penetrate the bottom. Also, the volume of bottom material sampled by the probe is small, which



A: Current Electrodes
B: Potential Electrodes

Current I is fed into the sediments through current electrodes A, and causes a voltage ΔV to appear between potential electrodes B. Sediment resistivity ρ is then determined from the formula

$$\rho = K \frac{\Delta V}{I}$$

where K is a factor depending on the geometry of the electrode arrangement.

Figure 2-10. Well logging probe used to measure resistivity of marine sediments.

may lead to interpretation errors if the sampled point is not representative of the surrounding area.

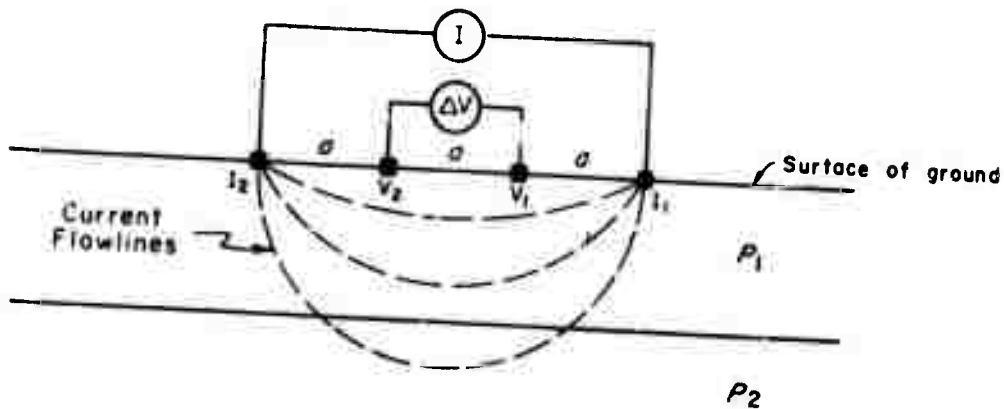
2.5.2 Horizontal Array Method

Description.

The use of a horizontal array of electrodes (figure 2-11) is another standard method of resistivity surveying on land. Mooney and Wetzel (1956), Van Nostrand and Cook (1966), Keller and Frischknecht (1966), Grant and West (1965), and Parasnis (1962), along with many other authors, cover this topic in detail.

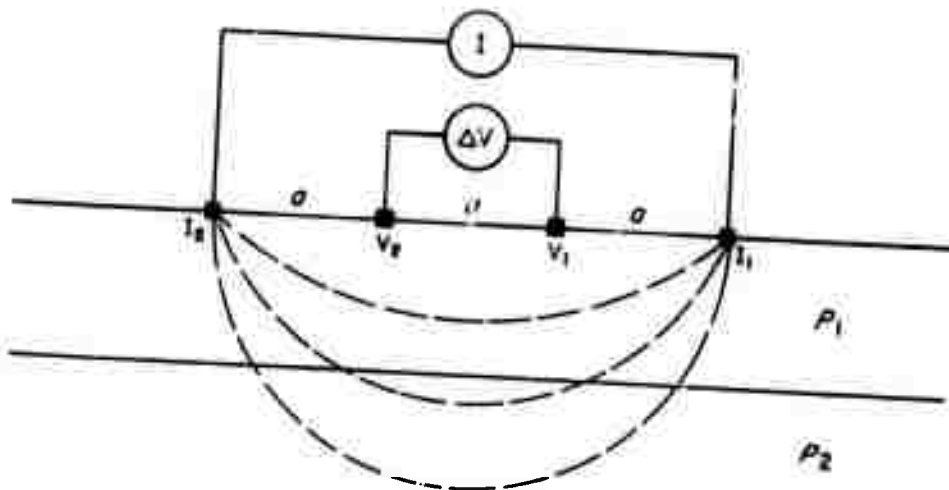
Briefly, a direct or low frequency alternating current I is introduced into the ground through two (or more) electrodes, usually in the form of copper or iron stakes. The potential difference on the surface of the ground is then measured between two (or more) electrodes inserted into the ground. These may be of the same type as the current electrodes or they may be of the "non-polarizing" variety. The voltage ΔV measured between the potential electrodes is a function of the current I and of the resistivity and structure of the ground below. By expanding the array, more current is forced to flow at greater depths, and information may be obtained on the change of resistivity with depth.

Many different array configurations are used for land surveys. The simplest is the Wenner array (figure 2-11), in which all the spacings a are equal. This the only configuration used in this study to date although others must be examined before the optimum array for marine use may be chosen.



A) Small Separation a .

V_1 and V_2 are potential electrodes
 I_1 and I_2 are current electrodes



B) Large Separation a .

Current I is fed into the ground through the current electrodes I_1 and I_2 , creating a potential field on the surface of the ground. The voltage difference, ΔV , between the potential electrodes V_1 and V_2 is a function of the resistivity of the ground below the electrodes. The apparent resistivity of the ground, ρ_o , is close to ρ_1 when the separation a is small, and approaches ρ_2 as a becomes very large.

Figure 2-11. Wenner resistivity array on land.

Interpretation of field data is done by use of a set of curves relating the ratio $\Delta V/I$ to the spacing a (figure 2-12). Usually, the ratio is converted to an "apparent resistivity", ρ_a , by use of the formula

$$\rho_a = 2\pi a \frac{\Delta V}{I}$$

The apparent resistivity would be equal to the actual resistivity if readings were made over an infinite, homogeneous half-space of resistivity ρ_a . As may be seen from figure 2-12, ρ_a changes with depth in a different manner for different layered situations. Use of the apparent resistivity concept gives a better qualitative feel for the resistivity-depth distribution, although the $\Delta V/I$ ratio would serve equally well for quantitative interpretation. In this study, the $\Delta V/I$ ratio is used as the ordinate for the interpretation curves, since the magnitude of the differences in this ratio will determine whether cases of geological interest may be distinguished.

Marine Application.

The use of an expanding horizontal array for sea-floor measurements (figure 2-13) has a number of advantages compared with the use of a probe. The "depth of penetration" is limited only by the size of the array and the amount of current available, so information may be obtained at considerable depths below the seafloor. Also, measurements may be made with the ship underway, at a considerable savings in time and expense. Even an array on the bottom may, in many cases, be dragged continuously across the sea floor as done by Marke (1965). On the other hand, a probe gives a more precise determination of resistivity with depth, and interpretation is simpler because there is no need to refer

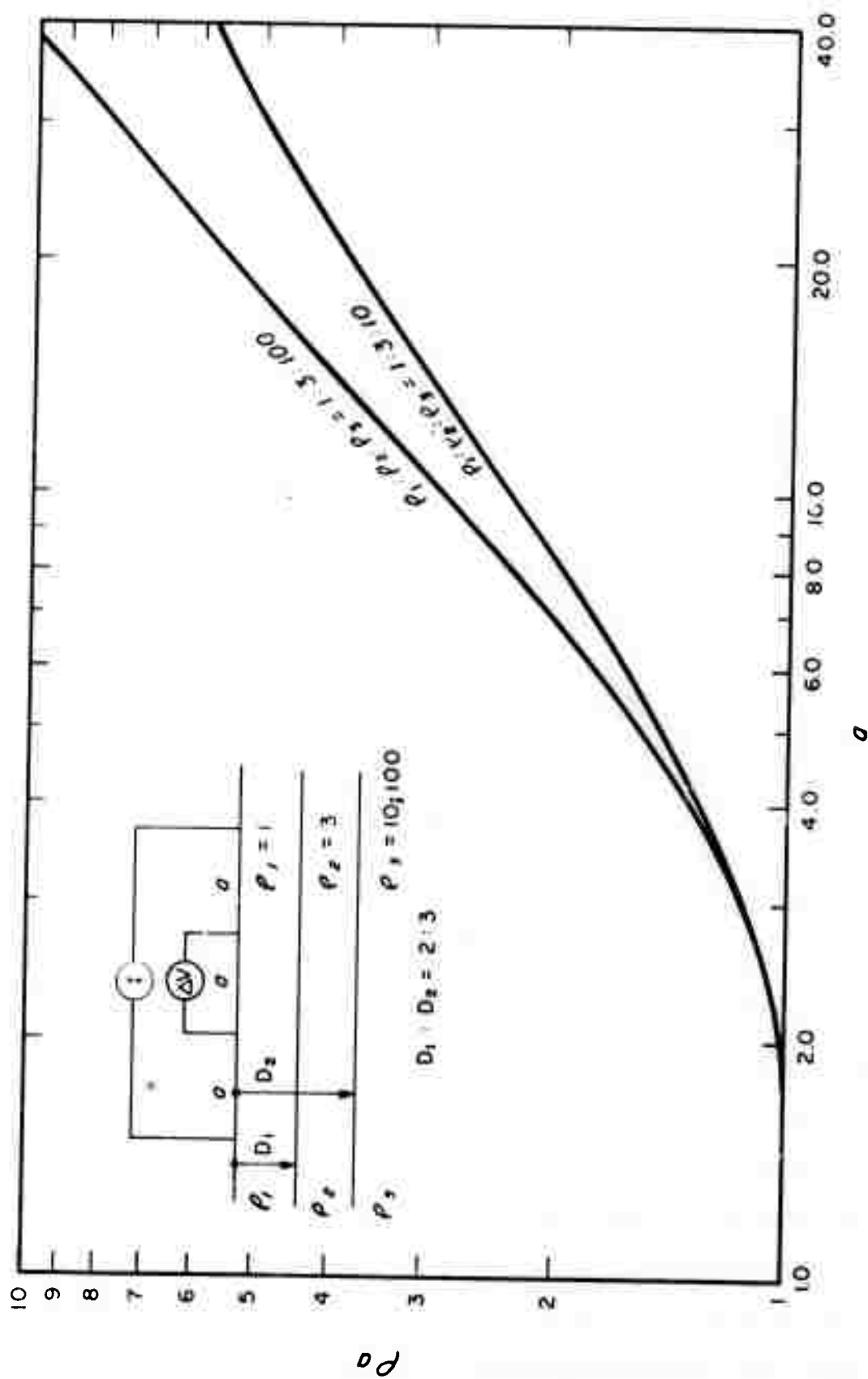
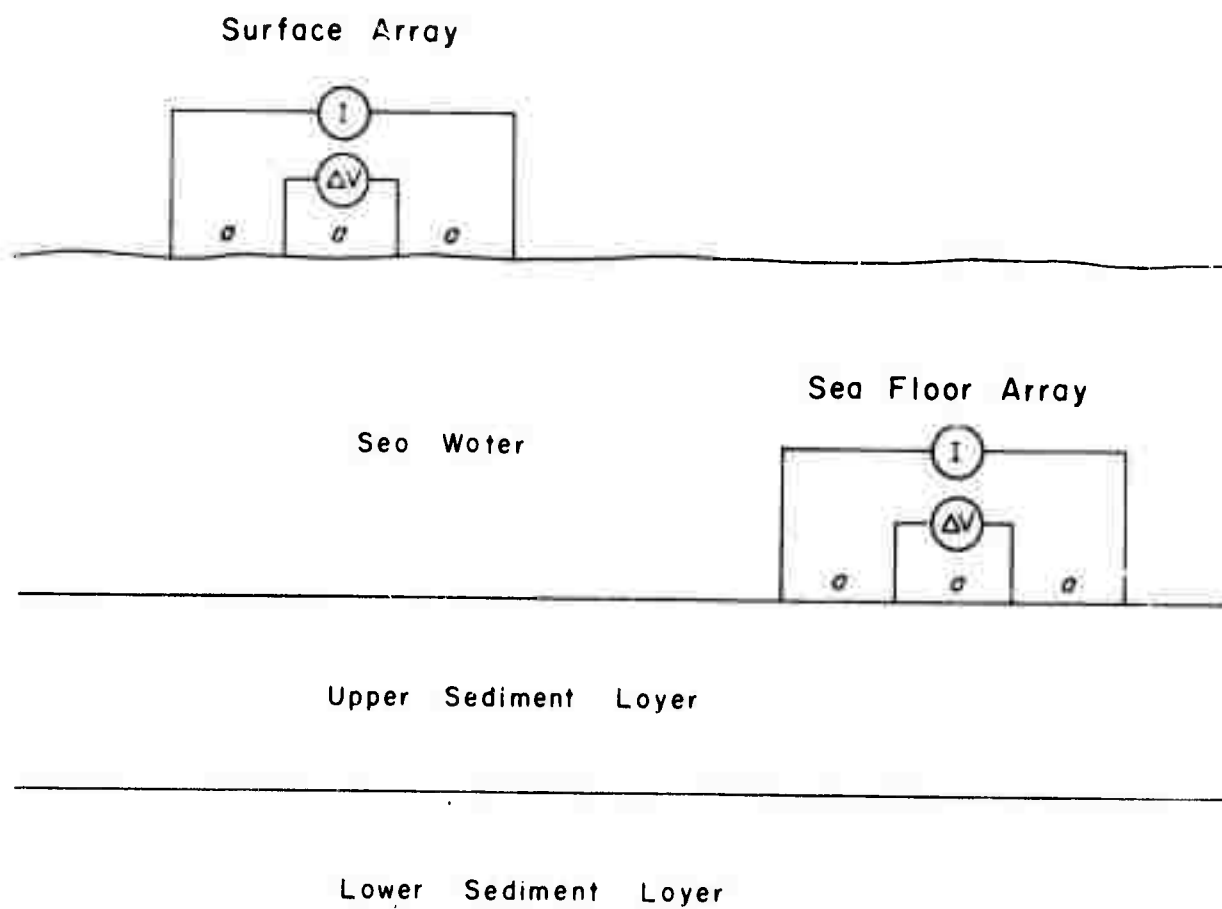


Figure 2-12. Wenner resistivity curves for a 3-layer model. (After Mooney and Wetzel (1956)).



The surface array is easier to tow, but the sea floor array is closer to the bottom, so it can "see" bottom resistivities of smaller values of the separation a .

Figure 2-13. Surface and sea-floor Wenner arrays.

to a set of curves to obtain the resistivity--depth relationship from the observed data. Also, the curves in some cases contain ambiguities which make interpretation more difficult.

The probe and horizontal array methods, then, are complimentary. Since considerable work has been done on the probe method by the authors cited above, it was decided for this project to investigate the horizontal array techniques for their applicability to sea-floor resistivity measurements.

Some previous work has been done in this area. Marke (1965) has studied the single layer case in detail, and has dragged a fixed array over the bottom off the coast of Cornwall, England. Volker and Dijkstra (1955) have measured the chloride content of deep ground waters under submarine sediments in the Netherlands using a marine Wenner array. Terekhin (1962) and Van'yan (1956) have examined the theory of the multilayered submarine case with current and measuring electrodes placed on the sea floor. Other Russian workers have apparently published curves for sea-floor resistivity arrays, and have carried out resistivity measurements at sea, but we have not yet been able to obtain copies of their work.

In order to determine the utility of the horizontal array for the measurement of sea-floor resistivity, sets of curves similar to those shown in figure 2-12 must be developed for arrays deployed over a layered bottom, both at the sea surface and on the sea floor. A comparison of these curves would show whether the surface array, which must "see" through a highly conductive layer of sea water before it can sense the bottom conductivity, would be useable for practical surveying

(it is obviously much easier to tow an array on the surface than to drag it over the bottom). The work of Marke (1965) indicates that an array on the surface is much less efficient than one on the bottom, but a more detailed study, especially for layered bottoms, must be made.

Next, it must be determined whether it will be possible to select or design instrumentation capable of measuring the desired quantities with the accuracy needed for practical application. Finally, the instrumentation must be selected (or designed and built) and tested in the marine environment, and the test results compared with the parameters measured on the samples taken from the MMTC test range (section 3.2.8).
Development and Interpretation of Curves.

For an array deployed on the sea surface, published sets of curves such as those by Mooney and Wetzel (1956) for the Wenner array, or Rijkswaterstaat (1969) for the Schlumberger arrangement are available. For an array on the sea floor, however, no general sets of curves are available. Terekhin (1962) has developed the mathematics needed to solve the most general case, that of a point source of current on the sea floor over an N - layered bottom, but the form of his solution is not ideal for computer calculation of actual values over a bottom with one or two layers.

Since three layers are usually the most that can be resolved in practice on land, two layers will probably prove to be the upper limit of resolution for marine studies. Therefore, the mathematics and computer programs to calculate the potential distribution over a two-layered bottom, due to a point source of current on the sea floor,

were developed. The mathematical analysis and the computer program are presented in section 4.2.

The program calculates V_r/I , the voltage on the sea floor at a distance r from the source, divided by the input current. The value of $\Delta V/I$ for the Wenner array may then be easily found by use of the formula

$$\frac{\Delta V}{I} = 2 \left(\frac{V_r}{I} - \frac{V_{2r}}{I} \right)$$

where V_{2r} is the voltage at a distance $2r$ from the source. Finally, the quantity $\Delta V/I$ is plotted against a , giving curves such as those shown in figures 2-14 and 2-15.

In order to be of use in the interpretation of sediment layering, the curves for various cases of geologic interest as obtained from field data must be distinguishable. As discussed below, it appears that differences on the order of 1 millivolt may be resolved by the field equipment which has been constructed. It is apparent that resolution is increased by increasing the input current I , as this increases the signal to noise ratio. As the current is increased, more subtle geologic cases may be distinguished from each other. Since the system discussed below will provide 10 amps of current, differences in the value of $\Delta V/I$ of about 0.1 millivolts/amp should be distinguishable from the field data. This value will be used as a preliminary criterion as to whether two readings obtained in the field may be resolved: if the difference in the value of $\Delta V/I$ for two geologic cases, at the same separation a , is greater than 0.1 millivolts/amp, the curves of $\Delta V/I$ vs a for the two cases may be distinguished at that point.

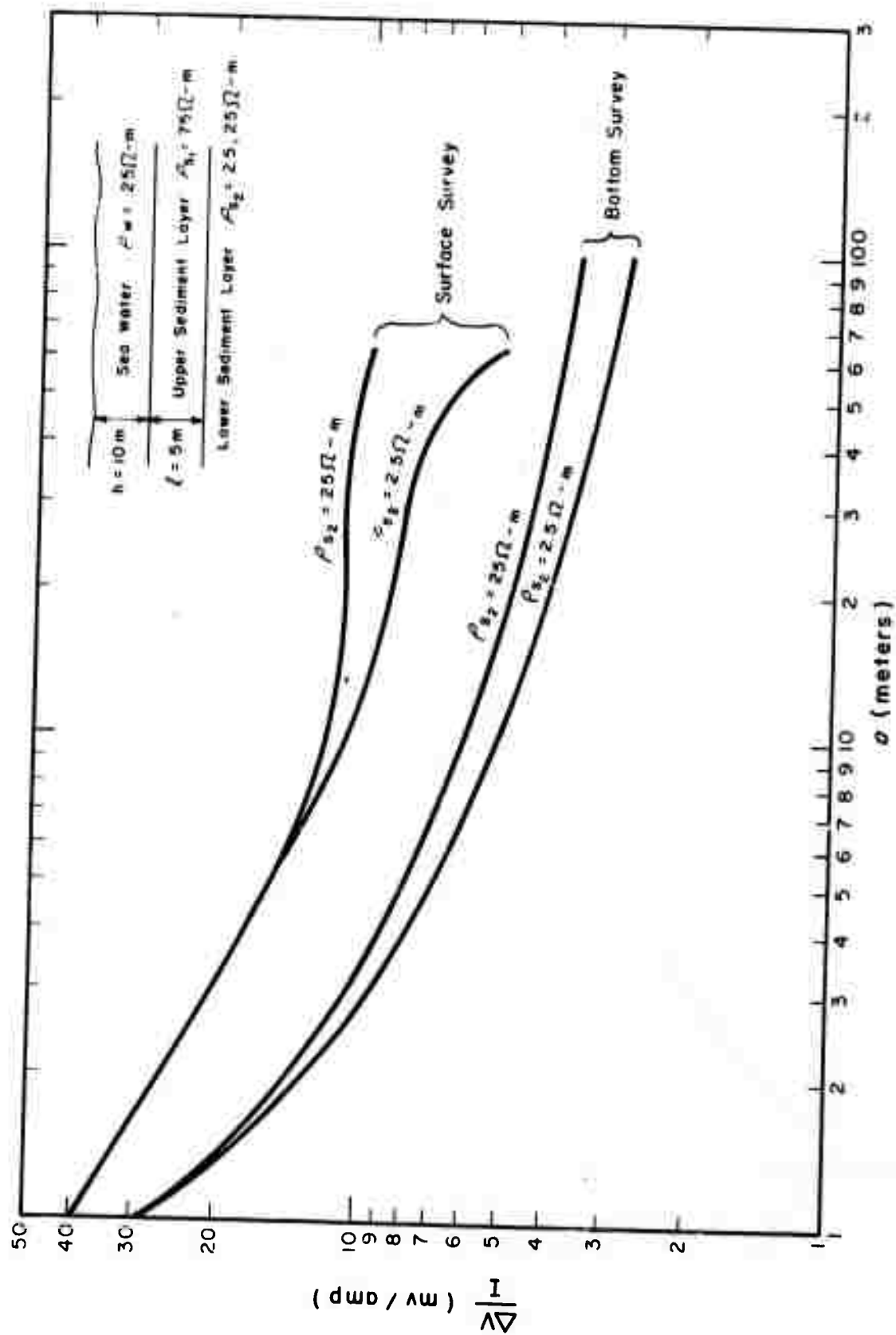


Figure 2-14. $\Delta V/I$ vs. ρ for a surface and a bottom Wenner array.

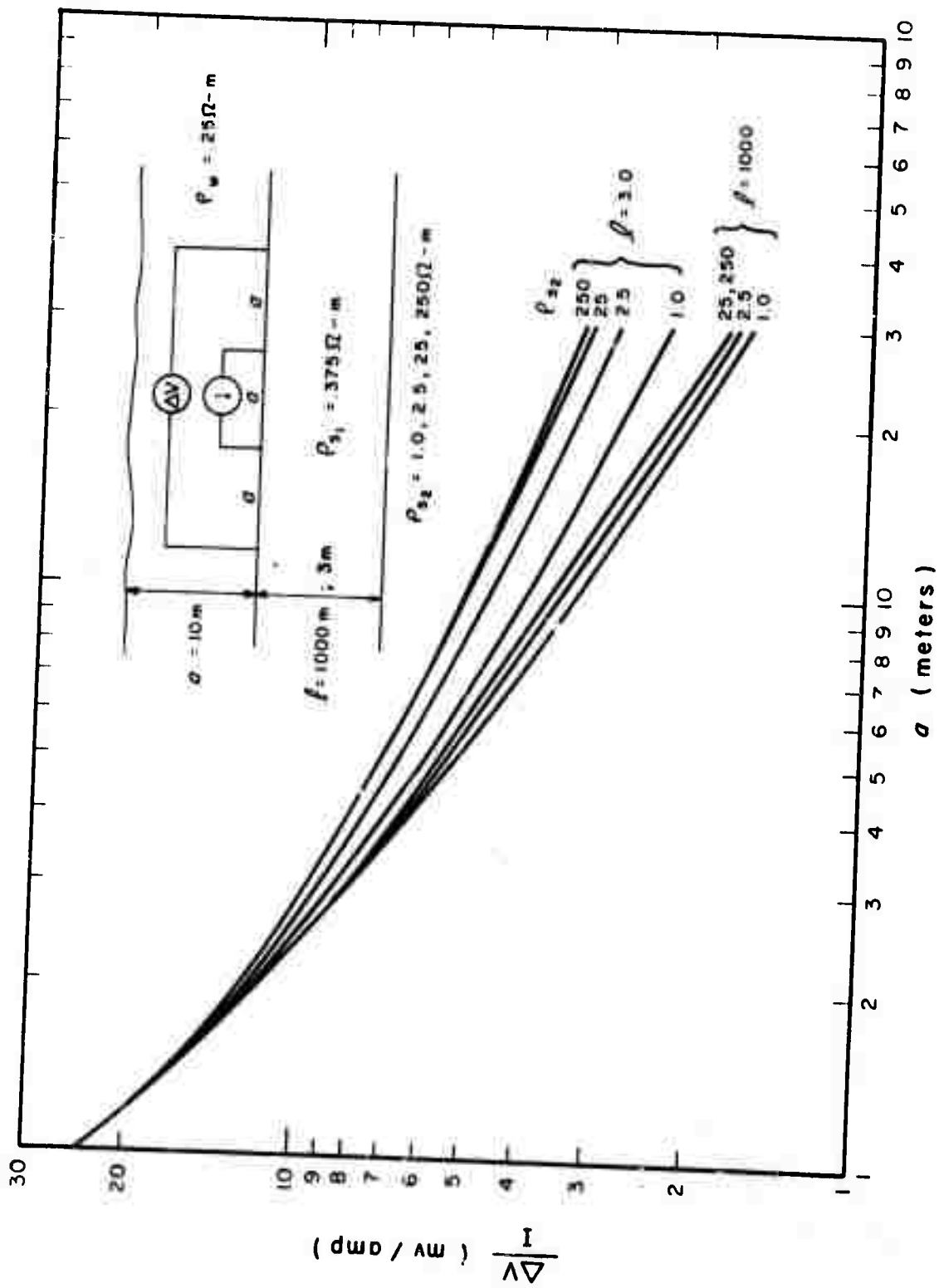


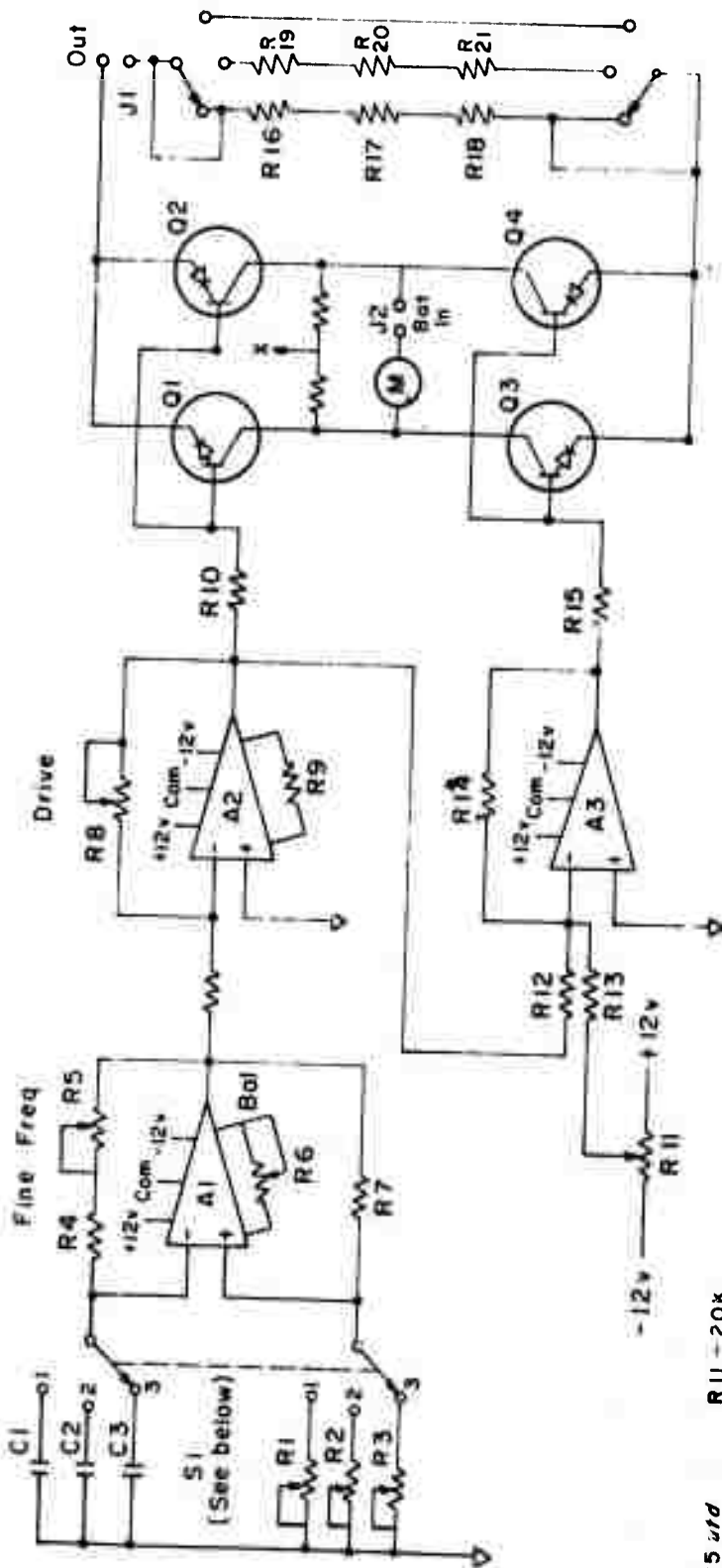
Figure 2-15. $\Delta V/I$ vs. a for a bottom Wenner array, with varying basement depth and resistivity.

Figures 2-14 and 2-15 are examples of the types of curves to be evaluated. Figure 2-14 shows the effect of varying the basement layer resistivity while holding the geometry constant for a hypothetical submarine situation. It may be seen that the difference in the resistivity of the bottom layer may be distinguished for values of a greater than 1 meter for an array on the bottom and for values of a greater than about 6 meters for an array towed on the surface. Figure 2-15 shows the effect, for a different layered case, of varying the depth to the lowest layer and the basement resistivity. The higher basement resistivities, 25 and 250 ohm-meters ($\Omega \cdot m$) are difficult or impossible to distinguish at any but very large values of a , while the lower resistivity cases are distinguishable for values of a ranging from 2 to 4 meters.

Equipment.

Because commercially available resistivity units are designed to be used in materials of high resistivity, they operate at high voltages and low currents. A unit to be used in the low resistivity marine environment, however, must operate at high currents in order to give useful values of the $\Delta V/I$ ratio, while the low contact resistances involved reduce the need for high voltage. Accordingly, a unit which uses an automotive or similar storage battery as a current source, and provides square wave output at currents up to 10 amps and at frequencies ranging from 0.2 to 20 cps. was designed and built at MMTC. The wiring diagram for this unit is shown in figure 2-16. A high impedance rectifying voltmeter for reading ΔV was also designed and constructed (figure 2-17).

Coarse Freq



C1 - 25 μ f

C2 - 50 μ f

C3 - 100 μ f

R1 - 20K

R2 - 150K

R3 - 25K

R4 - 100K

R5 - 1 meg

R6 - 260 Ω

R7 - 1 meg

R8 - 10K

R9 -

R10 - 2K

R11 - 20K

R12 - 10K

R13 - 100K

R14 - 10K

R15 - 2K

R16 - 1/2 Ω

R17 - 1/2 Ω

R18 - 1/2 Ω

R19 - 1/2 Ω

R20 - 1/2 Ω

R21 - 1/2 Ω

R22 - 100 Ω

R23 - 100 Ω

Q1 - MJ4033

Q2 - MJ4030

Q3 - MJ4033

Q4 - MJ4030

SI Pos

1 - 2.0-20.0 cps

2 - 0.2-2.0 cps

3 - 0.02-0.2 cps

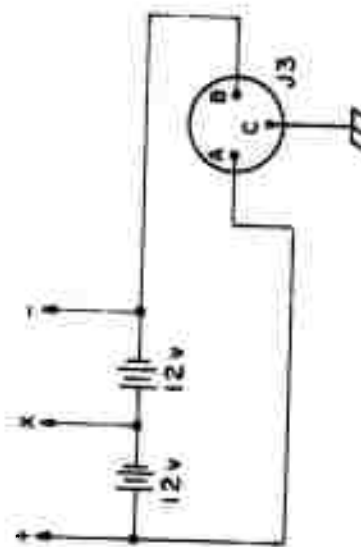


Figure 2-16. Square wave current source.

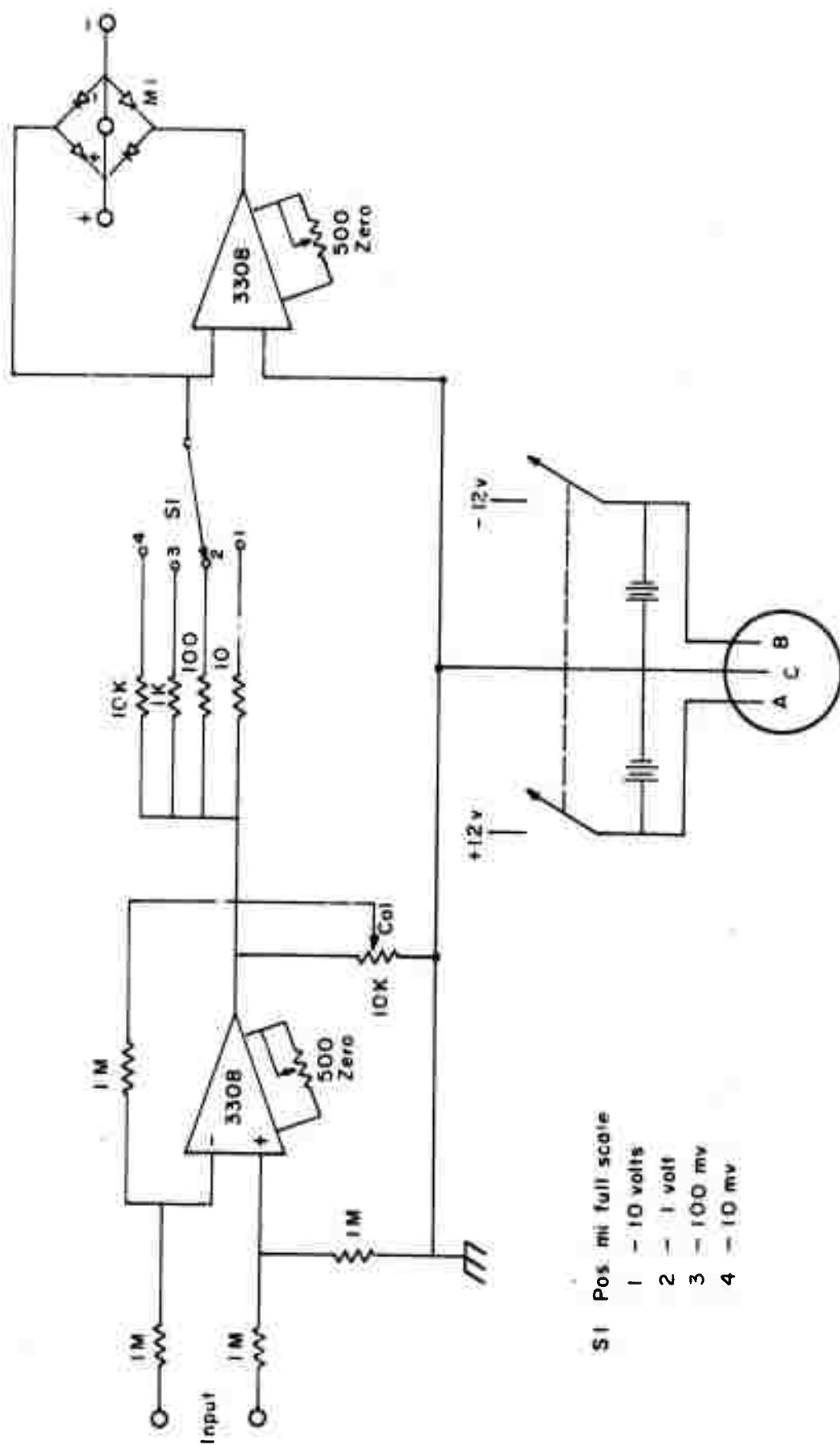


Figure 2-17. High impedance rectifying voltmeter.

Field Tests.

Three preliminary field tests have been run. For the first test a small array with a fixed spacing a of 20 cm. was lowered to the bottom off the wharf at MMTC (figures 2-18 and 2-19). For such a small electrode spacing, the bottom may be considered to consist of only a single layer of resistivity ρ_s and the water layer may be considered to be infinitely deep. In this case,

$$\frac{\rho_s}{\rho_w} = \frac{1}{\frac{\rho_w}{2\pi a \frac{\Delta V}{I}} - 1}$$

where

ρ_s is the resistivity of the (single) sediment layer.

ρ_w is the resistivity of the water.

A detailed derivation of the equation is given in the Appendix (Sec. 4.2.4). This formula may then be used to obtain sets of curves such as that shown in figure 2-20, for $a = 20$ cm. In this case, the measured value of $\Delta V/I$ was 140 millivolts/amp, which gives a value of ρ_s/ρ_w of 1.3 for the measured value of $\rho_w = 0.308 \Omega - m$. The value of $\Delta V/I$ appeared to be independent of the frequency or current used. The chart recorder was used to monitor the form of the potential signal. It was noted that the readings were subject to D.C. drift, although the peak-to-peak values of the signal were reasonably stable. The drift was probably due to corrosion of the copper potential electrodes, indicating that nonpolarizing potential electrodes are a better choice in the corrosive marine environment.

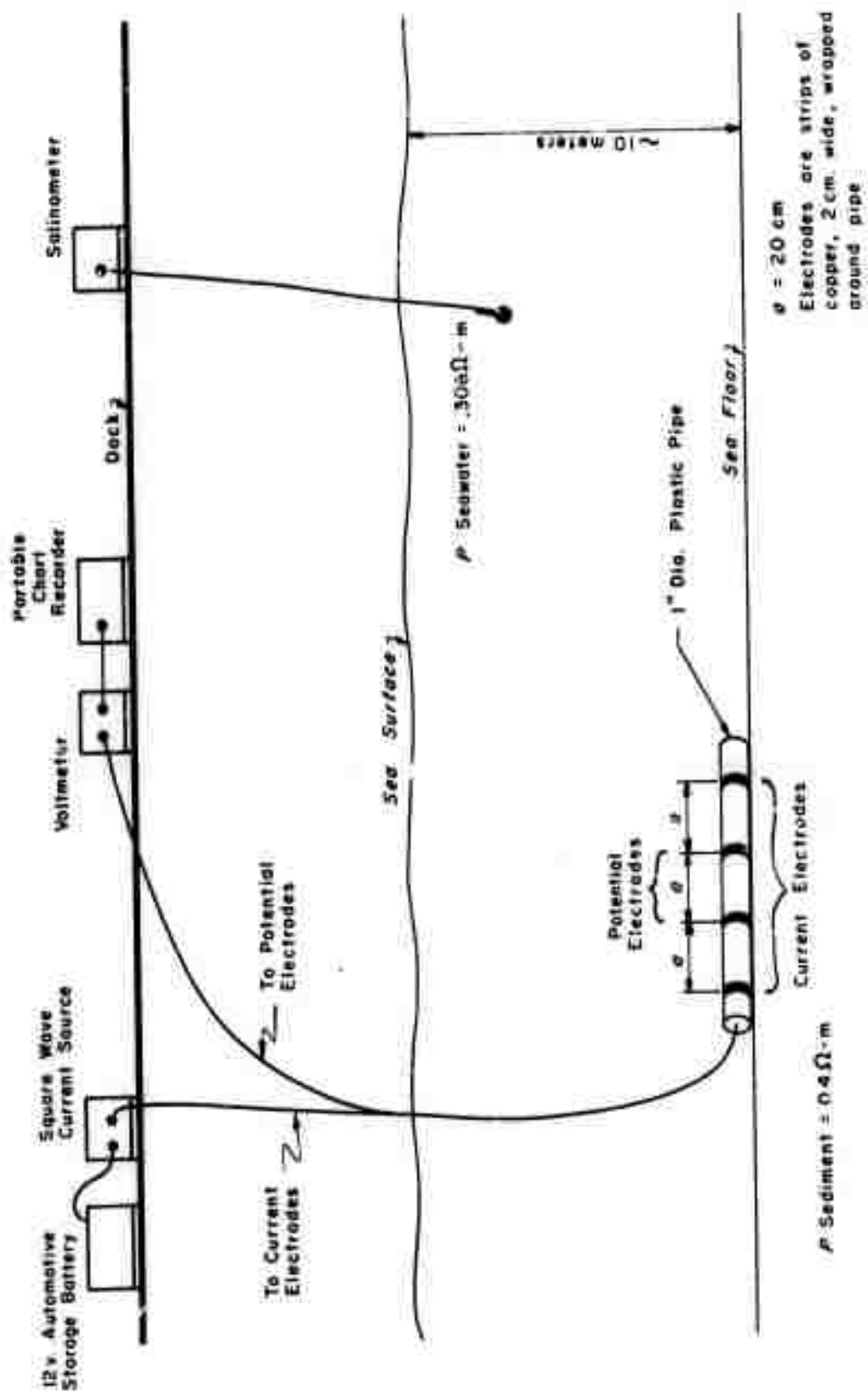


Figure 2-18. Field test arrangement for 20-centimeter Wenner array.

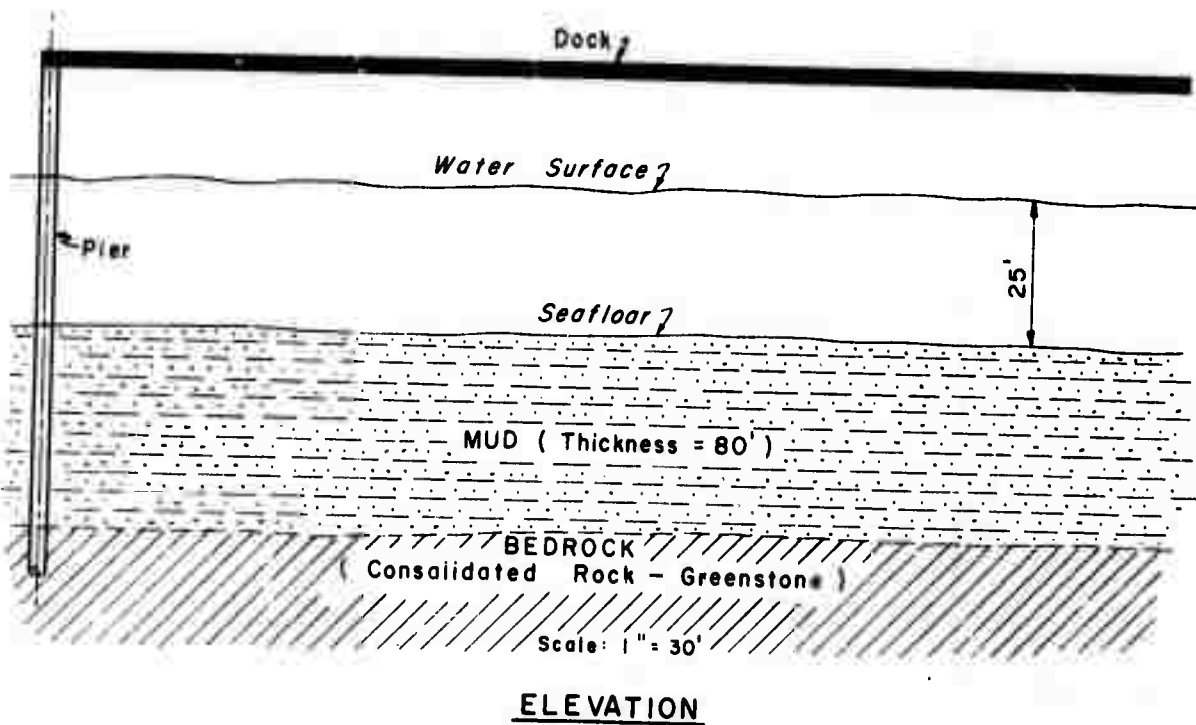
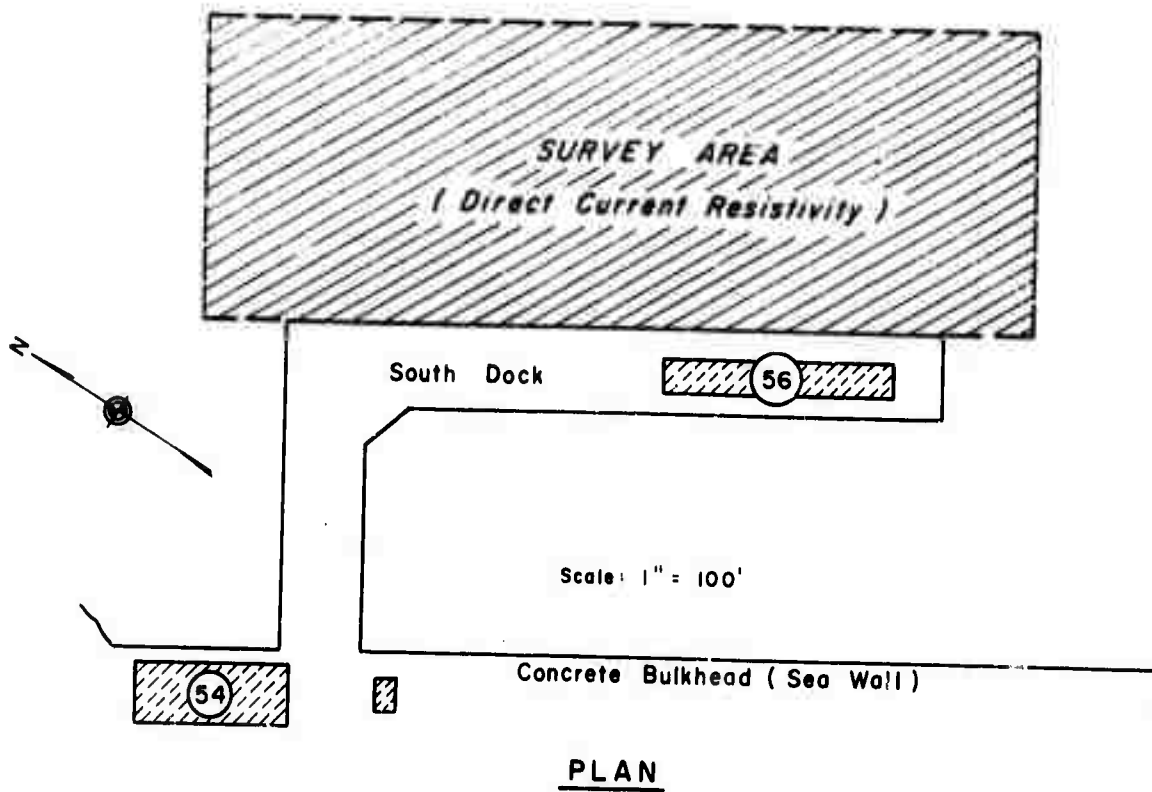


Figure 2-19. Test site - resistivity experiment.

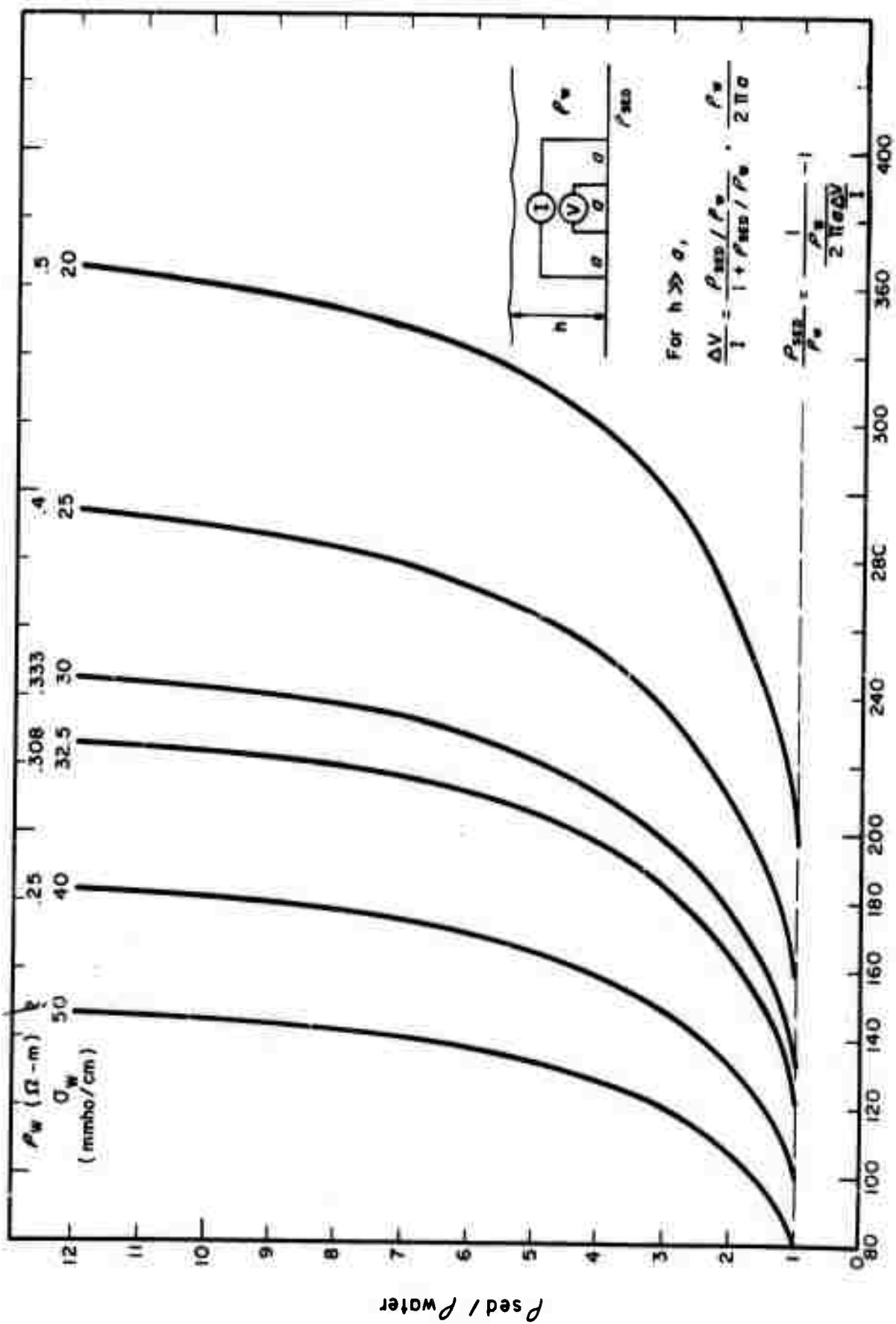
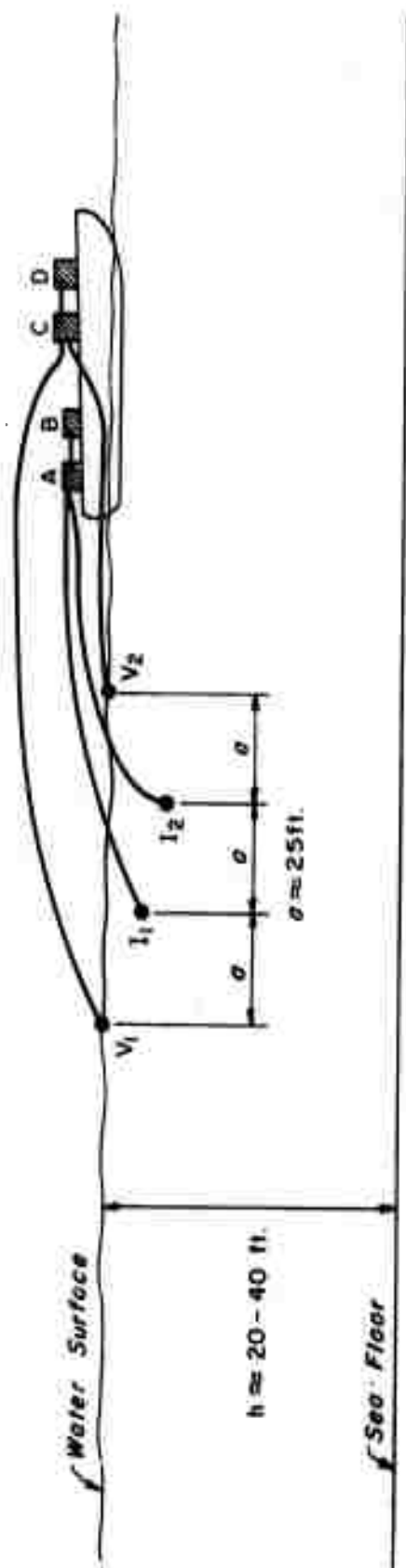


Figure 8-30. $\rho_{sed} / \rho_{water}$ vs. $\Delta V / I$ for $h \gg a$ and $a = 20$ cm.

For the second test, an attempt was made to use an expanding Wenner array off the same dock, deployed first on the surface and then on the bottom for each spacing a . Nonpolarizing silver-silver chloride potential electrodes as described by Von Arx (1962) were used, and drift was considerably reduced. Unfortunately, two factors caused the readings obtained to be extremely erratic. First, the large pilings and considerable amount of metal attached to the pilings undoubtedly distorted the potential fields severely. Second, a very strong tidal current made it impossible to position the electrodes accurately. For these reasons, no quantitative interpretation was made of the test results.

The performance of a towed array was observed for the third field test. The array was in the form of a very rough Wenner configuration with $a \approx 25$ feet (figure 2-21). The current electrodes were copper rods about 1 inch in diameter by about 6 inches in length, while the potential electrodes were of an improved silver-silver chloride nonpolarizing type (figure 2-22). No attempt was made to obtain quantitative readings of bottom resistivity since the configuration was not known with sufficient accuracy.

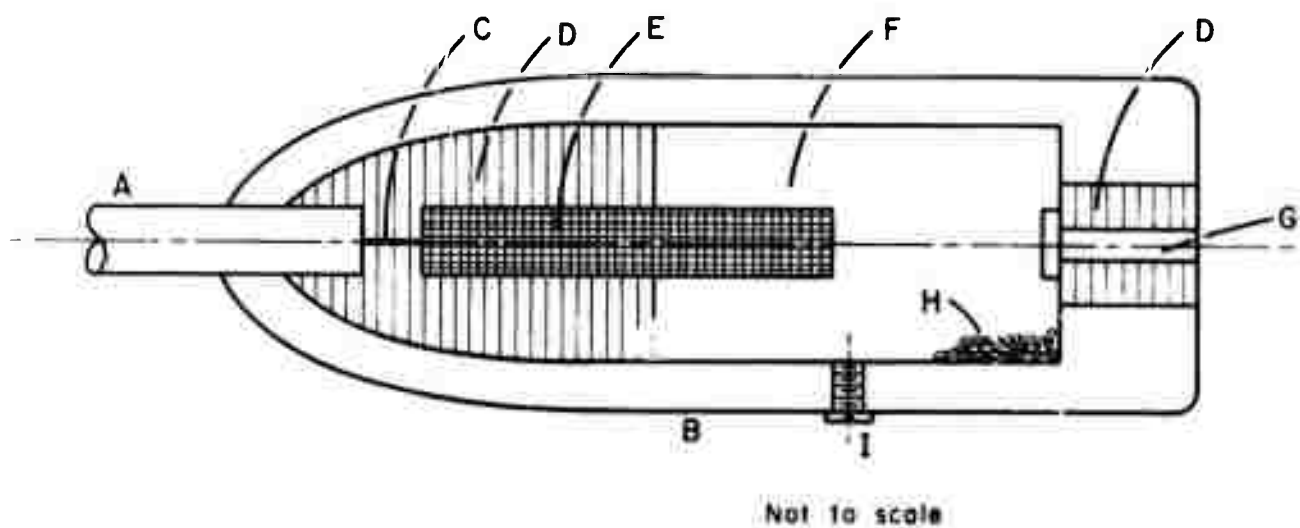
An important result, however, was apparent from the test: the reading of ΔV between the potential electrodes, with no power applied to the current electrodes, showed negligible drift and noise levels, well under 1 millivolt (figure 2-23). When power was applied to the current electrodes, a typical signal looked like figure 2-24. The noise seen on the signal was due to problems in the current source, which are being corrected, and random motion of the electrodes, which



V_1, V_2 : Potential Electrodes
 I_1, I_2 : Current Electrodes

A : Current Source
 B : Storage Battery
 C : High Impedance Voltmeter
 D : Chart Recorder

Figure 2-21. Towed array field test.



- A - Cable Insulation
- B - Plexiglas Housing
- C - Conductor
- D - Epoxy Resin Potting
- E - Silver-Silver Chloride Element
- F - Filling Solution: Saturated AgCl and KCl
- G - Porous Ceramic Rod
- H - KCl Crystals
- I - Filling Screw

Figure 2-22. Non-polarizing silver-silver chloride electrode.

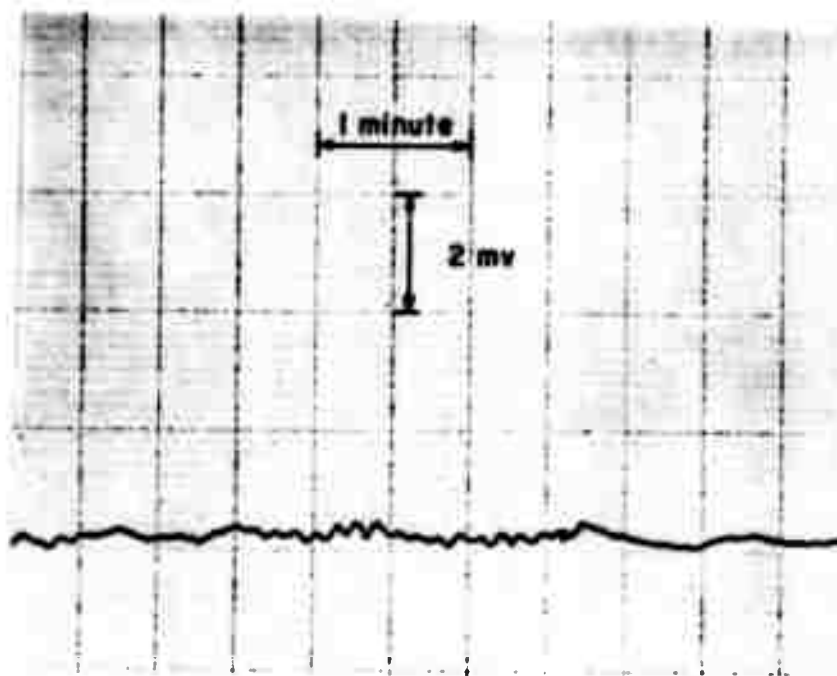


Figure 2-23. ΔV between potential electrodes, $I=0$.

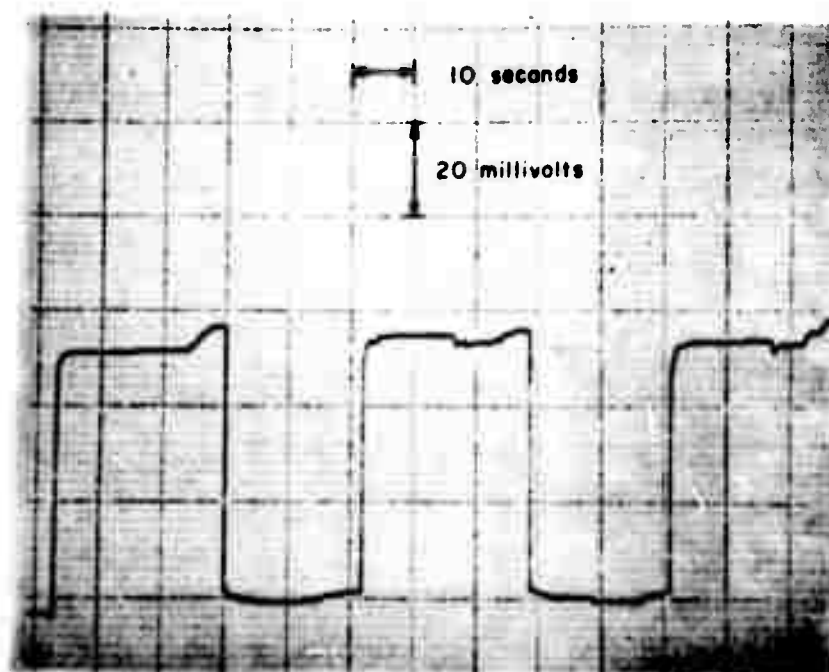


Figure 2-24. ΔV between potential electrodes, $I=5.4$ amps.

could be stopped by taping the four lines together. Once these problems are corrected, the signal should be easily readable to less than 1 millivolt.

2.5.3 Conclusions and Recommendations

It appears that the direct current resistivity method is applicable to the study of sea-floor properties. Preliminary field test results indicate that differences in the value of ΔV of 1 millivolt may be resolved and examination of curves such as figures 2-14 and 2-15 shows that with currents up to 10 amps, differences of a millivolt or more appear between the curves $\Delta V/I$ vs. a for at least some of the geologic cases studied.

Recommended future work includes:

1. A study of the different array configurations to determine which is the most useful in the marine environment.
2. A thorough theoretical comparison between surface- and bottom-towed arrays.
3. Compilation of a large number of interpretation curves for cases of geologic interest.
4. Fabrication of a multiple electrode expanding array which may be streamed at the surface, towed over the bottom, or deployed stationary on the bottom.
5. Field tests over the MMTC test ranges in San Francisco Bay (section 3.2.8.1) and Monterey Bay, and comparison of results with those obtained by coring, drilling, and the other geophysical methods described in this report.

3. DETERMINATION OF SEDIMENT PROPERTIES BY ACOUSTIC METHODS

3.1 Refraction Methods

3.1.1 Relationship Between Seismic Parameters and Other Soil Properties

Measured values of compressional-wave velocity, shear-wave velocity, attenuation coefficients of these two waves, and bulk density can be used to determine several properties of sediments. Rigidity, bulk modulus, Lamé's constant, Poisson's ratio and Young's modulus can be calculated directly while porosity, mean grain size, and shear strength possibly can be found through empirical relationships with the measured physical properties. Some previous work along these lines has been conducted by Hamilton et al (1970), Hamilton (1970b, 1971), Horn et al (1968), Schreiber (1968), Shumway (1960), and Sutton et al (1957).

3.1.2 Experimental Methods

The determination of the shear-wave velocity in the upper layers of marine sediments is difficult because shear waves will not propagate in water and consequently are transmitted poorly in a saturated, porous medium. On the other hand, the compressional wave is transmitted readily in water and in saturated sediments.

To date, no in situ seismic method has been found that will directly give the shear-wave velocity in saturated marine sediments. In fact, in earlier studies by Wood (1941), it was assumed there was no transmission of a shear wave in marine sediments. It was later found by Nafe and Drake (1963) and Hamilton, et al (1971) that almost all marine sediments have measurable rigidities and transmit shear waves.

Viscoelastometers have been demonstrated to be a means of obtaining the shear-wave velocity. The method involves measuring the real and imaginary parts of the rigidity from torsional waves propagating along the length of a round rod. However, the method is very dependent on the temperature properties of the rod, and furthermore, an in situ viscoelastometer has not yet been developed.

Another method used to determine the shear-wave velocity is the use of Stoneley waves (Davies, 1965, Hamilton, 1970, et al). Stoneley waves are generalized Rayleigh waves that propagate along the interface between two media such as a water-sediment interface. After obtaining the Stoneley-wave velocity from a seismogram, the shear-wave velocity is found from equations relating the shear-wave velocity to the Stoneley-wave velocity (Strick and Ginzberg, 1956). The disadvantage of this method is that it is difficult to tell when a Stoneley-wave begins on a seismogram. Furthermore, the equations relating the Stoneley wave velocity to the shear-wave velocity assume a liquid layer over a homogeneous, isotropic solid medium which extends to an indefinitely great distance. These conditions for the solid medium prove to be an ideal case that is not seen in earth sediments.

It appears that one does not have to resort to determining the shear-wave velocity indirectly using Stoneley waves or a viscoelastometer. By using a specially designed S_H source with a correctly oriented horizontal geophone and a vertical geophone, both the shear-wave velocity and compressional-wave velocity may be obtained from their respective direct waves. (The horizontal geophone is oriented to produce a large response to the direct S_H wave and the vertical geophone

records the particle motion of the direct P wave). This is the method investigated in this study.

The attenuation of the shear wave and the compressional wave may be determined using the technique of Fast Fourier Transforming, based on a Cooley-Tukey algorithm (Cooley, 1967). In this technique, one obtains the amplitude spectral density from the analog voltage and then squares this value. After converting the resulting energy to decibels, energy versus frequency is plotted, and spectra at different geophones are compared. For a certain frequency, the energy level difference divided by the geophone separation is the attenuation in decibels per length unit.

Density values from laboratory measurements on core samples have been obtained at the test facility in San Francisco Bay (section 3.2.8). These values will be used in the equations to determine the various sediment properties. Because the primary purpose of developing an in situ seismic method is to eliminate measurements on disturbed core samples, consideration has been given to the measurement of the bulk density in situ using a nuclear gauge. The use of gamma rays to obtain bulk density in marine sediments has been successfully accomplished by Preiss (1968) and Keller (1965).

3.1.3 Viscoelastic Model

The seismic parameters to be measured are the compressional-wave velocity (V_p), the shear-wave velocity (V_s), the compressional-wave attenuation coefficient (a_p), the shear-wave attenuation coefficient (a_s), and the bulk density (ρ). These properties were chosen because if a viscoelastic solid model is used as a model for the ocean floor,

then density, and at least four other physical properties, must be known to determine various other sediment properties. A viscoelastic model is favored over a Hookean model because the Hookean model does not explain the attenuation of seismic waves in marine sediments (Hamilton et al, 1970).

To account for this attenuation, Bucher (1964), Hamilton, et al (1970), and White (1965) replaced the rigidity (μ), incompressibility (K), and Lamé's constant (λ) by the complex Lamé constants ($\lambda_R + i\lambda_I$), ($K_R + iK_I$) and ($\mu_R + i\mu_I$) in the equations of elasticity. However, the linear viscoelastic model for a homogeneous isotropic medium discussed by Flügge (1967) and Fung (1967) appears to be the best model for the sea floor. The pertinent equations which result from the theory of Flügge and Fung are listed in section 4.3.2 of the appendix. Section 4.3.1 summarizes the notation used, and section 4.3.3 shows the relationships between the measured sediment properties and various other properties.

3.1.4 Time-Distance Curves

For the in situ seismic method described in this report, the shear-wave velocity is found from a particular wave arrival containing information about the shear wave. To determine the best wave arrival from which the shear wave velocity can be found, several time-distance curves were constructed for a simple three-layer model where three source-receiver combinations were considered. The source-receiver combinations were an impulsive source in the water with the receiver on the bottom; an impulsive source and receiver both on the bottom;

and a S_H -source and receiver both on the bottom. The method used in constructing these time-distance curves is outlined by Griffiths and King (1965). The method consisted of calculating the time-distance relationship for each wave arrival and drawing its curve on a time-distance graph. Multiple reflections and surface waves were neglected in the calculations. Reasonable values were chosen for the compressional wave velocity (V_p), shear-wave velocity (V_s), and depths (d) of the layers. Figures 3-1, 3-2 and 3-3 are examples of each source-receiver combination. In the graphs, the symbol "p" represents the compressional wave, " S_V " represents the shear wave polarized in such a manner that the particle motion is in a vertical plane, and " S_H " represents the shear wave polarized in the horizontal plane.

For an impulsive source in the water and receiver on the bottom, it was concluded that wave arrivals containing information about the shear-wave velocity would be hidden by various reflected and refracted waves or would have amplitudes extremely small compared to the expected amplitude of the direct P-wave. Amplitude calculations were accomplished using the equations of Ewing (1957).

For the source and receiver on the bottom, it was concluded that the direct S_V -wave could be theoretically identified on a seismogram if a vertical geophone is employed. All the other wave arrivals from which the shear-wave velocity could be obtained were found to arrive too late and, consequently, would be hidden by various compressional waves.

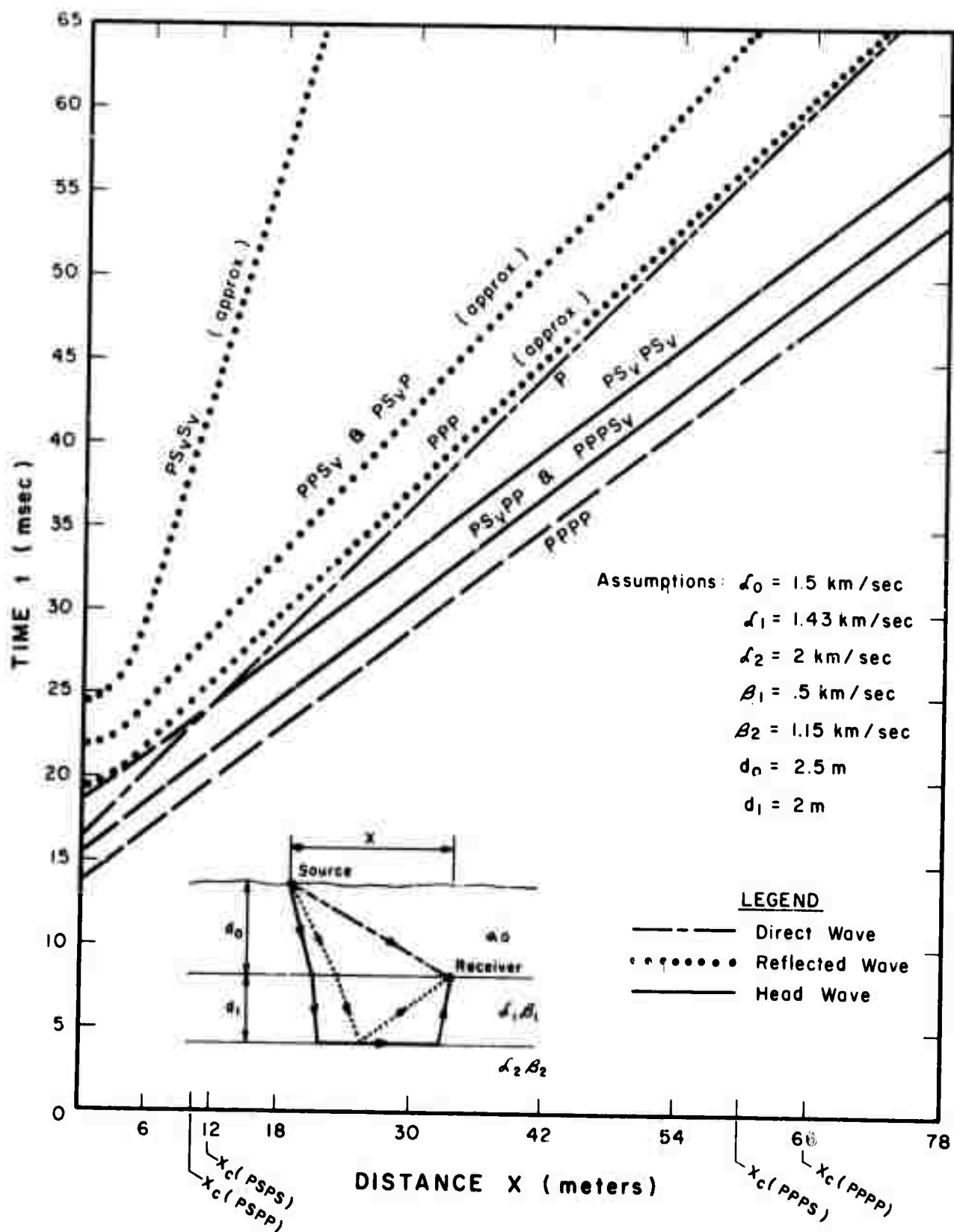


Figure 3-1. Theoretical time-distance graph for source on water surface and receiver on bottom.

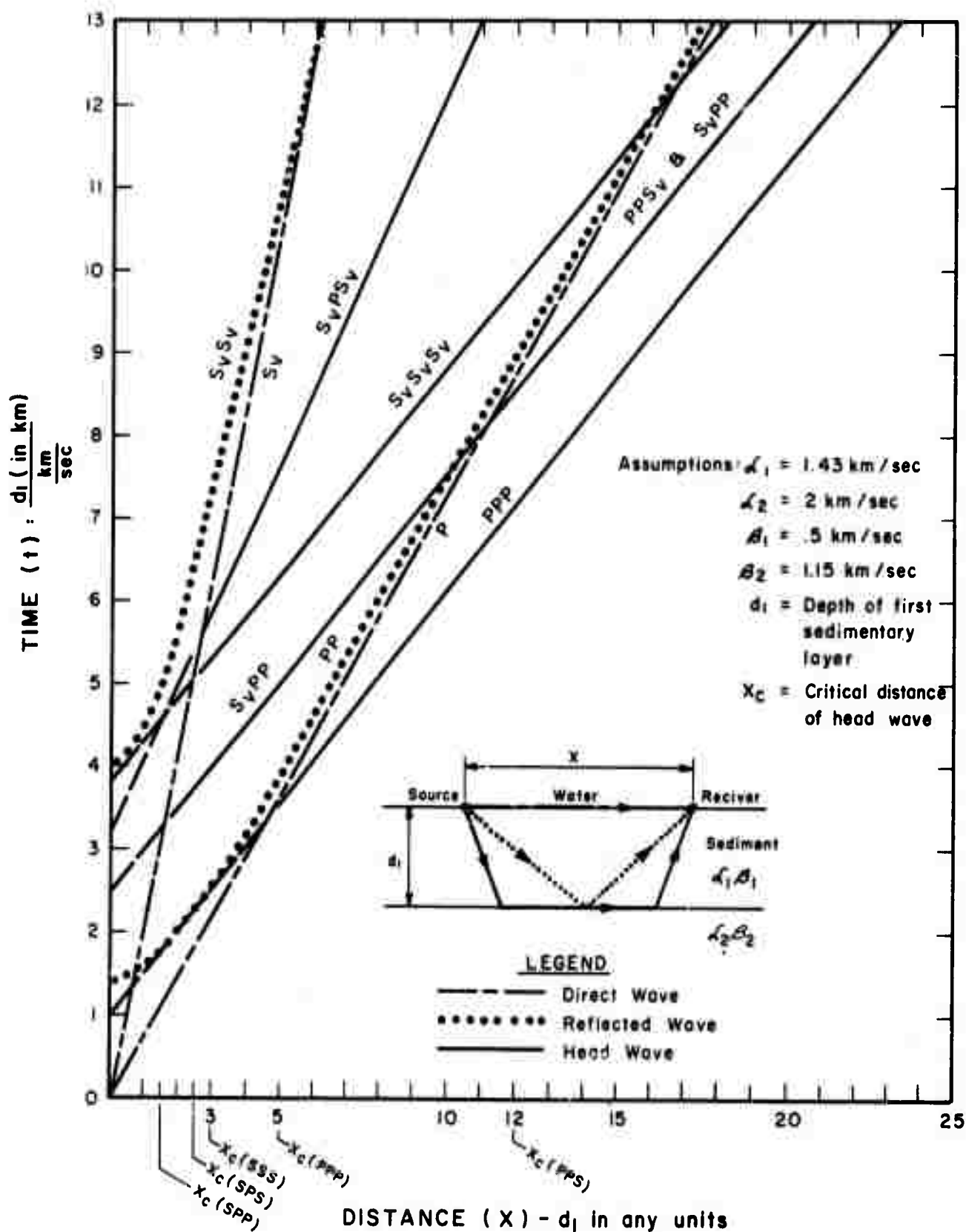


Figure 3-2. Theoretical time-distance graph for both source and receiver on bottom.

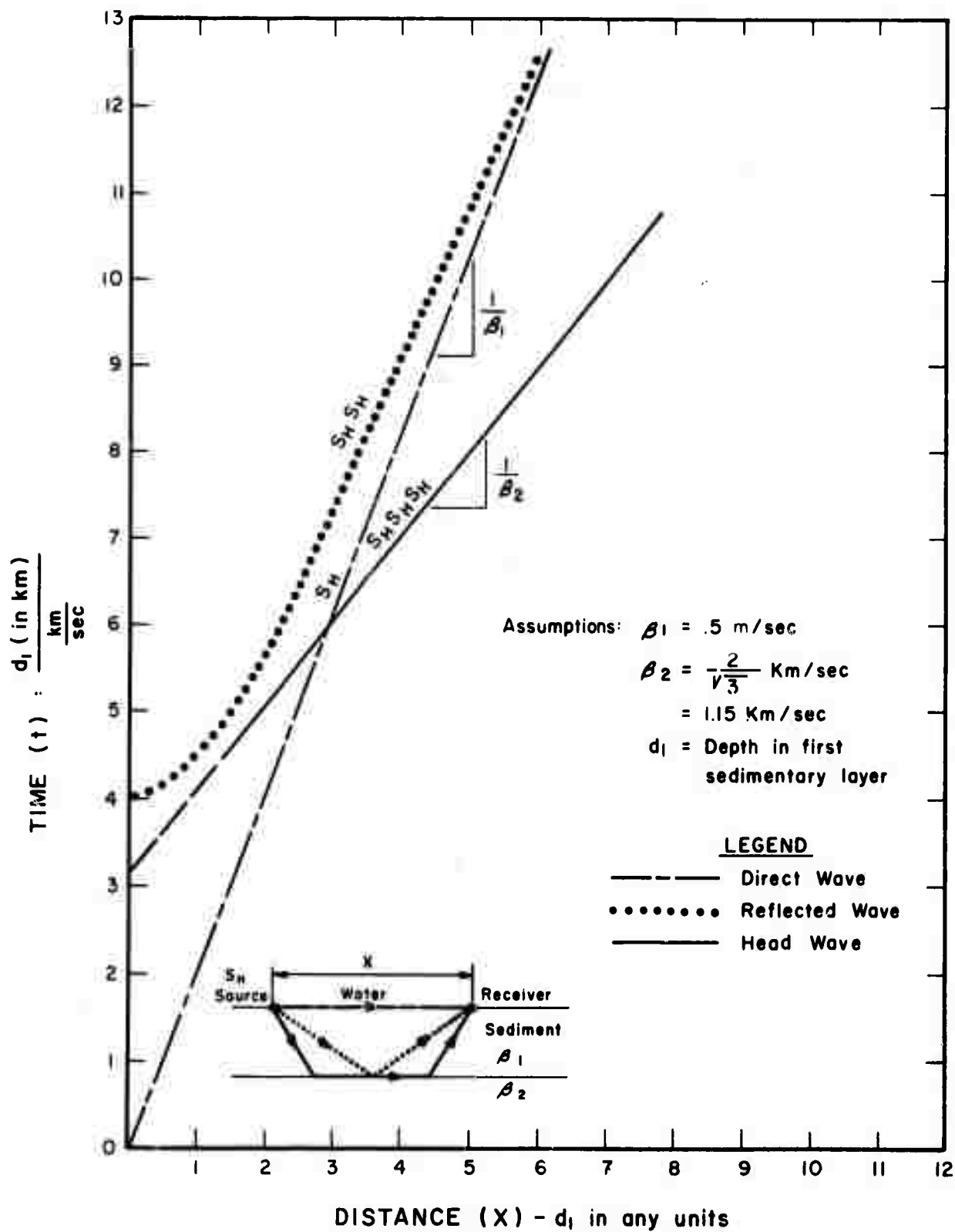


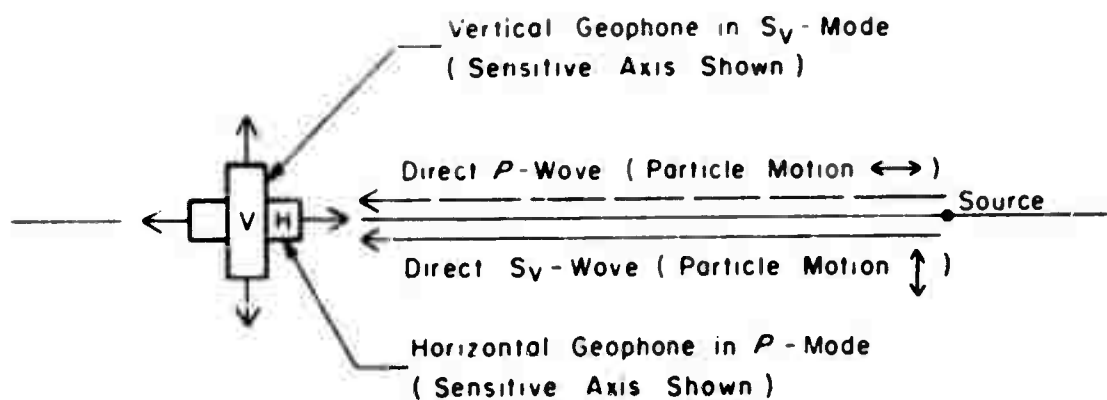
Figure 3-3. Theoretical time-distance graph for S_H -source and receiver both on bottom.

The particle motion produced by the direct S_V -wave is vertical and perpendicular to its line of propagation. Thus, if a vertical geophone is implanted in the bottom with its sensitive axis parallel to the ground motion produced by the direct S_V -wave, the first arrival on a seismogram should be the direct S_V -wave. This orientation of a vertical geophone to produce a large response to the direct S_V -wave will be referred to as the " S_V -mode".

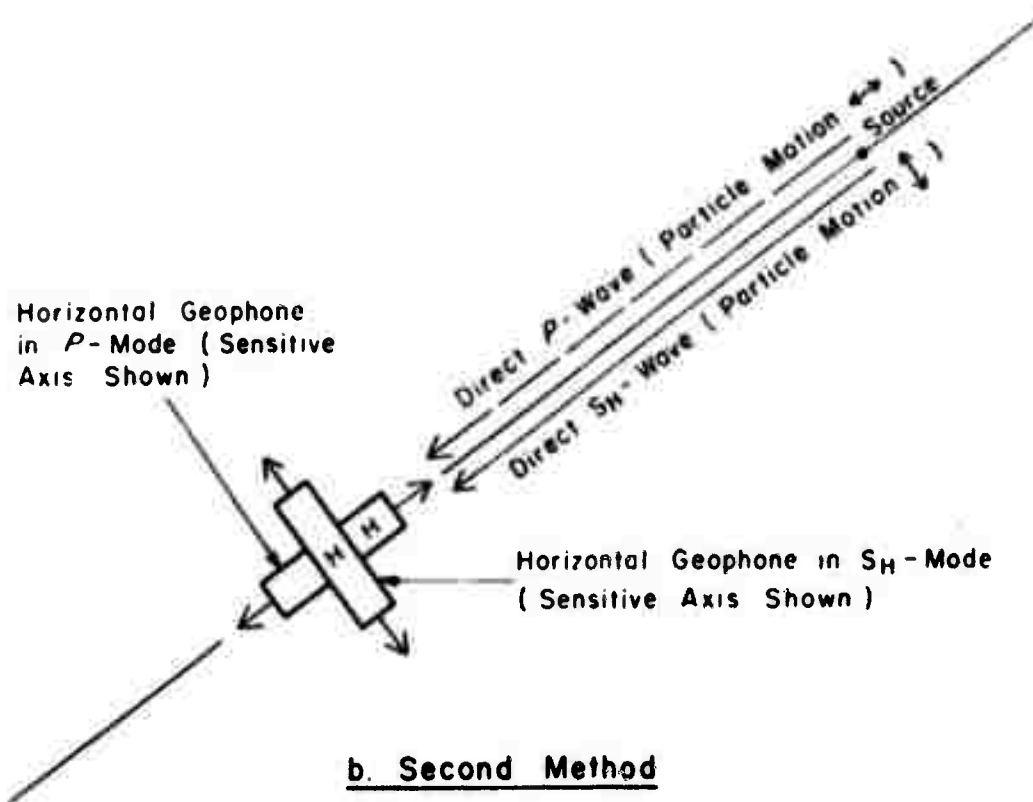
The compressional-wave velocity for a source and receiver on the bottom may be obtained in a similar manner. Because the particle motion of a compressional wave is in the direction of propagation (i.e. radial), a horizontal geophone with its sensitive axis directed toward the source would produce a large response to the direct P-wave. This orientation of a horizontal geophone will be referred to as the "P-mode".

Therefore, one of the proposed seismic methods was the orientation of a horizontal geophone in the P-mode and a vertical geophone in the S_V -mode. The compressional-wave velocity and the shear-wave velocity would be determined from the direct P-wave and direct S_V -wave, respectively. This proposed seismic method is shown in figure 3-4a.

For the S_H -source and receiver on the bottom, it was concluded that the direct S_H -wave was the only wave that could be efficiently identified on a seismogram. A horizontal geophone could be oriented so that its sensitive axis is parallel to the ground motion of the direct S_H -wave (the ground motion being horizontal and perpendicular to the line of propagation). This orientation of a horizontal geophone will be referred to as the " S_H -mode". Using the S_H -mode, the first arrival should be the direct S_H -wave.



a First Method



b. Second Method

Figure 3-4. Two proposed seismic methods.

The compressional-wave velocity can be obtained with a horizontal geophone in the P-mode. Therefore, the second proposed method employed the use of a S_H -source and two horizontal geophones--one oriented in the P-mode and the other oriented in the S_H -mode (figure 3-4b).

Experiments were conducted to determine which of the two proposed seismic methods would be the most feasible in marine sediments.

3.1.5 Description of Experiments

Experiments to determine the shear-wave and compressional-wave velocities were conducted in three environments. The first environment was a sand box containing unconsolidated, moist sand; the second was a beach near the shoreline where the sediment was sand and gravel, and the last was in 3 feet of water at a beach on San Francisco Bay where the sediment was also sand and gravel.

Sand Box Tests.

The first experiments, conducted in a large sand box, were to determine which of the two proposed seismic methods would be best to obtain the shear-wave velocity. A sand box was chosen because it was located in a building where equipment and facilities were readily accessible. The box was 15 feet square and overlaid a concrete bottom at a depth of 3 feet. Although the sand was moist and very unconsolidated, it was unsaturated so only a rough idea of the feasibility of the proposed seismic methods was determined.

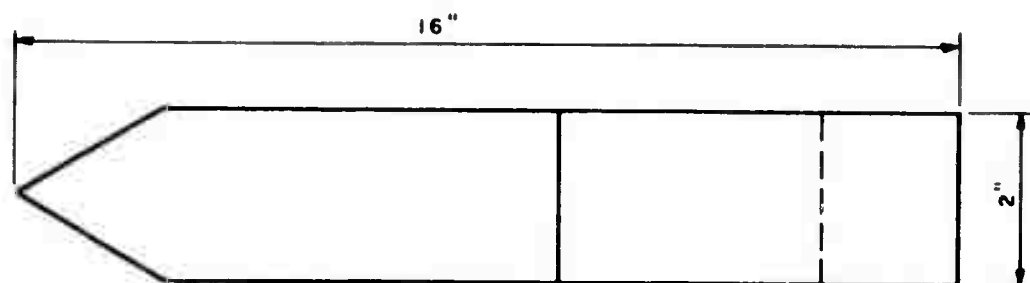
A 12-pound sledge hammer and an impacting plate (8 inches x 8 inches) were used as a source of energy to produce, in particular, S_V -waves and P-waves. The hammer contained an inertia switch so that

the hammer impact would trigger the recording devices. The S_H -source consisted of a carpenter's hammer and a metal stake. The S_H -source and the method of production of S_H -waves are shown in figure 3-5. The recorder was triggered as the triggering circuit was closed when the hammer forced the flexible metal strip against the base of the stake.

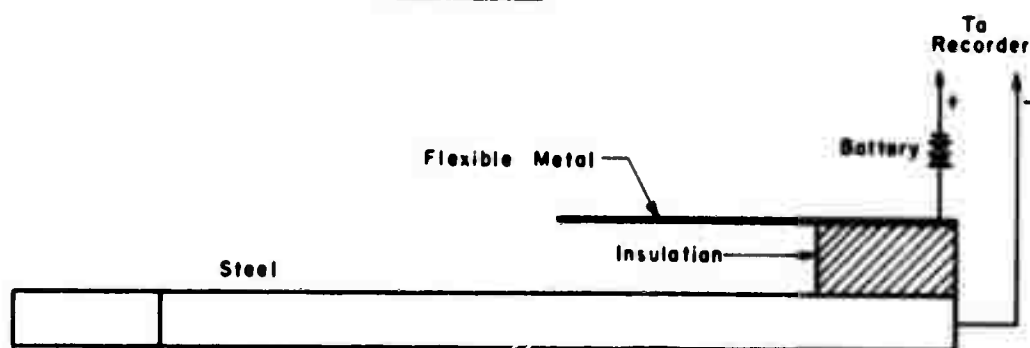
The horizontal geophone used in detecting the ground motion was a Hall Sears geophone with a natural frequency of 4 Hz. The vertical geophone employed was a Hall Sears Model HS-5-L1 which has a natural frequency of 14 Hz. These phones were placed firmly in the sand. Then 1-foot intervals were marked off with a tap measure. From station-to-station, energy was transmitted into the ground using the seismic sources, and the resulting ground motion detected by the geophones was recorded for the various modes of operation.

Beach Tests.

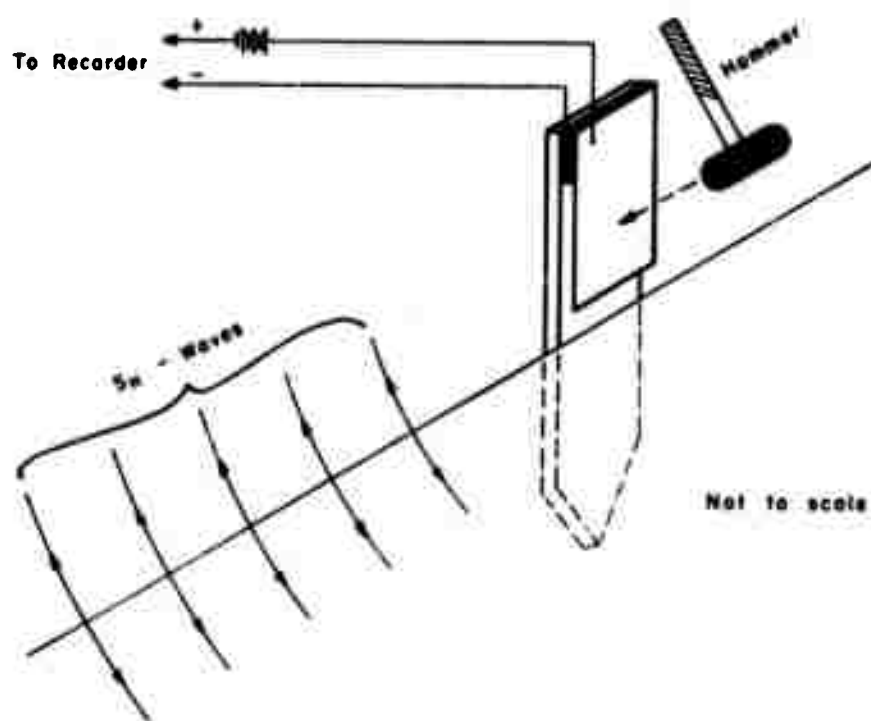
Because satisfactory results were obtained in a moist, unconsolidated sediment in identifying the arrival of the direct P-wave and direct S_H -wave, experiments were conducted next in a slightly undersaturated sediment employing two horizontal geophones (one in the S_H -mode and the other in the P-mode). A sand and gravel beach was chosen as the field site. Using the FS-3 refraction recorder (sec. 3.1.6.1), experimental runs were conducted on the beach near the shoreline. For the S_H -mode the S_H -source was used while the hammer and plate were used for the P-mode.



Top View



Side View
Metal Stake



Method of Production of S_H - Waves

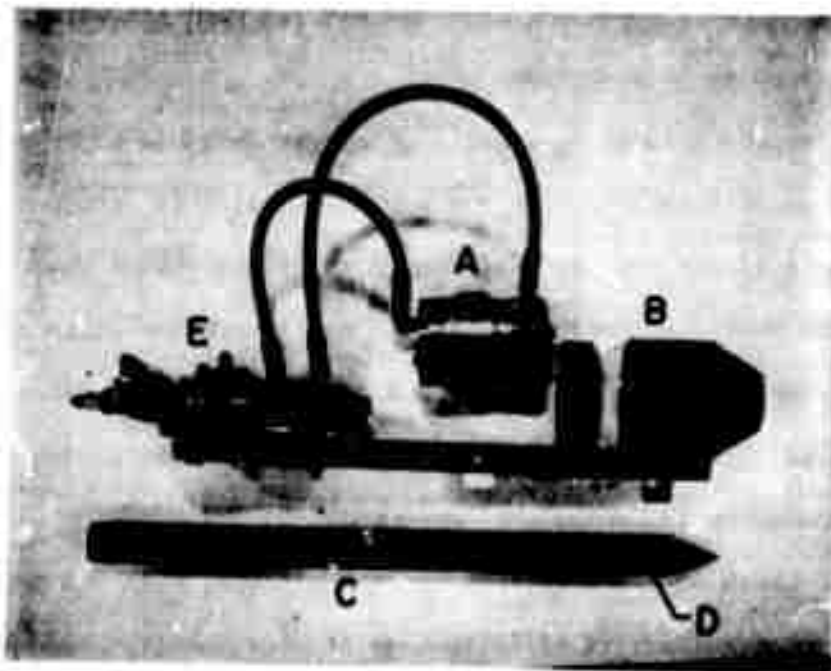
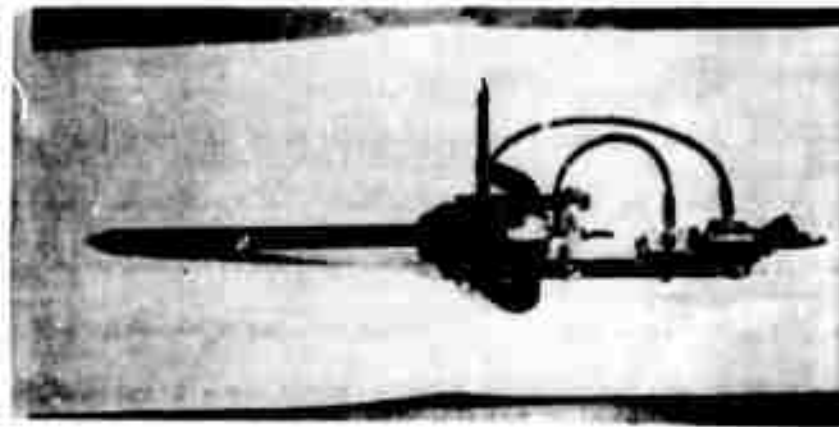
Figure 3-5. Method of generating S_H - waves for experiments conducted on land.

Shallow Water Tests.

In order to calculate the shear-wave velocity and the compressional-wave velocity in an actual marine sediment, a S_H -source had to be designed for underwater use. Several sources were investigated with consideration given to their energy, capability of producing S_H -waves, and ease of operation. Some of the sources investigated were blasting caps, capacitors, air guns, and regular rifle cartridges. The source finally decided upon was a small 3-cubic-inch air gun with the capability of being reduced to 1-cubic-inch.

To produce a large S_H -wave, a probe was designed to be attached to the air gun (figure 3-6). As the probe is implanted into sediment, water and a little sediment will enter the probe. When the air gun is fired, the sudden expansion of the air will force the water and sediment out the side of the probe. The force of this stream of water and sediment will cause a rotational movement, generating a large S_H -wave perpendicular to the rotational movement.

At a beach on San Francisco Bay the air gun, with the probe attachment, was tested for its effectiveness of producing S_H -waves. The field site was in 3 feet of water. The exit port on the probe was implanted by hand to a depth of 1 foot into the sediment. Two geophone units (each contained a vertical geophone and horizontal geophone) were implanted at a distance of 3 feet and 5 feet from the air gun. The horizontal geophone was oriented in the S_H -mode. The four-trace oscilloscope, with camera attachment, was used for recording. The oscilloscope was triggered off the battery which triggered the solenoid of the air gun.



- A 3 in.³ Air Gun
- B Adapter
- C Probe (1 1/2')
- D Exit Port on Probe
- E Solenoid

Figure 3-6. Marine S_H - source.

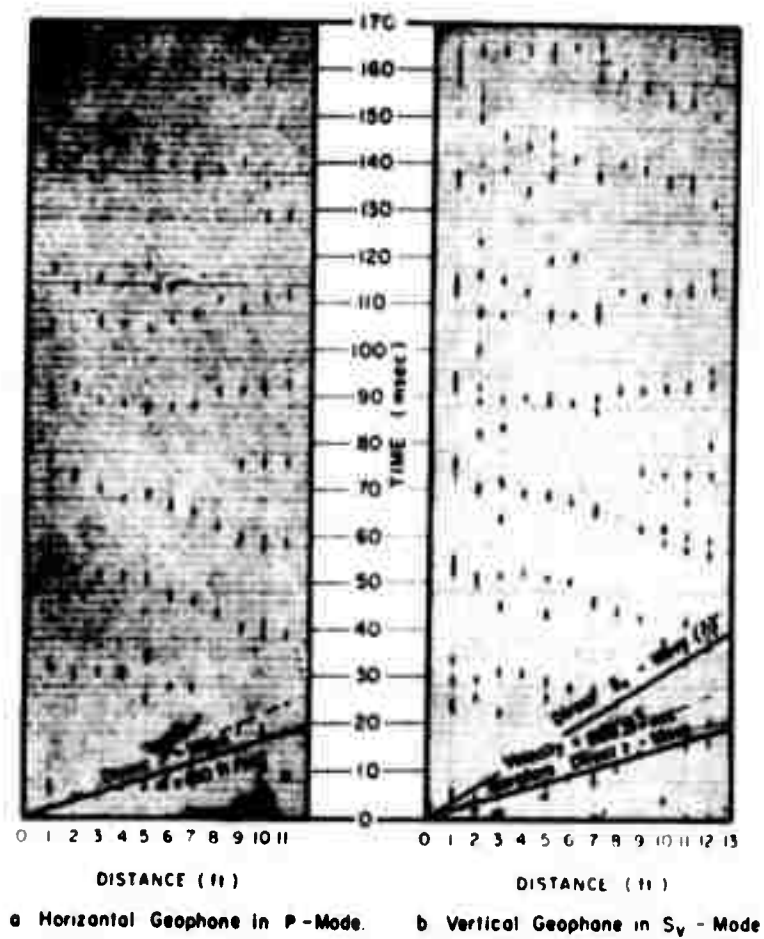
Unfortunately, the piston, when returning to its initial position after firing the air gun, sucked sediment into the probe. The probe of the air gun eventually became obstructed with sediment. This limited the number of shots for every implant of the probe (a maximum of three shots achieved). Sometimes the probe became obstructed just from inserting it into the sediment. Consequently, a little data was accumulated.

3.1.6 Data Acquisition and Results

Refraction Unit.

One method of recording the wave arrivals was the use of a refraction unit (Huntec model FS-3 Portable Facsimile Seismograph), a single-channel time-distance plotting instrument. The record, produced on electro-sensitive paper, is in the form of short dashes which represent the positive zero crossings of each cycle of the wave arrivals.

To determine the feasibility of the proposed seismic method employing a vertical geophone in the S_V -mode and a horizontal geophone in the P-mode, experimental runs in the sand box were conducted first in the P-mode and then in the S_V -mode because the refraction unit is a single-channel instrument. The source employed was the sledge hammer and impacting plate. Figure 3-7a shows one of the time-distance records produced with the horizontal geophone in the P-mode. The line drawn in the record represents the direct P-wave. The results for the compressional-wave velocity are listed in table 3-1 for three experimental runs.



(Source; sledge hammer and Impacting plate.)

Figure 3-7. Time-distance records from unconsolidated sand.

Figure 3-7b is an example of a record produced with the vertical geophone in the S_V -mode. The velocities obtained from the inverse slope of the first arrival for three experimental runs gave the velocity of the compressional wave. The results are listed in Table 3-1. Therefore, with the refraction unit, it can be concluded that the shear-wave velocity cannot be obtained from the first arrivals with the geophone oriented in the S_V -mode. With difficulty, it was possible to draw the curve that appeared to be the direct S_V -wave on some of the records.

Table 3-1.--Wave velocities in unconsolidated sand using refraction unit

		Compressional-wave velocity(ft/sec)	Shear-wave velocity(ft/sec)
First proposed seismic method	P-mode:	610	-
		610	-
		63	-
	S_V -mode:	665	-
		610	-
		650	-
Second proposed seismic method	P-mode:	-	-
		-	-
		-	-
	S_H -mode:	-	324
		-	308
		-	334

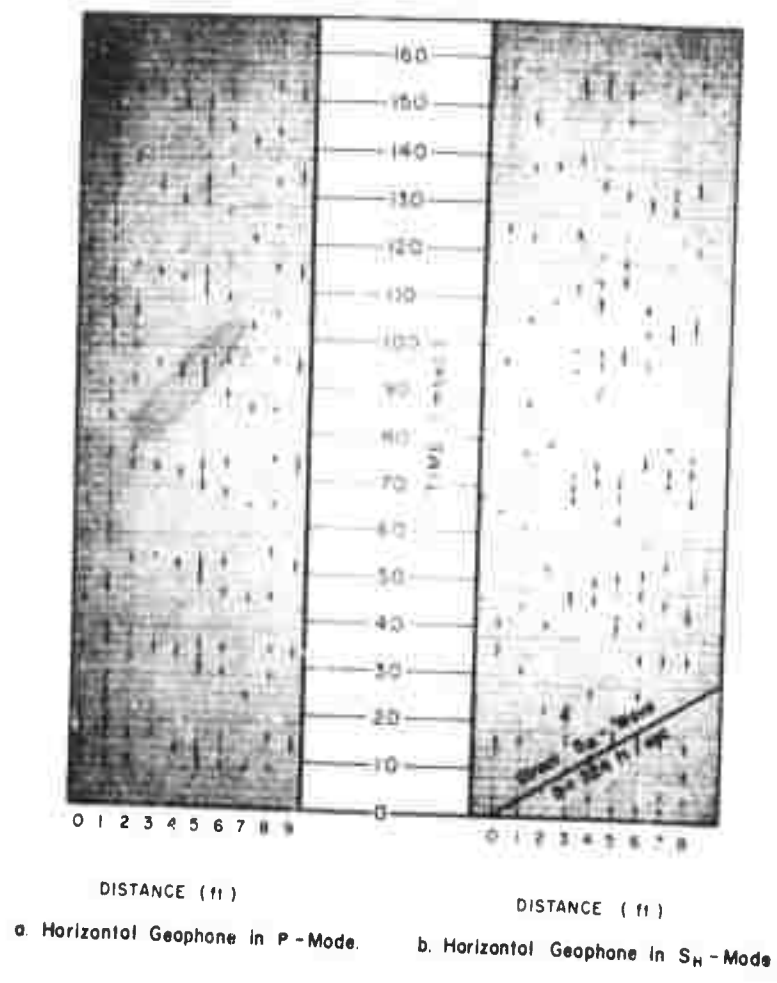
Next, the determination of the shear-wave velocity and compressional-wave velocity, using the second proposed method, was conducted in the sand box. With the S_H -source, records were produced with the horizontal geophone oriented first in the P-mode and then in the S_H -mode.

Figure 3-8a shows an example of the records produced with the horizontal geophone oriented in the P-mode. No direct P-waves were present on the records, revealing that the S_H -source does not produce direct P-waves of sufficient energy to trigger the refraction unit. However, the direct S_H -wave was seen with the horizontal geophone oriented in the S_H -mode. Figure 3-8b shows one of the records and Table 3-1 lists the calculated values for three experimental runs. From the beach tests, both the direct S_H -wave and the direct P-wave were identifiable on the records. Samples of the results are shown on figure 3-9.

Dual Beam Oscilloscope with Camera.

The second type of recording instrument used was a dual beam oscilloscope (Tektronix type 555). Because this oscilloscope has two independent inputs, the outputs from two geophones were traced simultaneously on the screen. To record the wave arrivals, a camera was attached to the oscilloscope screen. Polaroid type 47 photographic film (3000 ASA Speed) was used.

The same operational procedures were employed to determine the feasibility of the two proposed seismic methods as were conducted with the refraction unit. First, the seismic method with a vertical geophone in the S_V -mode and a horizontal geophone in the P-mode was tested in unconsolidated sand using the sledge hammer and impacting plate as the source. An example of a typical picture obtained is shown in figure 3-10a. A time-distance graph constructed from first arrivals from several pictures is shown in figure 3-11 and reveals that the first arrival at both geophones is the direct P-wave. The results of two experimental runs are listed in Table 3-2.



(S_H - Source.)

Figure 3-8. Time-distance records from unconsolidated sand.

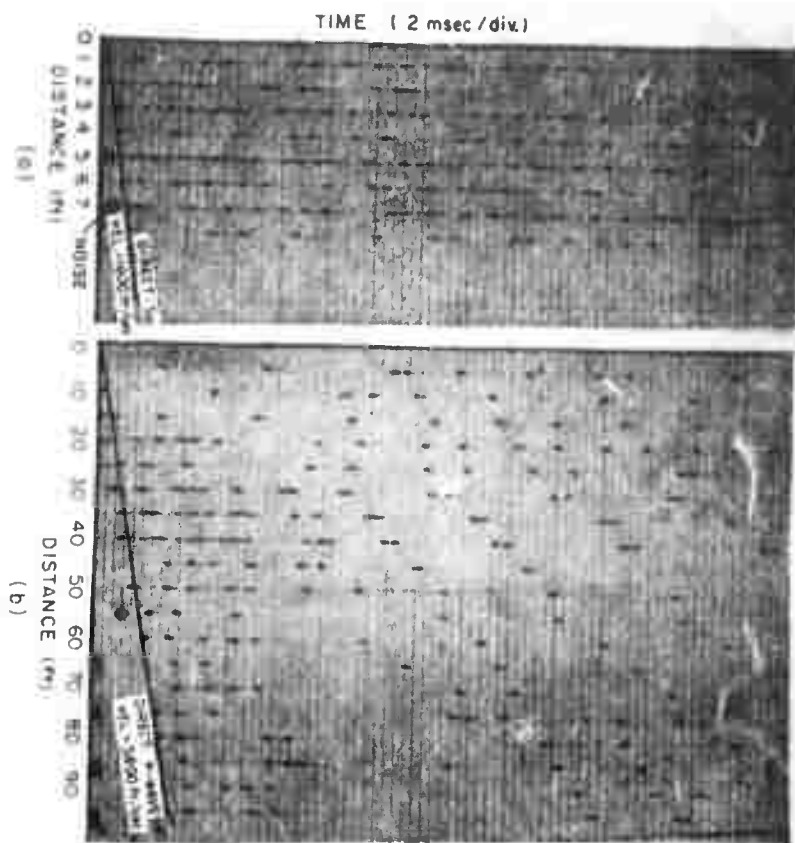
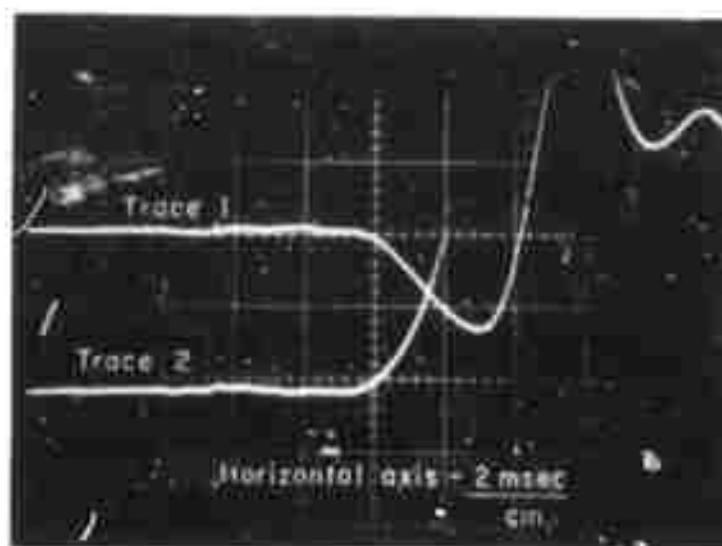
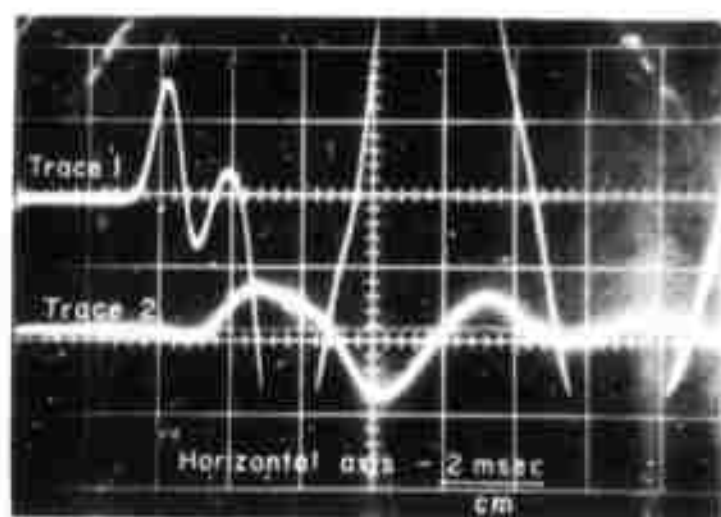


Figure 3-9. Time-distance records from beach experiments.

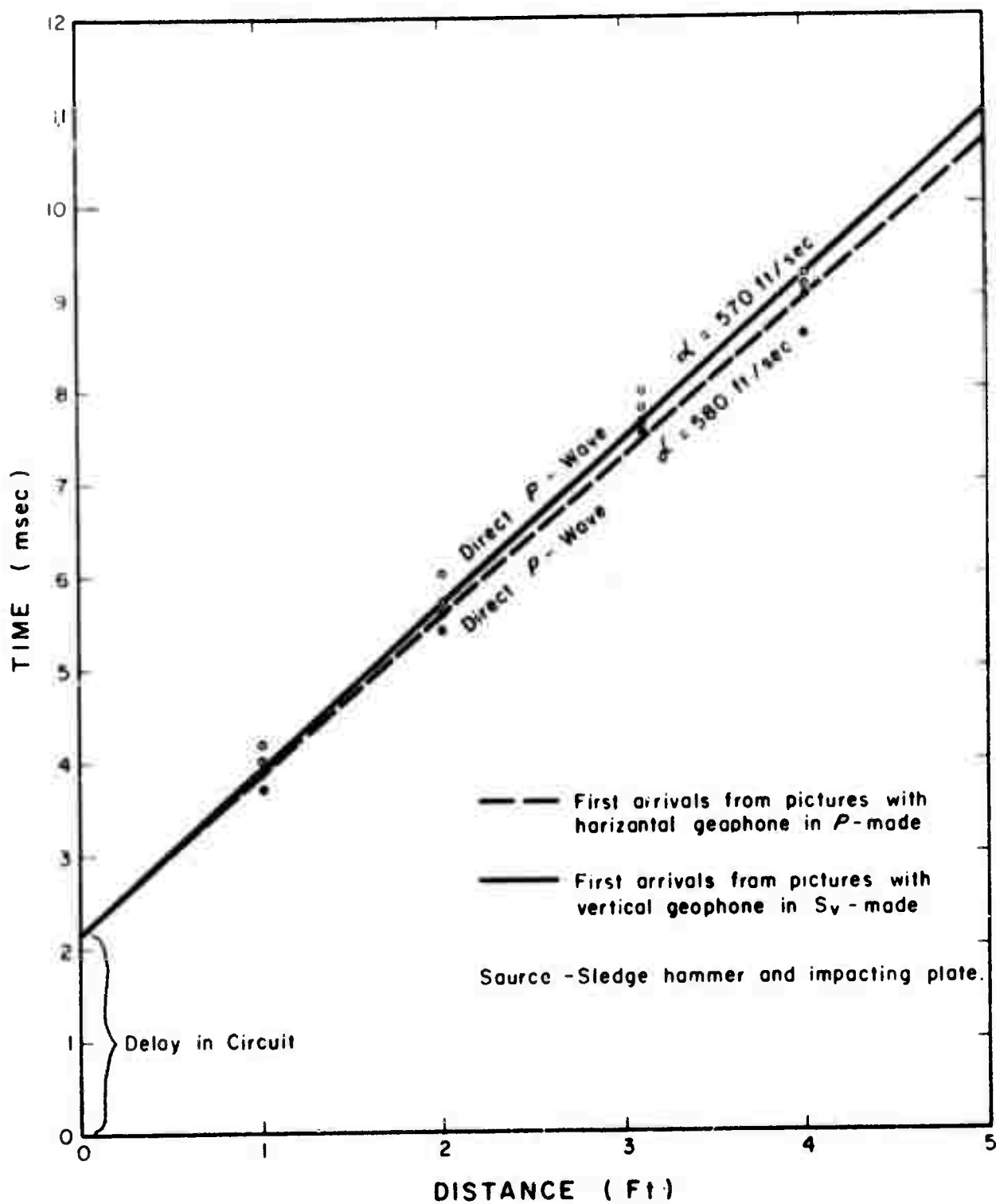


- a. Output of vertical geophone in S_V -mode (trace 1) and of horizontal geophone in P -mode (trace 2) - [sledge hammer and plate source ; source-receiver separation = 4 feet.]



- b. Output of vertical geophone in S_V -mode (trace 1) and of horizontal geophone in S_H -mode (trace 2) - [S_H source ; source-receiver separation = 1 foot.]

Figure 3-10. Geophone records - unconsolidated sand.



(Horizontal geophone in P-mode; vertical geophone in S_v-mode.)

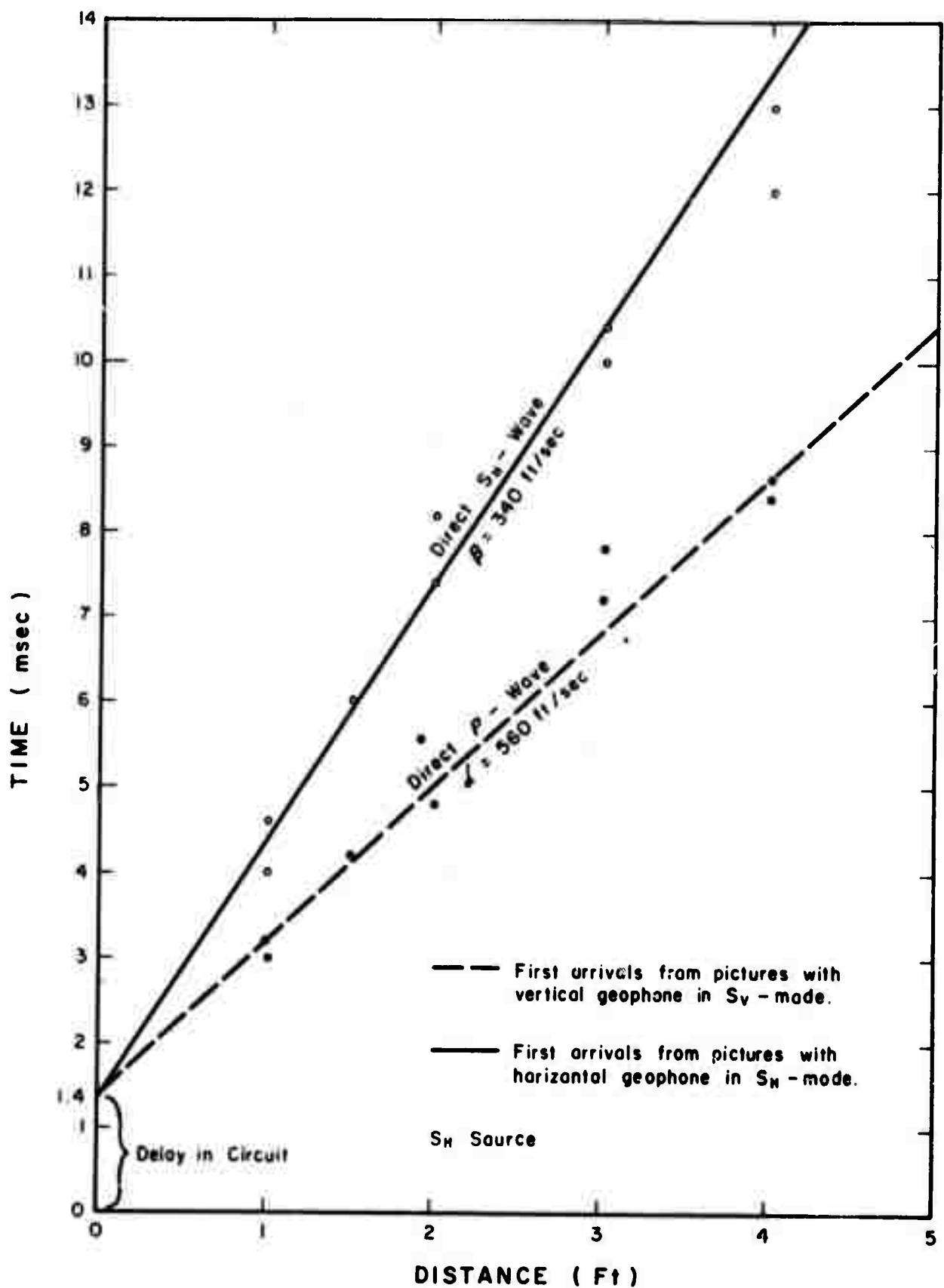
Figure 3-11. Time-distance plots - unconsolidated sand.

The second operation consisted of orienting the horizontal geophone in the S_H -mode. Because only one horizontal geophone was available, experimental runs could not be conducted with a horizontal geophone in the S_H -mode and a horizontal geophone in the P-mode (i.e., the second proposed seismic method). However, previous results have shown that the compressional-wave velocity can be obtained from the first arrival produced by a vertical geophone in the S_V -mode; and therefore, a vertical geophone was used. Figure 3-10b shows one of the pictures taken using the S_H -source. Plots of first arrivals on a time-distance graph for two experimental runs are shown in figure 3-12. The graph shows that both the direct P-wave and the direct S_H -wave were obtainable, and their calculated velocities are listed in Table 3-2.

Table 3-2.--Results in unconsolidated sand using oscilloscope

		Compressional- velocity (ft/sec)	Shear velocity (ft/sec)
First proposed --	P-mode:	580	--
Seismic method	S_V -mode:	570	--
Second proposal --	S_V -mode:	560	--
Seismic method	S_H -mode:	--	340

Additional experiments were conducted in unconsolidated sand using the dual beam oscilloscope. However, the oscilloscope was converted to four traces by use of a Tektronix 1A4 plug-in (i.e., the oscilloscope was converted to a four-channel recorder). Furthermore, four geophone units were employed. Each unit consisted of a vertical geophone and a



(Vertical geophone in S_V -mode; horizontal geophone in S_H -mode.)

Figure 3-12. Time-distance plots - unconsolidated sand.

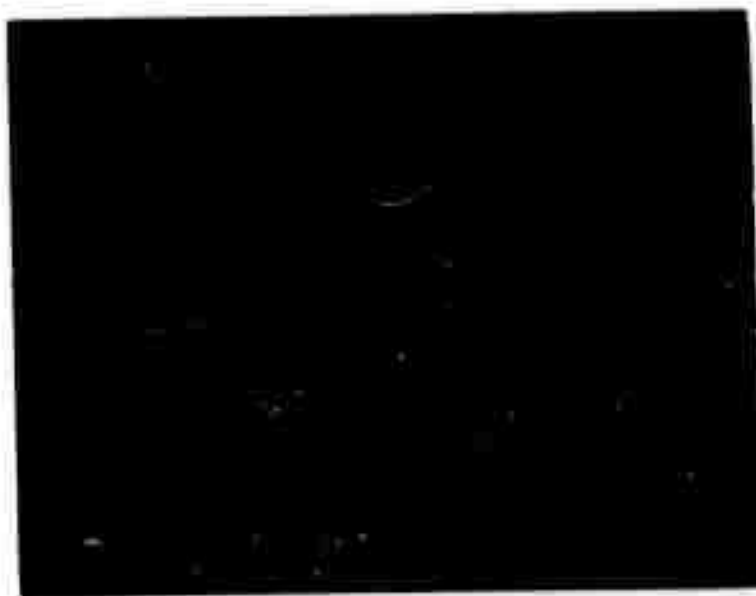
horizontal geophone (Geospace HS-5 Model K). These units were implanted in a line with the horizontal geophone oriented in the S_H -mode. A typical picture for the four horizontal geophones oriented in the S_H -mode is shown in figure 3-13a. The first arrival time of each of the four traces was determined and then plotted on a time-distance graph (figure 3-14). The inverse slope of the line obtained from these four points gave the shear-wave velocity from a single picture. The graph shows excellent results for five pictures taken.

The experiment was repeated using the four vertical geophones and the hammer and plate source. A typical record is shown in figure 3-12b, and the results of four pictures are plotted on a time-distance graph in figure 3-15. The compressional velocities obtained are listed in the graph.

For shallow water tests, one of the problems encountered in the oscilloscope recording was reading data values that were buried due to too large a time scale on the oscilloscope. It was difficult to measure the arrival time difference of the direct P-wave between the two vertical geophones. Figure 3-16 shows two pictures that were taken. By measuring the difference in arrival time of the direct P-wave and direct S_H -wave between their respective geophones and dividing by the geophone separation (2 feet), a compressional-wave velocity of 5,000 ft/sec was calculated from both pictures, and a shear-wave velocity of 340 ft/sec and 242 ft/sec was calculated from picture 1 and 2 of figure 3-16 respectively.

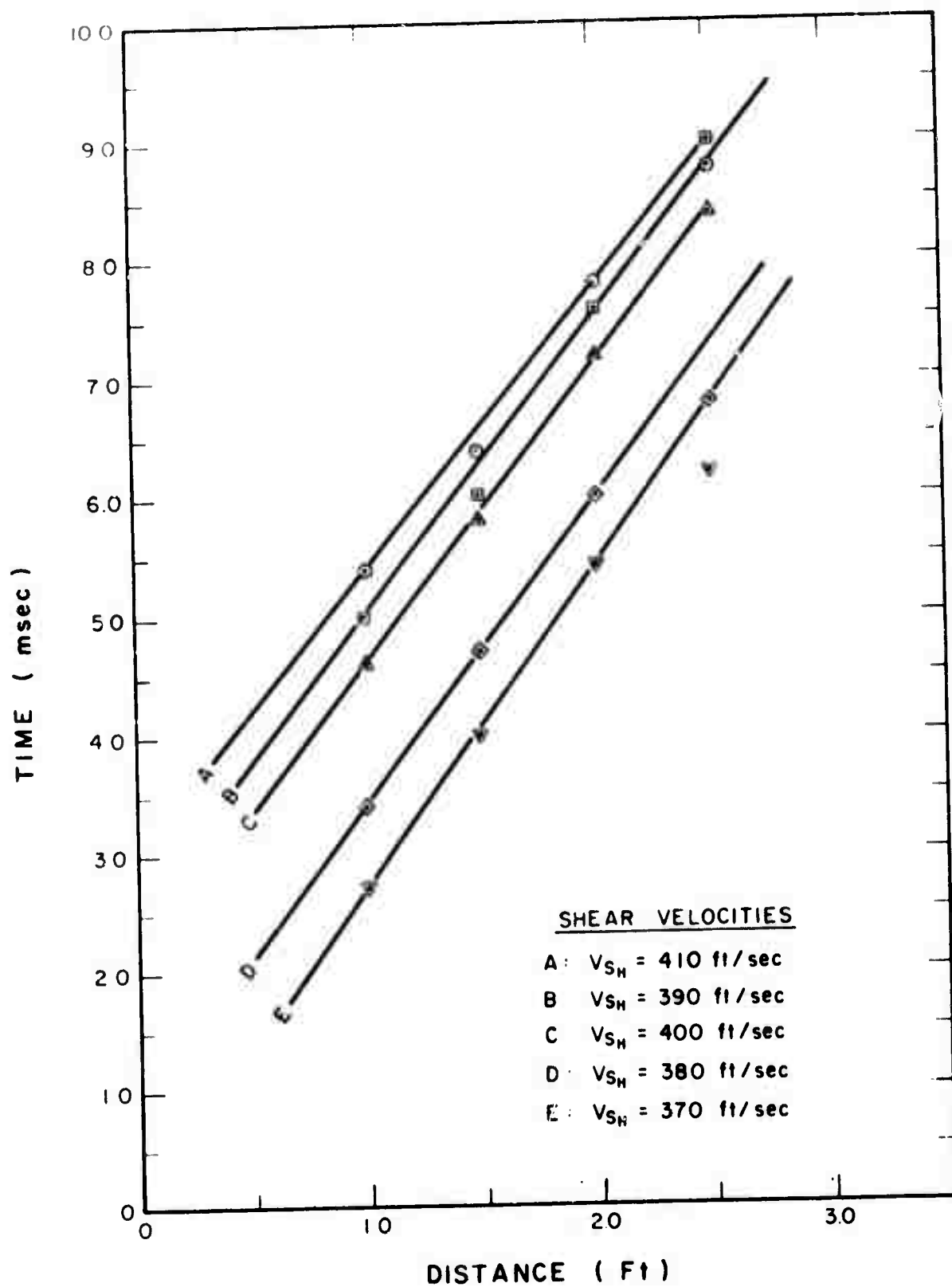


a. Wave arrivals from four horizontal geophones in S_H - mode
(source-receiver separation distance listed on traces.)



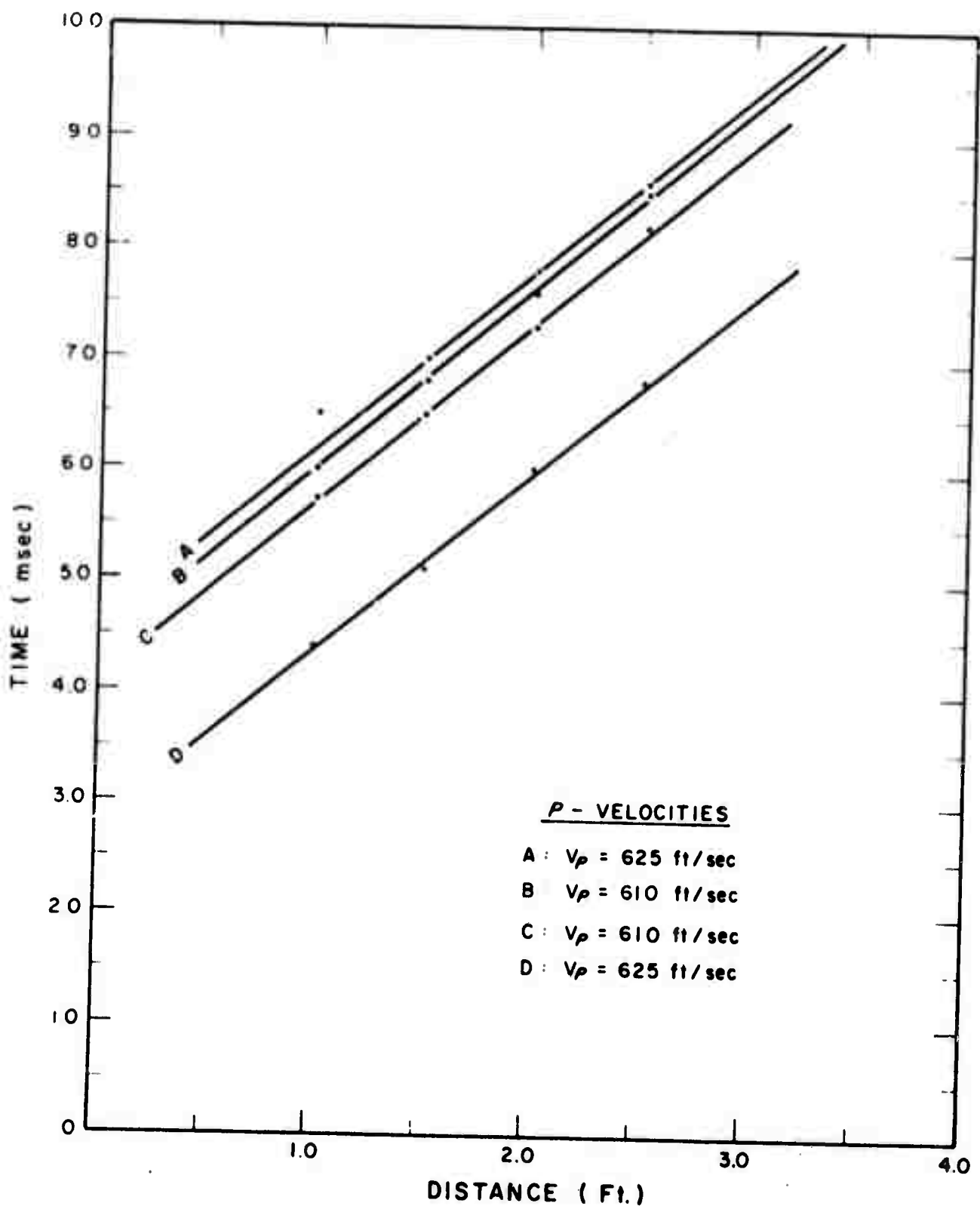
b. Wave arrivals from four vertical geophones in S_V - mode
(source-receiver separation distance listed on traces.)

Figure 3-13. Geophone records - unconsolidated sand.



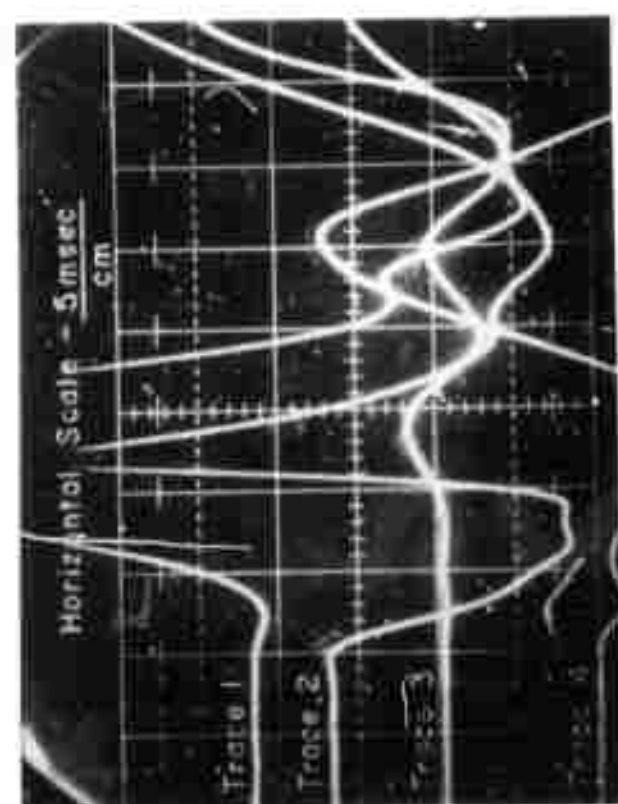
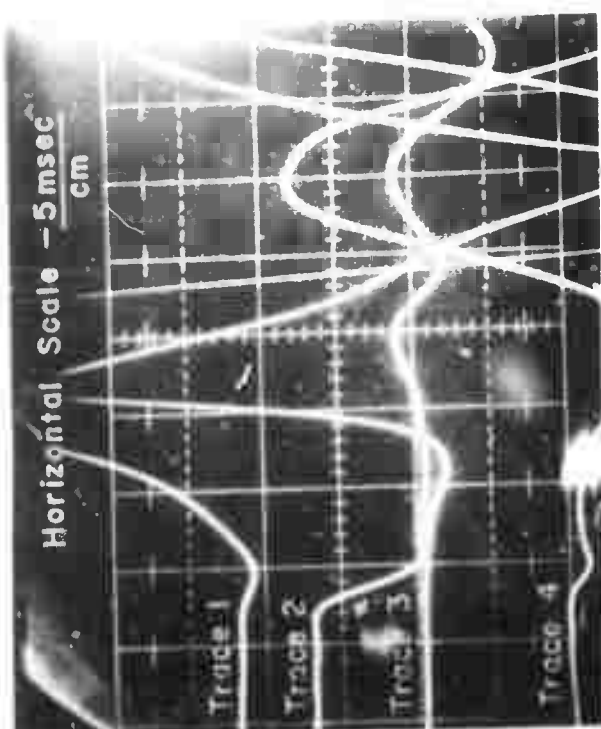
(Four horizontal geophones in S_H - mode.)

Figure 3-14. Time-distance plots - unconsolidated sand.



(Four vertical geophones in S_v - mode.)

Figure 3-15. Time-distance plots - unconsolidated sand.



PICTURE 1.

PICTURE 2.

On these pictures, traces 1 and 3 are the wave arrivals from the two horizontal geophones. The first arrival in each of these traces are the direct S_H - wave. Traces 2 and 4 are the wave arrivals from the two vertical geophones. The first arrival in each of these traces is the direct P -wave. Source was air gun with probe.

Figure 3-16. Geophone output - submarine sediments.

3.1.7 Conclusions and Recommendations

Of the two proposed seismic methods studied, only one proved to be feasible in determining the compressional-wave velocity and shear-wave velocity. The method consisting of a vertical geophone oriented to produce a large response to the direct S_V -wave and of a horizontal geophone to produce a large response to the direct P-wave was shown to give only the compressional-wave velocity and not the shear-wave velocity from first arrivals. This was due to the fact that either the vertical geophone was not implanted perfectly normal to the surface (if one assumes that the direct P-wave travels on the surface), or velocity increases with depth in the sediment, which would result in the direct P-wave making an arcuate path to the surface. Both would cause the ground motion of the direct P-wave to be detected by the vertical geophone.

The second proposed seismic method was shown to give both the shear-wave velocity and compressional-wave velocity from first arrivals in unconsolidated sand, on a beach of slightly undersaturated sand and gravel, and in San Francisco Bay in saturated sand and gravel. Using an S_H -source, the direct S_H -wave was seen in the records with a horizontal geophone oriented to produce a large response to the direct S_H -wave. For this method, the direct P-wave can be seen either with a horizontal geophone oriented to produce a large response to the direct P-wave or with a vertical geophone.

As may be seen from the experiments conducted, the primary goal to date has been the determination of a seismic method to obtain the shear-wave velocity. It is believed that by using the air gun with the probe attached, S_H -waves will be generated with sufficient energy to be detected.

After satisfactory results have been obtained at the beach using the air gun, an acoustically dead framework, on which will be attached the four geophone units and the air gun, will be designed and constructed. A sketch of the framework is shown in figure 3-17. Upon completion of the framework, the stations in San Francisco Bay, where core samples were taken (section 3.2.8), will be reoccupied. After determining the compressional-wave velocity, shear-wave velocity, and their attenuation coefficients, and using the value for bulk density determined from the core samples, the sediment properties in Table 3-3 will be calculated. Furthermore, an attempt will be made to find empirical relationships from which porosity, shear strength, bulk density, and mean grain size can be predicted from the in situ measurements of the compressional-wave velocity and/or the shear-wave velocity. These four sediment properties have been related to the compressional-wave velocity for various environments by Hamilton (1970b), Horn (1968), Schreiber (1968), and Lewis (1971).

Because the undisturbed bulk density is preferable for calculating the sediment properties for a viscoelastic solid model, consideration has been given to the construction of a nuclear density probe to be attached to the framework. Cesium 137 with a strength of 5 to 10 millicuries seems to be suitable radioisotope. It has a half life of approximately 30 years and emits a gamma photon with a discrete energy of .662 mev. A scintillation counter would be used to detect the electrons emitted by the sediment. The separation distance would be approximately 1 foot.

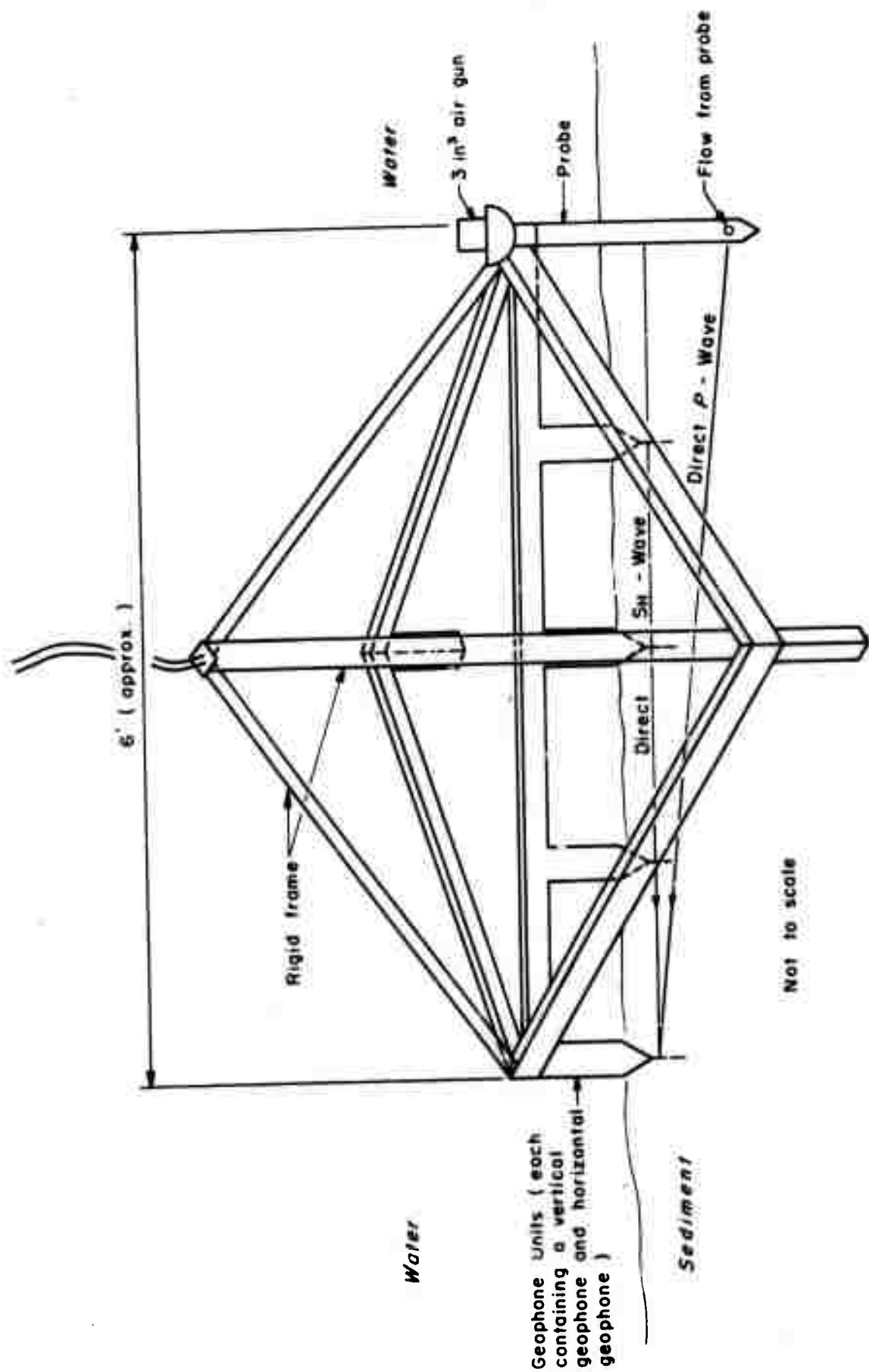


Figure 3-17. Probe for measurement of shear - wave and compressional - wave velocity.

3.2 Classification of Sea-Floor Sediments by a Ship Underway

3.2.1 Concept

The geologic nature of the sea floor has long been known to have certain intrinsic physical properties amenable to measurement by remote sensors as well as in situ devices. Acoustic soundings of the bottom and subbottom with seismic energy in the form of short pulses and recording the echo or reflected energy from acoustically reactive horizons has become a popular method employed by geophysicists to map the variability of the earth's geologic structure. Although it has been theoretically recognized that the method has application for determining mass physical properties of sediments and rock, the utilization has not developed. Requirements for this kind of data were minimal until ocean exploration began. The need for sea floor engineering properties and better knowledge of sediment distribution has prompted new interest. Two obstacles still remain and have limited widespread application of the methods. The first concerns the time consuming detail required in data processing and the second lies in the uncertainty involved in relating the attenuation or loss of seismic energy noted in continuous seismic profiling to parameters depicting the engineering and physical properties of the materials. The advent of the digital computer has overcome the first obstacle, but many more field exercises must be conducted to take measurements before a thorough understanding of the uncertainties of the second obstacle is possible. The work described herein entails one such exercise.

3.2.2 Procedure

A simple, straightforward approach to making acoustic measurements of the sea floor is described. Basically, it involves the continuous mapping of reflection coefficients by comparing the peak amplitude of the transmitted pulse (impulse) to the peak amplitude of the echo or reflected pulse (response). In this investigation the acoustic-reflection measurement is made at normal incidence and with both a wide-band 0-5 KHz (with center frequency at 2.5 KHz) sparker source and a discrete 41 KHz source. A semi-automated measurement system was designed and constructed to facilitate the acquisition of acoustic data on shipboard. Continuous recording of seismic events depicting the impulse-response functions for each of the two sources and their respective receivers is obtained. The peak amplitude measurements are taken from the zero line of the pressure wave train, measuring only the positive excursion from line.

The data presented in this report was developed without the aid of digital computer processing. Analog measurements were reduced manually from photographic reproduction of data acquired on analog magnetic tape. It was felt that the initial investigation should pursue this course to gain better familiarization with the signal/noise variations and understanding the physical (geometrical) problems encountered in making acoustic measurements of this type. Future plans will include machine processing which will undoubtedly enhance the precision and handling of the voluminous quantity of data.

3.2.3 Previous Investigations

The first analysis of acoustic transmission in seawater began during World War II when several investigators looked into submarine warfare applications (1946). Slant angle measurements at various frequencies and distances provided the first data on the sea floor geological environment. Attention was focussed on two aspects relating to wave propagation phenomena and sediments per se. In the period following the war, investigations by Liebermann (1948), Urlick (1954), Urlick and Saling (1962), Mackenzie (1960), McKinney and Anderson (1964) and Jones, et al (1964) were directed to the characteristics of sound transmission and reflection. Attention was not given to sea-floor sediments and their mass physical properties until the mid 1950s when investigations by Hamilton (1956), Shumway (1960), Sarmiento and Kirby (1962), Richards (1962) and Nafe and Drake (1963) commenced. Actual field measurements of reflectivity and correlations to sediment type, by a ship underway, were made by Taylor-Smith (1968), Taylor-Smith and Li (1966) and Breslau (1964 and 1967) in the mid 1960s.

The material presented in this section is another effort to obtain field measurements, but with a practical application in mind. The work generally follows the recommendations of Breslau (1967 and personal communications) that more investigations and measurements are needed over all water covered areas. This effort for purposes of satisfying both the objectives of the contractor (ARPA) and NOAA is limited to the Continental Shelf water depths. It is felt the practical application for sea-floor tunneling and excavation for foundations engineering,

mining (dredging) and defense purposes necessitate concentrating attention on this zone. Several technologic advances since the work performed by Breslau (1964 and 1967) are incorporated in the electronic systems used in this investigation.

3.2.4 Theory Developed

A simplified approach to a very complex physical process involving wave propagation, attenuation and absorption has been used in developing the model of the sea floor-water interface. The sea floor is considered as a plane interface between two fluids. Energy is focussed on a zone of about one square meter surface area. The backscattering strength associated with this surface area depends much on the roughness of the sea bottom. A smooth bottom acts as a mirror such that the reflected energy is concentrated on the specular direction. A rough bottom will reflect the energy more evenly in all directions. It is important to note that the terms "smooth" and "rough" must be considered in relation to the acoustical wave length. Where the wave length is only a few centimeters it is seen that a 100% smooth bottom is rare. Even small stones, holes or ripples will make the bottom rough in the sense considered here. When a sound wave strikes the sea bottom, part of the incident energy will be reflected. The reflected energy is spread in all directions with a typical distribution as shown in figure 3-18. The distribution is totally dependent on the roughness of the sea bottom. Figure 3-19 illustrates how the roughness of the topography can influence the bottom backscattering strength as a function of the grazing angle. The angle of incidence is seen to also play an important

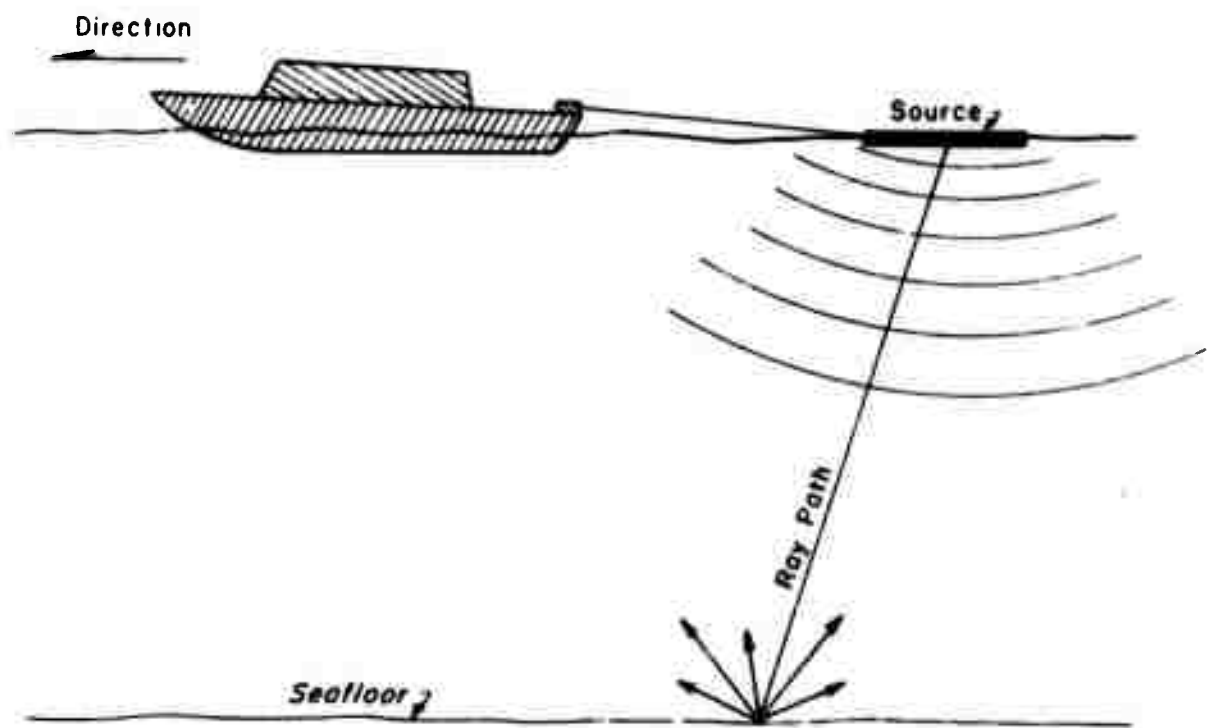


Figure 3-18. Seafloor scattering - specular energy.

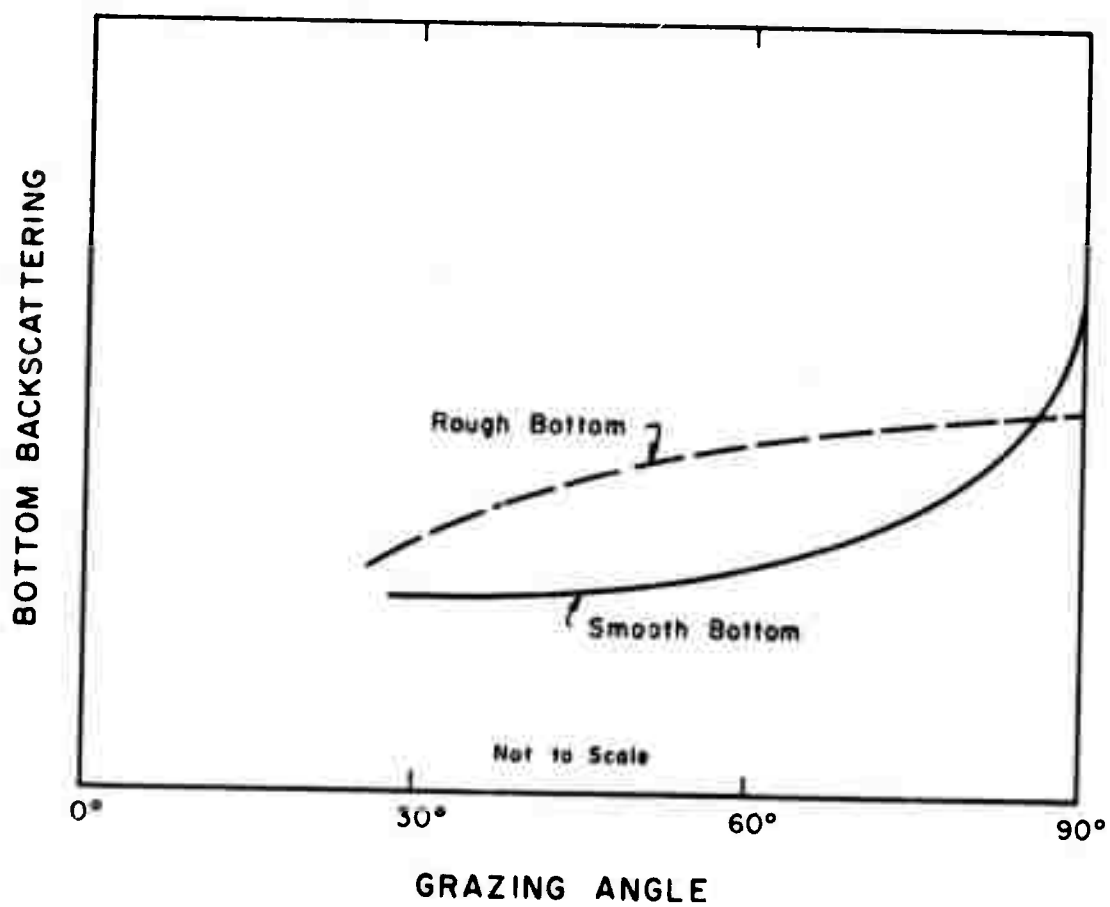


Figure 3-19. Typical curves for bottom backscattering strength (After Bodholt 1969).

role in determining the strength of the echo signal. The experiments in the following description were all conducted with the source and receiver set up to record normal incidence. It can be shown that theoretically the most accurate measurements of bottom backscattering strength should be obtained with a narrow beam transducer. If the beam width is $5-10^\circ$ between the 3dB points the bottom backscattering strength will vary only a few dB or less within the beam, of course depending on the type of bottom. The magnitude of the bottom sampling area will depend on the pulse length of the transmitted sound. The shorter the pulse the smaller the sampling area. Figure 3-20 illustrates the beam width, pulse length and area concept.

In the exercise conducted for this investigation, two sources are employed. One is an uncontrolled beam width emitting a .5 millisecond pulse length and the other is a narrow beam (7.5°) echo sounder having a pulse length of .25 millisecond.

Derivations.

A detail treatment of the mathematical description for acoustic wave propagation, reflection and absorption (bottom loss) is contained in the appendix (section 4.4) to this report. Several references were consulted and the best mathematical expressions relating to the experiments conducted in this investigation were taken from derivations by Breslau (1968).

From the derivations the most useful equations applicable to data reduction and processing are represented by defining the relationship between the fractional loss of intensity at the sea floor, K , and the

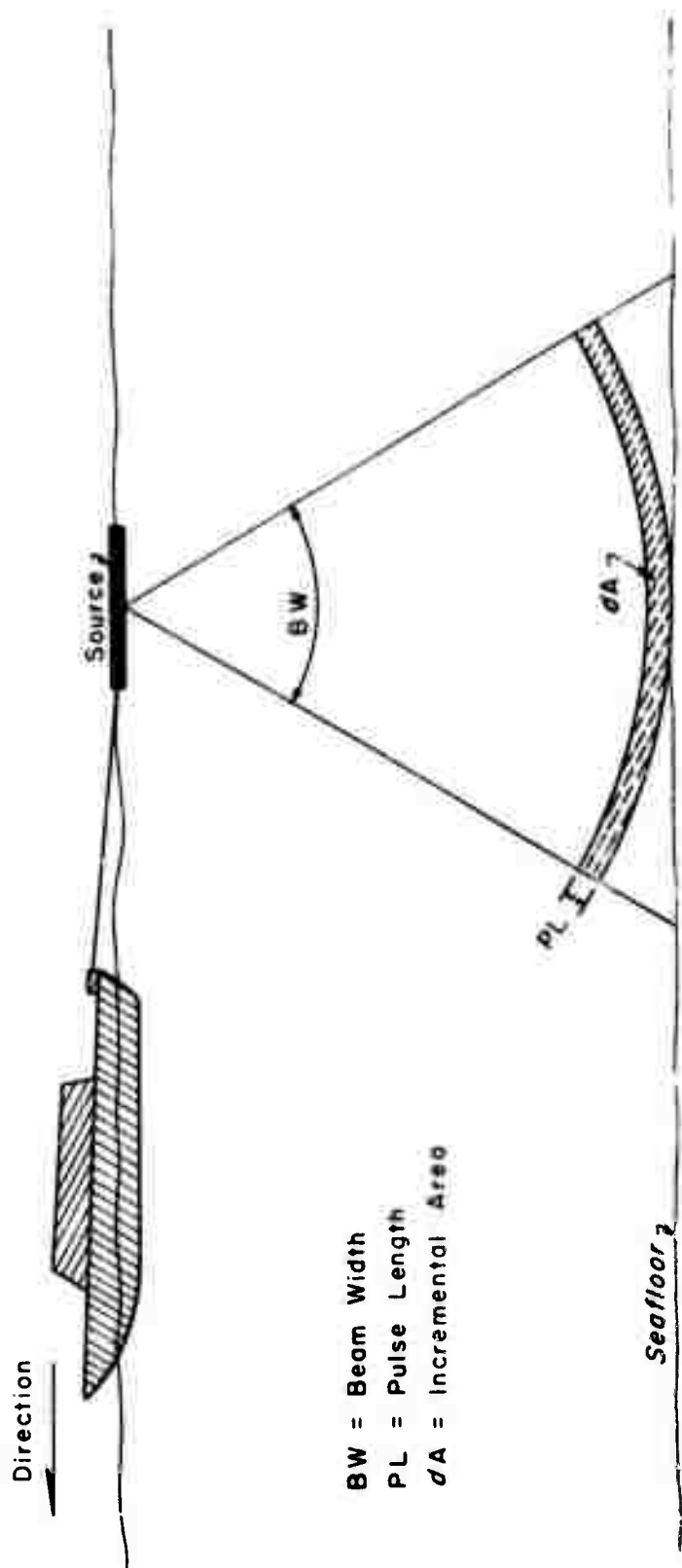


Figure 3-20. Transmitted sound pulse.

Rayleigh Reflection Coefficient, R.

$$\text{i.e. } K = R^2 \quad (\text{Eq. 13})$$

where K is defined on a peak pressure basis, thusly

$$K = \frac{P_R^2}{P_S^2} (2D)^2 \frac{1}{e^{-\alpha 2D}} \quad (\text{Eq. 8})$$

where

P_R = pressure of the echo pulse

P_S = pressure of the source pulse

D = transmission loss due to spherical spreading

$e^{-\alpha 2D}$ = transmission loss due to dissipative attenuation of sound in seawater

Expressing Eq. 15 as a logarithmic function to get decibel form gives an expression of the fundamental equation for bottom loss, BL

$$\text{i.e. } BL = S_{PL} - E_{PL} - TL_S - TL_A \quad (\text{Eq. 15})$$

where

BL = bottom loss (in dB) and is equal to $-10 \log K$

S_{PL} = pressure level of the source pulse (in dB//1 dyne/cm²) and is equal to $20 \log P_S$

E_{PL} = pressure level of the echo pulse (in dB//1 dyne/cm²) and is equal to $20 \log P_R$

TL_S = spreading loss (in dB) and is equal to $20 \log 2D$

TL_A = attenuation loss (in dB) and is equal to $10 \cdot 2D \log e$

A final expression relates to bottom loss, BL, to reflectivity, R.

$$BL = 20 \log R \quad (\text{Eq. 17})$$

Other manifestations of these basic expressions that include measurements dealing with the energy versus time waveform of the echo are described in Breslau's paper (1968). Since this investigation was concerned only with peak pressure measurements, the derivations relating

to energy in the echo strength are not included in the appendix.

Relation of Bottom Loss to Mass Physical Properties.

The mass characteristics of the bottom sediment are related to bottom loss through the Rayleigh Reflection Coefficient and the acoustic impedance contrast (Eq. 12) at the interface, and it has been shown by Eq. 17 how the Rayleigh Reflection Coefficient is related to bottom loss. It is possible to establish a relationship between porosity and bottom loss through the expression for impedance (Z) which is dependent upon density and compressional velocity, both factors that relate to the porosity of natural sediments.

In summary, several investigations have ascertained a linear relationship exists between porosity and density, in particular that bottom loss as deduced from many measurements made on sediments bears a definite relationship to the porosity of the sediment. And furthermore, since the porosities of natural sediments are somewhat related to sediment grain size, it is also possible to establish a general relationship between bottom loss and the geological properties of sediments.

For further discussion of the sediment bulk properties and variations within the physical makeup of the grains, interstitial properties, etc. and more specifics on how these factors influence porosity, the reader is directed to the papers by Nafe and Drake (1963), Birch et al (1942), Hamilton et al (1956), Shumway (1960), Sutton et al (1957) and Breslau (1964). The information available on this subject is too voluminous to be discussed here.

3.2.5 Description of Geophysical Instrumentation and Equipment

The instrumentation used for acquisition and processing the data is discussed independently according to its location and function. The recording and sound source equipment is all shipborne, the reproducing and processing equipment is located in a shore-based central processing facility. The block diagrams given in figures 3-21 and 3-22 illustrate the data flow. Elements in the data flow are indexed by circled letters for purposes of discussing the components and their respective signal processing function.

Acoustic Sources (Shipborne).

The acoustic-reflectivity measurements incorporated two acoustic impulse sources, an electrical type discharge generated by a multiple-electrode sparker sound source (figure 3-23) and a standard fathometer transducer. The directional multiple-electrode sound source (DMSS), developed by MMTC, is powered by a capacitor bank capable of delivering a maximum output of 1000 joules. For this experiment, 500 joules was the operating power, measured at the capacitor. Effective power delivered at the source varies; however, tests indicate at least a 60% power loss occurs due to transmission loss. This is a factor normally overlooked in rating power delivered in spark discharge seismic systems. A more meaningful value is the acoustic output determined by calibration using a standard. The measured average acoustic power output of the source is 101.5 dB/V/ubar referenced to 1 yard.

The DMSS source is a prototype test tool that produces a broad band frequency spectrum which ranges from 0 to 5 KHz. Center frequency

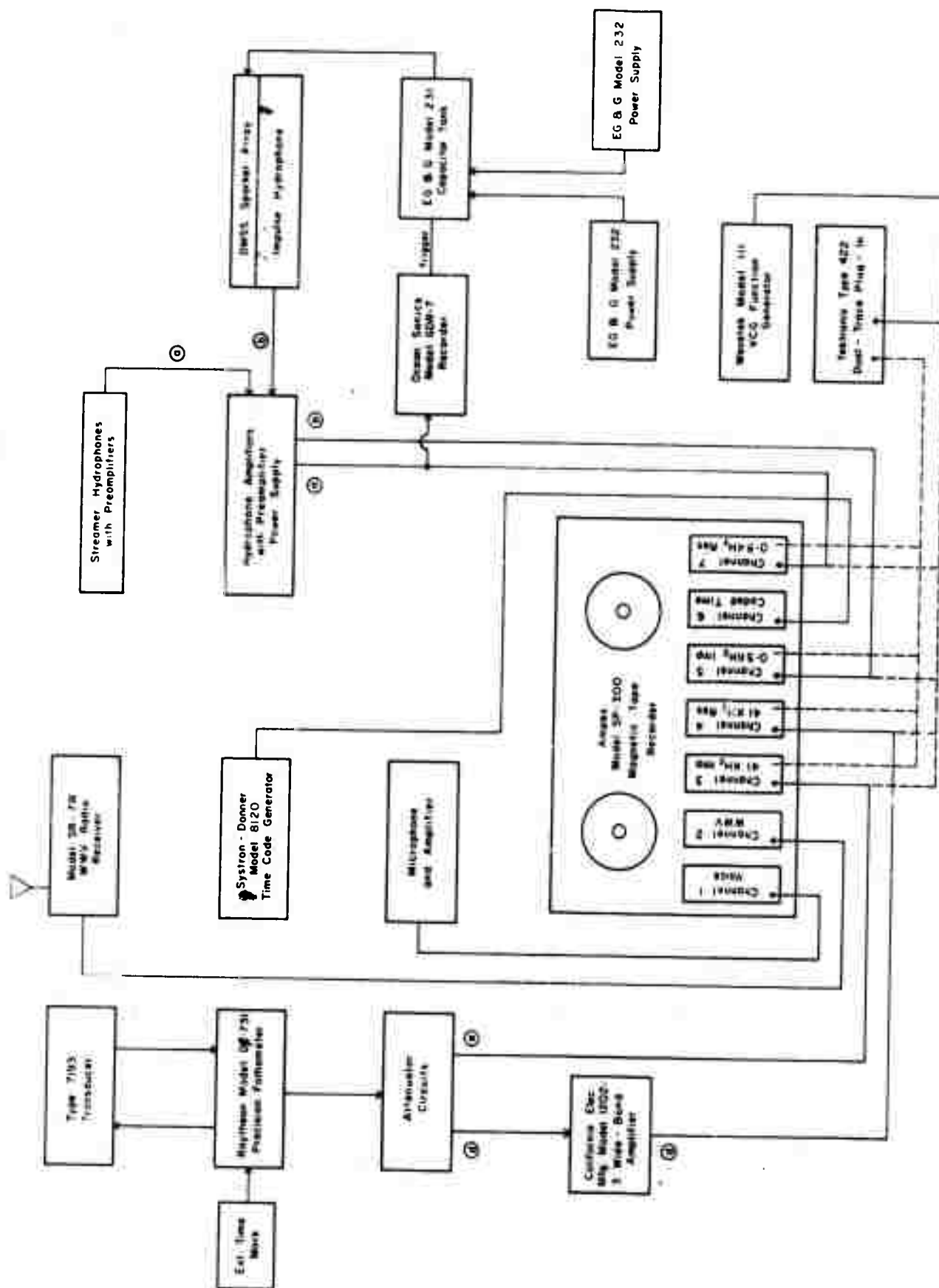


Figure 3-21. Shipboard recording and sound source equipment.

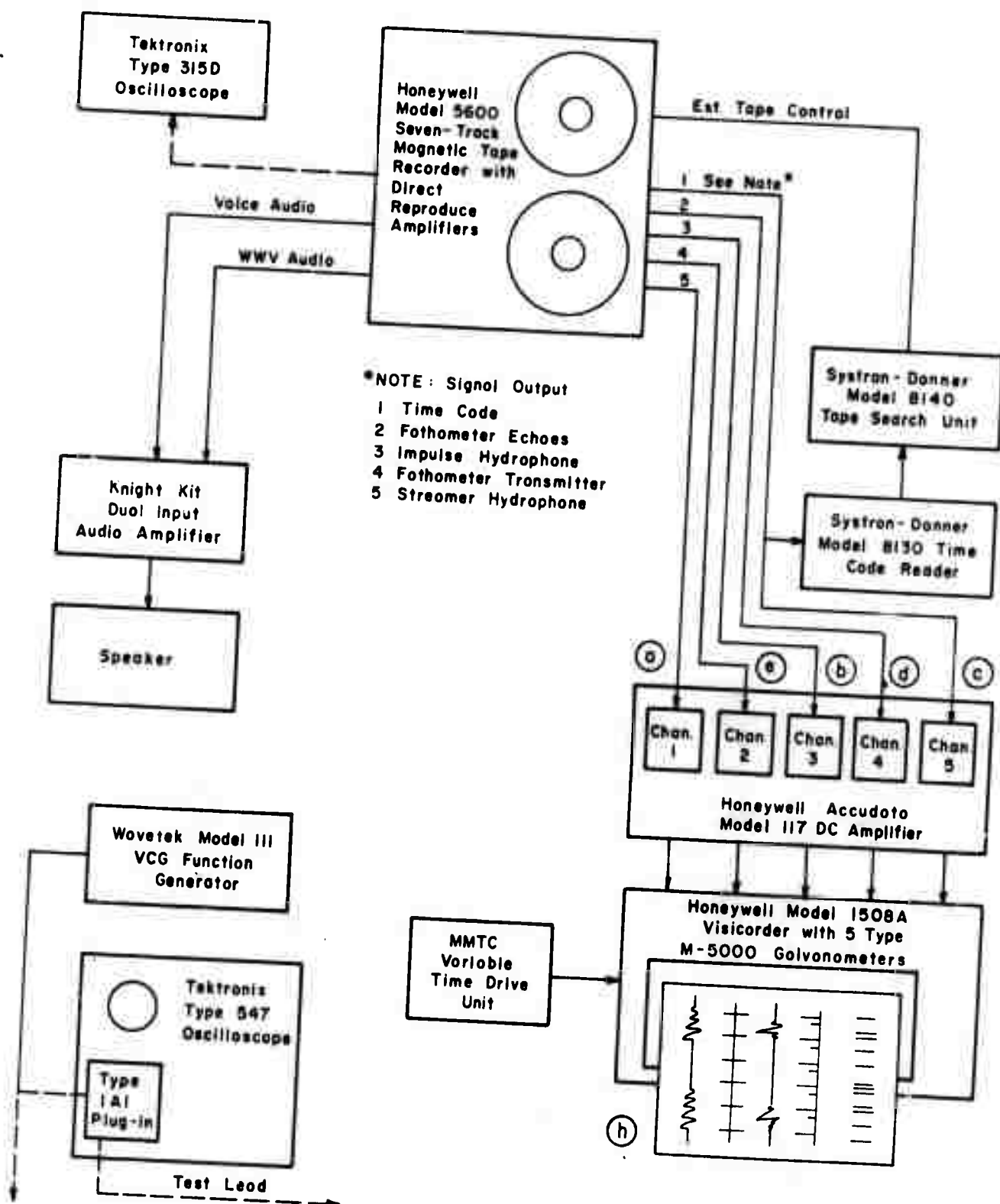
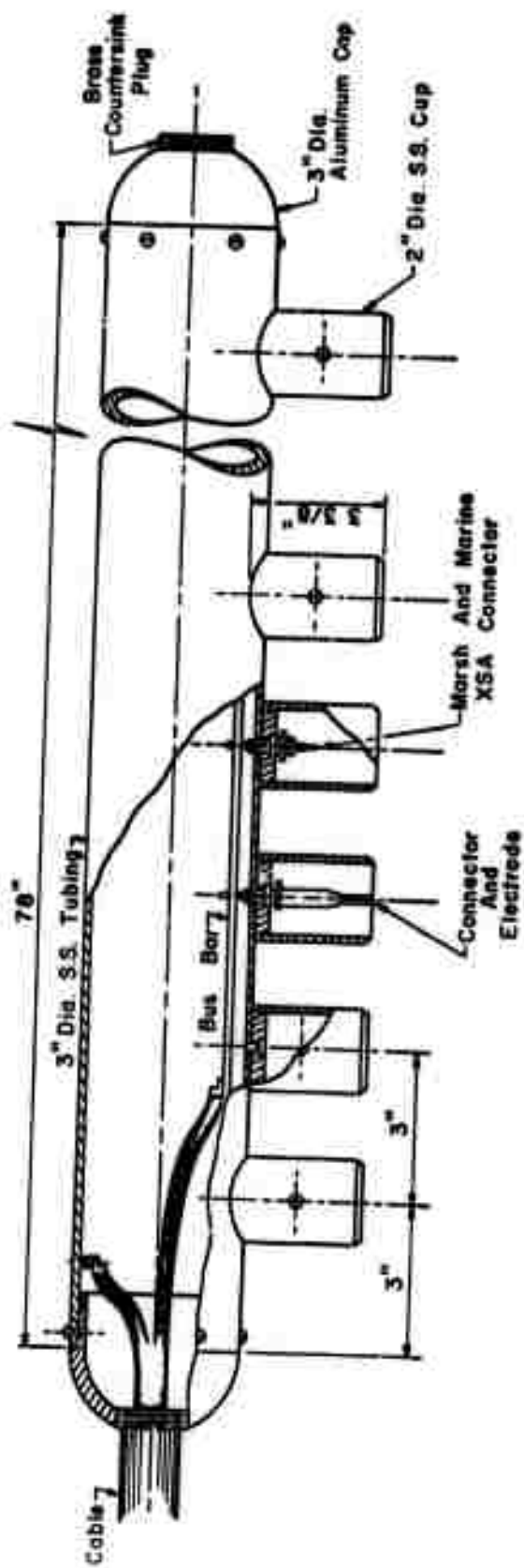


Figure 3-22. Shore station rock mounted reproducing equipment.



Not to Scale



Figure 3-23. Directional multiple electrode sound source (DMSS).

is about 2.5 KHz. The short pulse length and wide beam enable a specular energy distribution yet retain a relatively high resolution for shallow (water operation) penetration. Directionality of this source has been tested giving about 3 to 5 dB improvement in the vertical (downward projection) plane when the cylinders are in the downward orientation. The multiple electrode arrangement produces what is essentially a line source. Bubble collapse which is known to generate undesirable secondary impulses is minimal. This was the primary reason the DMSS unit was selected over single and triple electrode sources.

In conjunction with the DMSS unit, a Raytheon Model DE-731 Precision Fathometer and Depth Recorder (figure 3-24) was used. The 41.5 KHz discrete frequency source is a hull-mounted barium titanate piezoelectric type transducer. It has a narrow beam angle of 16° at -3dB on the frontal plane and a 43° beam in the athwart ships plane. The transmitted pulse is rated at 600 watts into a 150 ohm load. In terms of acoustic power delivered this is 113 dB/V/ubar at 1 yard.

Impulse-Response Receivers (Shipborne).

The sparker impulse (transmitted peak pressure) hydrophone receiver array (figure 3-25) consists of nine hydrophones connected in parallel whose output is fed directly to a shipboard single channel amplifier. The array is mounted piggyback to the acoustic source unit during the operations, thus representing as near a direct coupling to the source as possible (figure 3-26). Throughout the survey, the amplifier gain of the piggyback hydrophone array is set at near unity to eliminate overloading and signal distortion that could affect the amplitude measurement.



Figure 3-24. Raytheon model DE-731 precision depth recorder.



Figure 3-25. Impulse hydrophone and no. 1 main hydrophone receiver arrays.

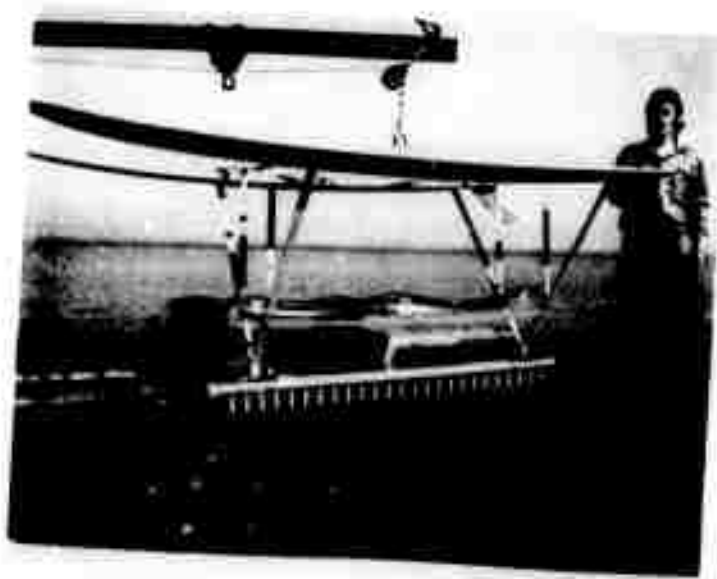


Figure 3-26. DMSS unit and impulse hydrophone receiver - tow configuration.

The sparker source with the piggybank hydrophone is towed alongside a main hydrophone streamer at a distance of about 75 feet astern of the ship. The main hydrophone streamer receives the reflected response from the bottom and subbottom seismic horizons. The maximum side-by-side distance employed throughout the survey was about 10 feet, thereby affording the reception of essentially a normally incident signal.

The average effective dynamic range (in field operation) of the impulse hydrophone is 80 dB. The low end sensitivity is limited by random electronic noise. The basic receiving sensitivity is -92.4 dB/V/ubar , and the maximum amplifier gain is 42 dB.

The signals from the sparker impulse hydrophone and the main hydrophone streamer are fed independently through the shipboard amplifier and then onto separate tracks of a 7 channel analog magnetic tape recorder (figure 3-27). Shipboard amplification of the impulse receiver is kept near unity. The main hydrophone streamer amplification varies according to the gain needed to boost the signal above the noise threshold. Conditions that can cause changes in the gain are; 1) large variation in water depth, 2) externally generated noise, or 3) marginal reflectivity due to high energy loss in soft, unconsolidated sediments. Annotation of the variations in gain settings to the amplifiers is recorded as changes are made. The data is then normalized in processing.

In some instances the signal generated by the number 1 main hydrophone streamer is inverted. This is due to processing the signal through a 100 Hz high-pass filter. The graphical reproduction of the analog of the wave train on the visicorder display will therefore reflect this inversion. Whether it is inverted or not is dependent upon

*Figure 3-27. 7-channel
analog tape recorder
(Ampex model SP-300)
and receiver-amplifier.*

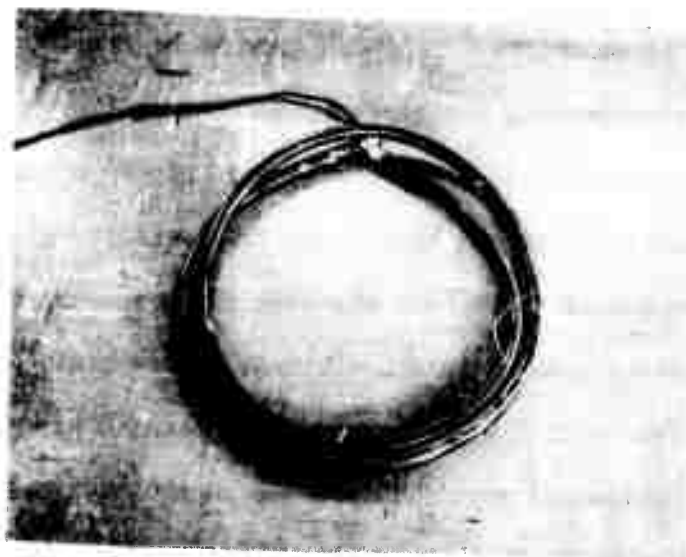


Figure 3-28. No. 2 main hydrophone array.

filtering. The number 2 main hydrophone streamer signal is always inverted.

Two main hydrophone streamers were alternated throughout the survey. One streamer, designated as No. 1, (figure 3-25) consisted of 20 hydrophone elements divided into 8 electrical sections or groups of either 2 or 3 elements. Within each group, the phones are wired in parallel. The groups are wired in series. The signals from the elements are amplified by preamplifier modules in the streamer. The number of groups activated vary according to the operator's selection. Variation is controlled at the shipboard amplifier unit. The signals from all 8 groups or fewer can be composited and amplified at the shipboard control unit. The average effective dynamic range of the number 1 hydrophone is 29.2 dB. The low end sensitivity is limited by the towing noise observed on the records. The nominal operating dynamic range is 46 dB where the low end sensitivity is limited only by ambient noise generated by the electronics and vibrations. The basic receiving sensitivity is -75.5 dB/V/ubar. The maximum amplifier gain is 52.3 dB with the 100 Hz filter on.

A depth transducer is contained in the number 1 streamer and information regarding steamer towing depth is read out on a calibrated meter on the front panel of the shipboard amplifier unit.

The number 2 main hydrophone streamer (figure 3-28) consists of 18 hydrophone elements divided into 3 electrical groups of 6 elements, each wired in parallel, with the groups wired in series. Preamplification of the signal and shipboard amplification and capability for group variation is the same as used on the number 1 streamer. The average effective dynamic range (in field operation) of this hydrophone is 32 dB.

The low end sensitivity is limited in this case by towing noise observed on the records. The nominal dynamic range is 47 dB. The low end sensitivity in this case is limited only by ambient electronic and vibration noise. The basic receiving sensitivity is -76 dB/V/ubar and the maximum amplifier gain is 46 dB. The number 2 streamer does not have a depth transducer.

The receiver hydrophone for the 41.5 KHz fathometer transducer has a dynamic operating range of 60 dB. This value was not measured, but was obtained from the Raytheon Model DE-731 Fathometer Depth Recorder Operation and Maintenance Manual.

Signal Processing (Shipborne).

The transmitted impulses and return echoes are monitored at the transducer input. The signals are next fed to attenuator circuits to reduce the transmitted impulses to an acceptable recording level. The transmitted signal was attenuated by 43.2 dB and then fed directly to the magnetic tape recorder. The return echoes are attenuated by only 2.7 dB, while the accompanying transmitted signal was clipped by diodes. The low amplitude echoes are then amplified and these signals fed to the magnetic tape recorder. The transmitted fathometer impulse amplifier is an R-C coupled wide band, solid state amplifier with a 40 dB maximum gain and a frequency response of 20 Hz to 500 KHz. The amplifier features low harmonic distortion, flat frequency response, and high stability due to the fact that its variable gain is determined by a ratio resistor that varies the amount of negative feedback rather than a nonlinear transistor. All specifications for the Wide Band Amplifier (Model 1202-3) were taken from the Technical Manual of the manufacturer, California Electronic

Manufacturing Co.

The Ampex Model SP-300 rack mounted magnetic tape recorder is a seven track recorder using 1/2 inch, 1.0 mill tape on type NAB 10-1/2 inch reels. It is operated at a tape speed of 15 ips, accurate to a rated $\pm 0.2\%$ and with flutter specification of less than 0.15%. The head assemblies are IRTG compatible. The seven individual plug-in amplifiers enable direct or FM record or reproduce capability. The direct record mode of operation is used in this application.

The input signal range required for a normal level of recording is specified at 0.5 to 10.0 volts rms with total harmonic distortion rating of less than 0.5% tested at 1 KHz and 15 ips. The input impedance is greater than 10 K ohms. The record amplifier can produce an output to the head at least 8 dB above the normal level before saturation of the amplifier occurs. The rated signal to noise ratio is 30 dB. At 15 ips, the rated frequency response is within ± 3 dB from 50 Hz to 40 KHz.^{6/}

During field operations, selected calibration signal levels are recorded on each tape. At the shore based playback center, these pre-recorded calibration signals are used to determine any signal level errors of both tape recorders and the visicorder. The errors are then added to the computed signal levels.

The inputs to the seven channels are as follows (figure 3-21):

Channel 1: Voice

^{6/} Specifications quoted were obtained from SP-300, FM/Direct Recorder/Reproducer Operations and Maintenance Manual, Ampex Part. No. 48814-30.

- Channel 2: WWV audio
- Channel 3: Fathometer transmitted impulse signals (figure 3-29e)
- Channel 4: Fathometer echos (reflected signals) (figure 3-29d)
- Channel 5: Sparker impulse signals from the piggyback hydrophone (figure 3-29b)
- Channel 6: Time code, IRIG standard format B (figure 3-29c)
- Channel 7: Main streamer hydrophone (reflected signals) (figure 3-29a)

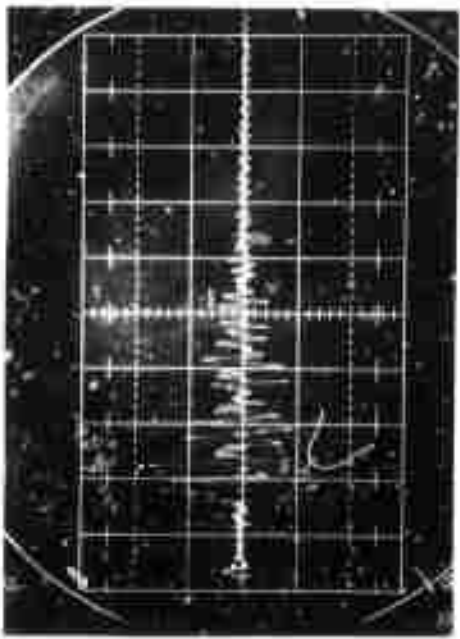
The time reference is obtained from the Systron-Donner Model 8120 Time Code Generator. The unit is used to generate an Inter Range Instrumentation Group B (IRIG B) time code format in terms of Binary Coded Decimal (BCD) hours, minutes, and seconds. As a Time Code Generator, it also has a precise digital clock, which produces a serial code for recording continuous time on the magnetic tapes. On the front panel of the instrument, updated time is displayed by an in-line nixie-tube read-out unit.

The time base is a crystal controlled oscillator with an overall stability of 1 part in 10^5 per day. The modulated code is generated on a 1 KHz carrier with an adjustable amplitude from 0 to 10 volts (peak to peak) and an adjustable modulation ratio.^{7/} This output was connected directly to the Ampex tape recorder.

Signal Processing (Shore Based).

The recorded tapes are processed at a shore based playback center (figure 3-30). The tapes are first played back at 15 ips (recording

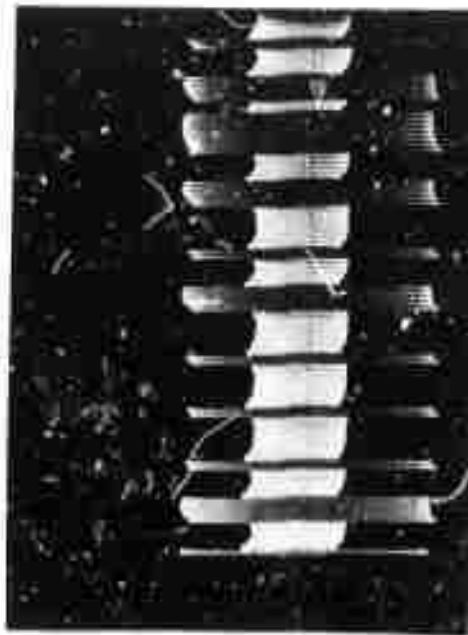
^{7/} Information from Systron-Donner Time Code Generator Model 8120 Manual.



a. 0-5 KHz Response



b. 0-5 KHz Impulse

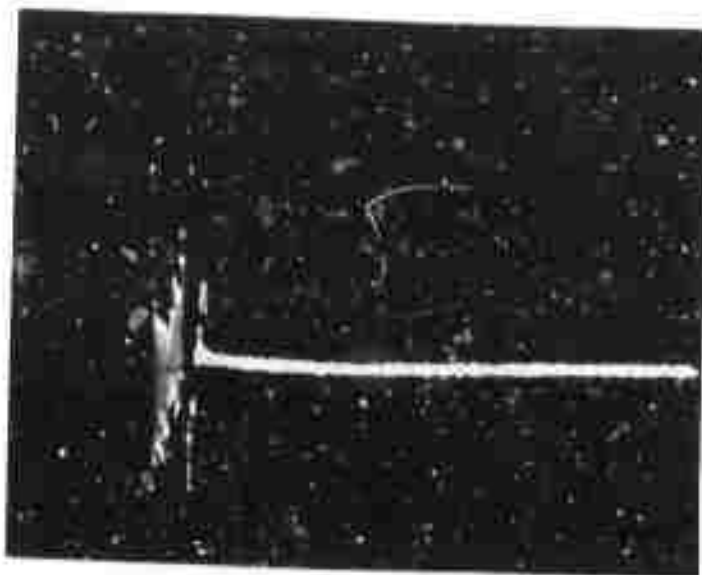


c. IRIG B Time Code

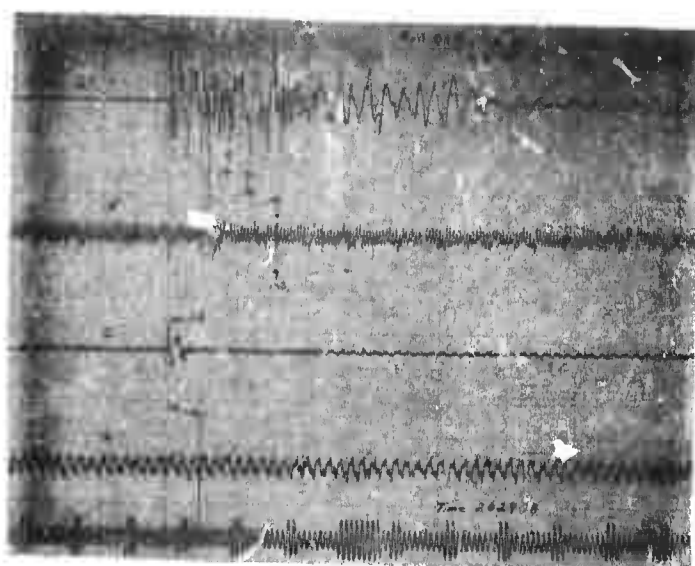


d. 41 KHz Response

Figure 3-29. Signal wave forms.



e. 41 KHz Impulse



Trace 1

Trace 2

Trace 3

Trace 4

Trace 5

f. Visicorder Record

Trace 1 - 0-5 KHz Wave Train (Impulse-Response)
 Trace 2 - 41 KHz Impulse
 Trace 3 - 0-5 KHz Impulse
 Trace 4 - 41 KHz Response
 Trace 5 - IRIG B Time Code

Figure 3-29. Signal wave forms.

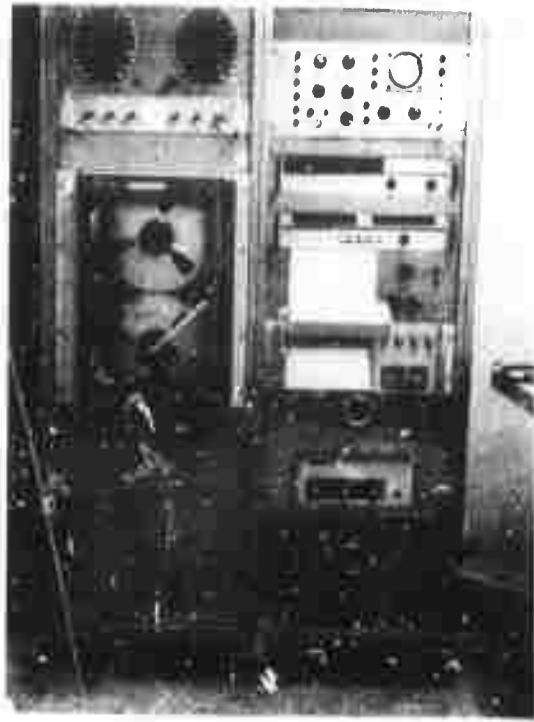


Figure 3-30. Shore-base playback console.

speed) to listen to the audio channel and note the gain setting changes or pertinent information which might affect the computation of the signal levels.

The Honeywell Model 5600 rack mounted magnetic tape system is a 7 track machine capable of reproducing data at seven selectable, servo-controlled tape speeds from 15/16 ips through 60 ips. The machine has IRIG compatible 1/2 inch tape heads with an optional voice channel on an edge track. Flutter, skew, and time displacement error are minimized by the servo-controlled tri-capstan drive and independent reel servos. At 15 ips, flutter is rated at 0.4% P-P and at 1-7/8 ips 0.7% P-P. Tape speed accuracy is rated at 0.15% of the selected speed.

The machine is fitted with 7 direct reproduce plug-in amplifiers and one direct plug-in amplifier. The record/reproduce amplifier's rated frequency response at 15 ips is 100 Hz to 75 KHz with a 30 dB RMS signal to RMS noise ratio; at 1-7/8 ips, 50 Hz to 9300 Hz it is rated at 26 dB signal to noise ratio. The input signal range required for a normal level of recording is specified at 0.3v RMS to 3.0v RMS with Harmonic Distortion rated at 1%, tested at 1 KHz and 60 ips. The input impedance is greater than 100 K ohms. Each reproduce amplifier has two equalization plug-in cards, with the correct one being selected by the speed control switch.

During the playback operation the 15 ips and 1-7/8 ips speeds are used. At 15 ips, the audio comments concerning amplifier gains, maneuvering, calibration and general observations and comments are monitored along with a time check of WWV compared to the pre-recorded time code.

The speed is reduced to 1-7/8 ips to give an 8 to 1 reduction of recorded frequencies to enable better reproduction and data acquisition by the Visicorder. The machine is operated manually and is remotely controlled by the Tape Search Unit.

The Systron-Donner Model 8130 Time Code Reader is used to translate the recorded IRIG B time code (BCD format) in terms of hours, minutes and seconds. The incoming time code is visually presented on a six digit in-line nixie tube readout on the front panel. The rack mounted unit decodes the incoming time code in both forward and reverse directions during the data playback and is used in combination with the Model 8140 Tape Search Unit, thus providing a fully automatic tape search system, with manual override 8/

The Systron-Donner Model 8140 Tape Search Unit (TSU) is a combination tape search and transport control unit used with the Model 8130 Time Code Reader. The TSU provides the remote control commands for the Honeywell Model 5600 Magnetic Tape System in order to automatically search for, locate and produce selected segments of test data.

The Model 8140 operates as a digital limit comparator to compare the decoded tape time from the Model 8130 with selected start and stop times that are pre-set by the operator by means of thumbwheel switches. Upon detection of the desired time comparisons, the search unit automatically provides the various control commands (contact closures) to the tape transport. Manual search is also included in the control.

8/Information from Systron-Donner Data Products Division Manual for the Model 8130 Time Code Reader for IRIG B.

In a typical operation the operator sets in predetermined times which are correlated with a determined location relating to a particular sample site in the survey, i.e., the coring sites. The tape automatically searches out the start time and reads out data to the end of the pre-selected time window at designated speeds. In order to accomplish this feature a Variable Time Drive Unit had to be designed and built. The MMTC modification to incorporate the Variable Time Drive Unit (VTDU) is used to control the operation of the visicorder paper drive motor. Both the repetition rate and the duty cycle times can be varied by the operator. This unit was used to reduce the amount of photographic paper used, thus reducing the cost of playback.

Typical sparker firing rates are .75 second and 1 second. The visicorder paper speed is 10 inches per second. However, there is an 8 to 1 reduction of tape speed, from 15 inches per second to 1-7/8 ips, which lengthens the firing rates to 6 and 8 seconds respectively. Paper consumption for a 10 second observation of 10 bursts amounts to 600 to 800 inches per site.

Since most of the significant information could be obtained in an interval of .25 second to .4 second the VTDU reduced paper consumption to a minimum of 200 inches and to a maximum of 400 inches per site.

The Honeywell Accudata 117-06 is a rack mounted 6 channel direct coupled amplifier unit consisting of six separate solid state, wide band, single ended, low gain amplifiers. This instrument is used to drive the galvanometers of the Model 1508A Visicorder.

The amplifiers amplify AC and DC voltages and provide the proper

impedance matching and isolation between the tape recorder reproduce amplifier outputs and the visicorder. Each channel has a multi-position gain switch in steps of 1, 2, 5 from .01 to 10 yielding a 1000:1 range, and a vernier control that increases the fixed gain from unity by a factor of 2.5. The maximum rated input is ± 300 VDC or peak AC. The maximum rated output is ± 3 VDC or peak AC at 40 milliamperes.

The accuracy at DC is $\pm 2\%$ and the gain or sensitivity linearity is $\pm 0.2\%$ of full scale output at DC. The frequency response is flat within $\pm 5\%$ from DC to 20 KHz. The overload recovery time is less than 100 microseconds to within $\pm 1\%$ of the final value with an overload 10 times the full scale input up to a maximum of 300 volts. The DC stability is rated at less than 100 microvolt/degree Centigrade. The noise level is less than ± 2 millivolts RMS over DC to 20 KHz for all gains.

The Honeywell Model 1508A Visicorder (Visual Recorder) is a direct-writing oscillograph recorder with provisions for up to 12 channels of input. A photographic, permanent recording of the tape recorded analog data is produced (figure 3-29f). A mercury vapor, ultraviolet light source produces the nominal 0.2 inch wide traces on the 8 inch wide sensitized paper which is relatively insensitive to normal room lighting.

The recorder includes a high-linearity optical system consisting of 5 fluid damped miniature galvanometers, an accurate grid line system and timing line system. The recorder drive system can be operated at speeds ranging from 0.1 to 80 inches per second. Four reference timing line intervals of .01 to 10 seconds, with a basic $\pm 1.5\%$ accuracy, can be selected on the recordings. The simultaneous recording of the grid lines

and galvanometer traces at the same point on the paper eliminates any inaccuracies due to dimensional changes in the paper caused by humidity or lateral paper movement during the recording process.

Five, fluid damped, miniature, type M-5000 galvanometers are used. Their normal undamped natural frequency is 5000 Hz, with a rated flat, $\pm 5\%$, frequency response of 0 to 3000 Hz. The mirrors are optically coated to insure maximum efficiency of the reflecting surface. The maximum deflection of the AC operation is rated at 3.5 inches which maintains the proper optical qualities and a $\pm 2\%$ linearity specification. Each magnet assembly is heated and thermostatically controlled at 120° F. This temperature control insured top performance and stability of the fluid-damped galvanometers by maintaining a constant viscosity of the damping fluid.

A typical paper drive speed of 10 inches per second is used with a timing grid of 0.1 seconds. Kodak type 1895 Linagraph paper is used. The relative writing speed of the paper is rated at up to 100,000 inches per second.

Exact calibration of the recorded and reproduced information signals is accomplished by recording calibration levels of 1 KHz sine wave signals on each of the active information channels during the actual shipboard operation. The calibration levels are then played back on the shore based equipment and any discrepancy is measured, noted and included in all the readings measured and computed from the visicorder photographic record. Therefore, the total error of both the recording and playback systems is reflected in this one measured value for each information channel.

The equipment used to record and measure the calibration levels is a Wavetek Model 111 Voltage Controlled Generator and a Tektronix type 422 oscilloscope.

The various incoming information signals and calibration signals are monitored with the Tektronix type 422 dual channel oscilloscope. The vertical deflection accuracy is within the rated 3% of the indicated deflection factor. The range of vertical deflection is from 10 millivolts per division to 20 volts per division, in 11 calibrated steps. The frequency response of both channels is flat from the rated DC to 15 MHz at the -3 dB point. Single, dual trace alternate, or chopped modes of presentation are depicted for later analysis.

Seismic Data Processing.

All the seismic data processing is accomplished at the Tiburon Center. Visicorder reproductions are analyzed by measuring the peak amplitudes of the transmitted and received pulses. These measurements are accomplished by hand and computed directly without the aid of digital computers.

The location of each of the 16 core sites are correlated for position to the seismic data by the time reference marks on the x-y plots and the listing from the digital printer. The times obtained thusly are set by the operator on the tape search unit. When the selected time on the tape is read and monitored, the recorder is then set to 1-7/8 ips and the playback amplifier adjusted to provide the proper recording levels. The tape playback is automatically or manually cycled and by use of the variable time drive unit the visicorder drive is controlled to provide a visual record of the taped signals (figure 3-29f). Each tape is then run to

the recorded calibration sections where any signal level variations from the known calibration levels can be noted and incorporated in the computation of the measured signal levels (peak amplitude of the desired event on the impulse-response wave train). The visicorder gain levels are noted on the record (figure 3-29f) and the signal levels of the desired events are measured. The measurement is converted to the corresponding voltage level for computation.

The steamer hydrophone events are identified in several ways. Generally the water depth (in time) is sufficient, or when readily identified the character of the impulse hydrophone signal. Another method involves checking the seismic record and timing the multiples of the primary reflector (sea floor horizon). One can usually distinguish the real signal of the surface reflector horizon from other reflecting sources or induced noise sources by establishing the time differential between successive multiple reflections and regressing to the primary reflector event.

The playback wave forms fed from the tape recorder to the Honeywell AC to DC amplifier are illustrated in figures 3-22 and 3-29. The typical playback signal amplitudes are: steamer receiving hydrophone signals 3 to 4vp-p (figure 3-29a); the piggyback impulse signals 1.2vp-p (figure 3-29b); the fathometer receiver signals 0 to 2vp-p (figure 3-29d); and the fathometer transmitter signals 1.5vp-p (figure 3-29e).

High Frequency Impulse Signal.

Trouble was encountered with both the amplifying and recording of the fathometer received echo signals. The beam width of the fathometer transducer is apparently too narrow, the fathometer is designed to

operate at depths up to 2460 feet, to obtain an absolute amplitude measurement of the signal. The primary problem encountered was maintaining a consistent return amplitude at any one location. Even when the boat was moored at one fixed location to test the consistency, repeatable amplitudes were never reliable. For this reason, data used in the investigation is limited to the broad band (0-5 KHz) sparker source (section 3.2.9).

3.2.6 Sediment Sampling Equipment

In order to verify reflectivity measurements it was necessary to have a core sampler which could rapidly sample the first meter of surface sediments and obtain relatively undisturbed samples. This was required for reliable engineering and mass physical property determinations. A one meter core length was decided upon because the depth of penetration was also within the wave length of either of the two acoustic sources employed. This makes it possible to determine to what degree changes in the near surface lithology or structural variations influence the reflection coefficient. Three samplers of the gravity-type or piston-type gravity corer variety were tested but found unsatisfactory. It was therefore necessary to design, construct and test a coring device that would provide the desired capability. It was also decided that the energy source for penetration should not be percussion or rotary since these types tend to induce sediment distortion. Therefore, a steady thrust energy produced by pneumatic power was incorporated in the design.

Diver Operated Corer - Design.

Simplicity of operation and a minimal number of mechanical-electrical features were other criteria used for design of the corer. A study

of figures 3-31 through 3-34 gives self-explanatory details of the design and hardware incorporated in the final product. Details covering the laboratory and field test of the prototype tool are in a report by Jenkins and Takeyama (1971). The field testing and evaluation of the prototype corer were done in conjunction with the sampling program for the reflectivity experiment.

Operation.

All work associated with the coring program is done from the DOODLEBUG, a 40-foot converted launch (sect. 3.2.7). A crane and winch, having a load capacity of 1,000 pounds, were used to handle the corer. Scuba divers are used during the actual sampling. Three divers are normally required; two operate the device under water and the third remains on the surface as standby and relief. Valves, located on the corer, are actuated by the divers. These can be regulated by the diver to enable a flow of air pressure to drive a piston that forces the Shelby sampling tube slowly into the sea floor. The force of the steady thrust is controlled by regulating the pressure. When full penetration is observed a three-way valve is reversed and three independent hydraulic pistons lift the main carriage away from the base plate, thus retrieving the core barrel from the sediment. A diver immediately caps the lower end of the barrel to preclude core loss. The core unit is completely sealed while under water so that water content remains as it was in situ. The removal of the core barrel and replacement of a second core barrel is done by the divers under water. This saves time and makes preparation for the next sampling operation more efficient, particularly when a vessel has a very small deck area.

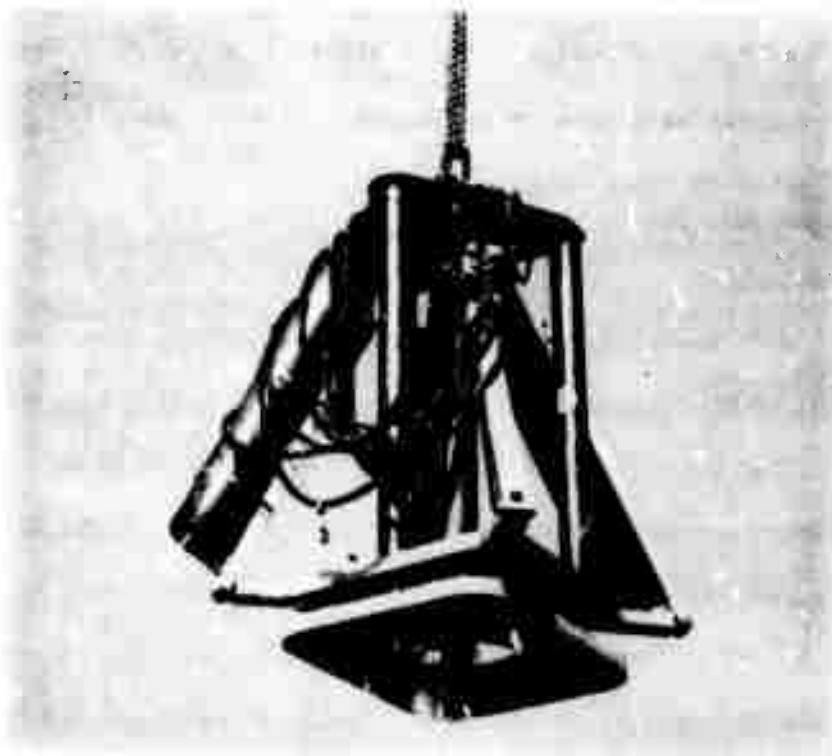


Figure 3-31. Diver operated corer (retracted position).

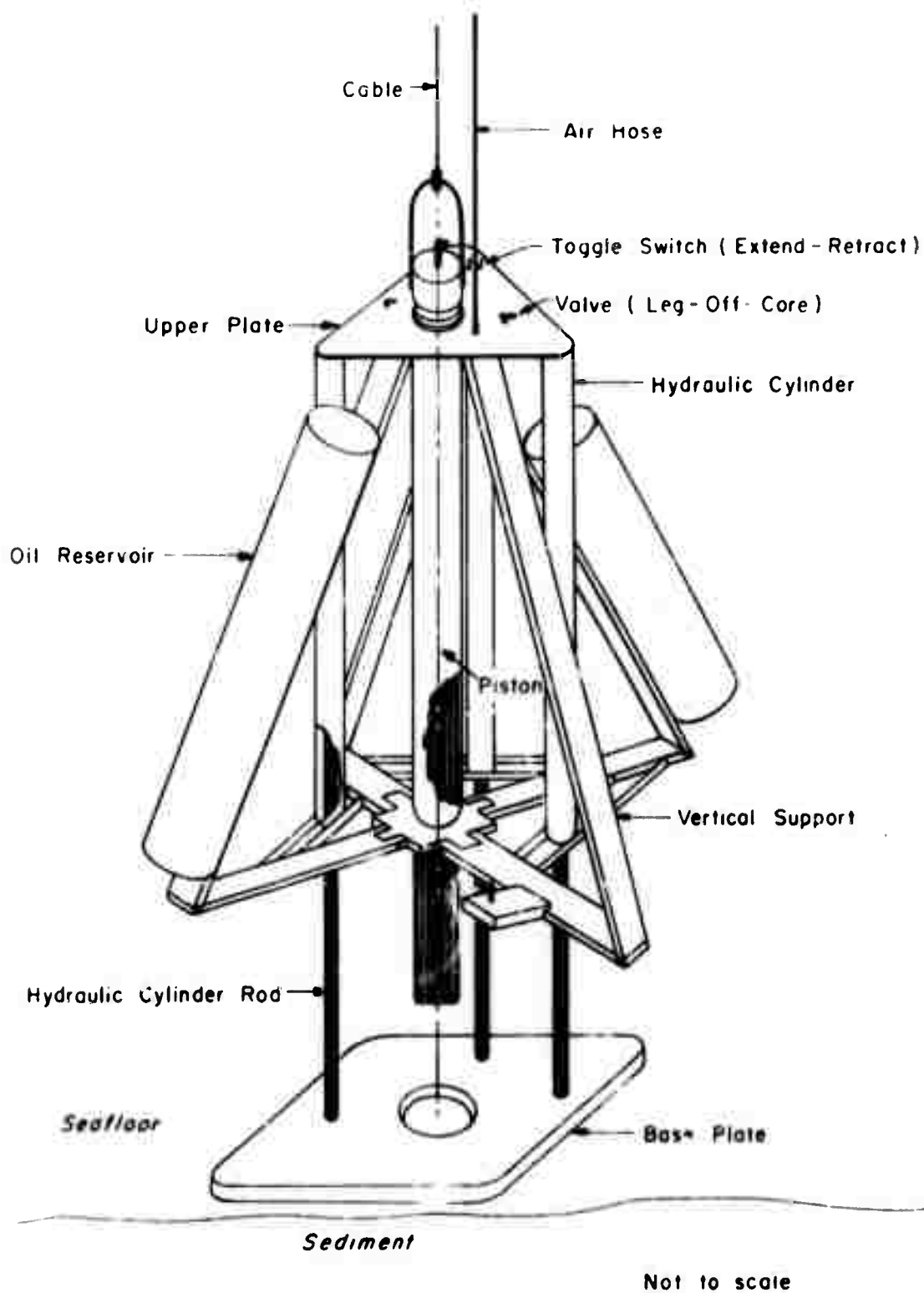


Figure 3-32. Diver operated corer (extended position).

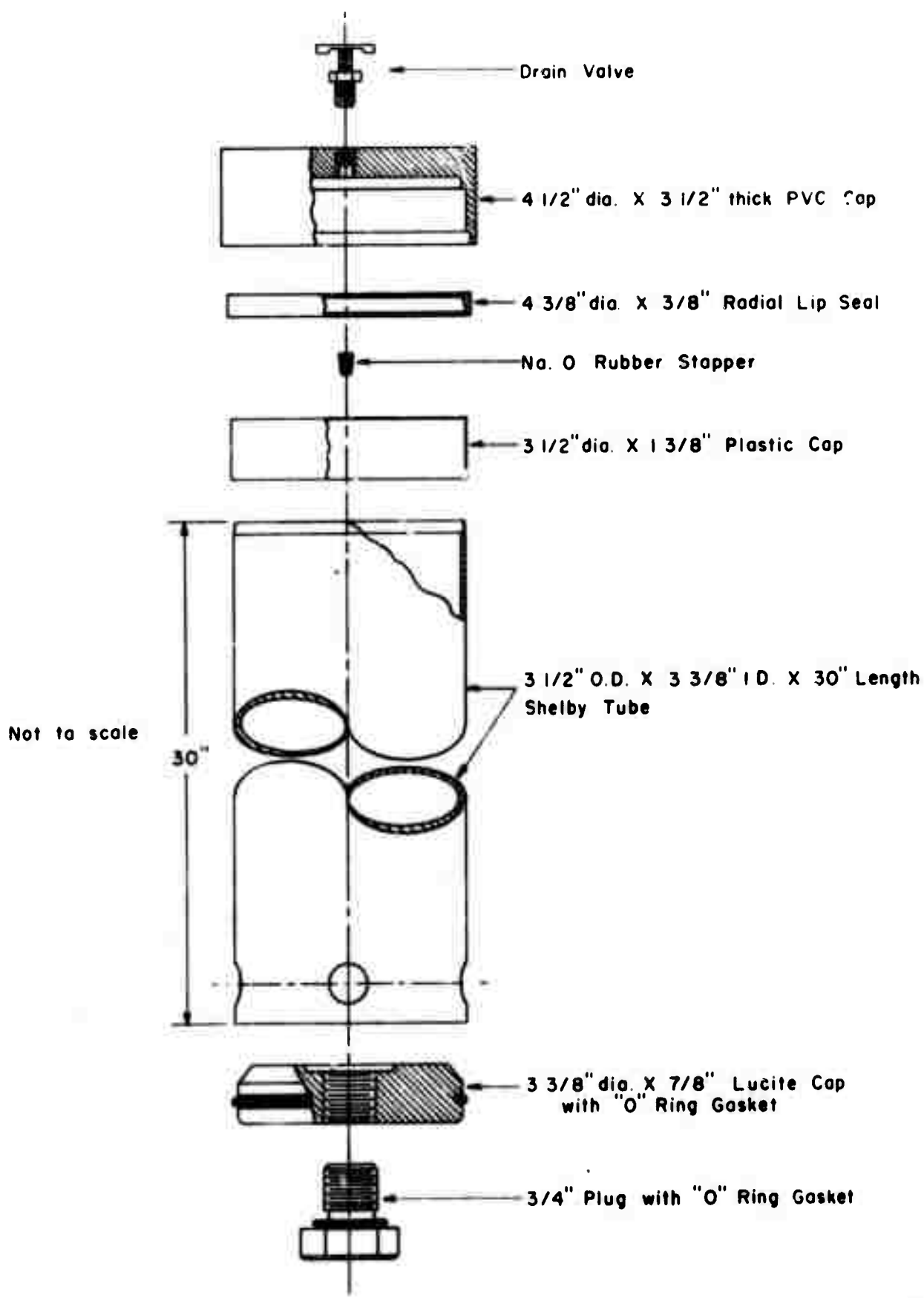


Figure 3-33. Core retainer modified Shelby tube.

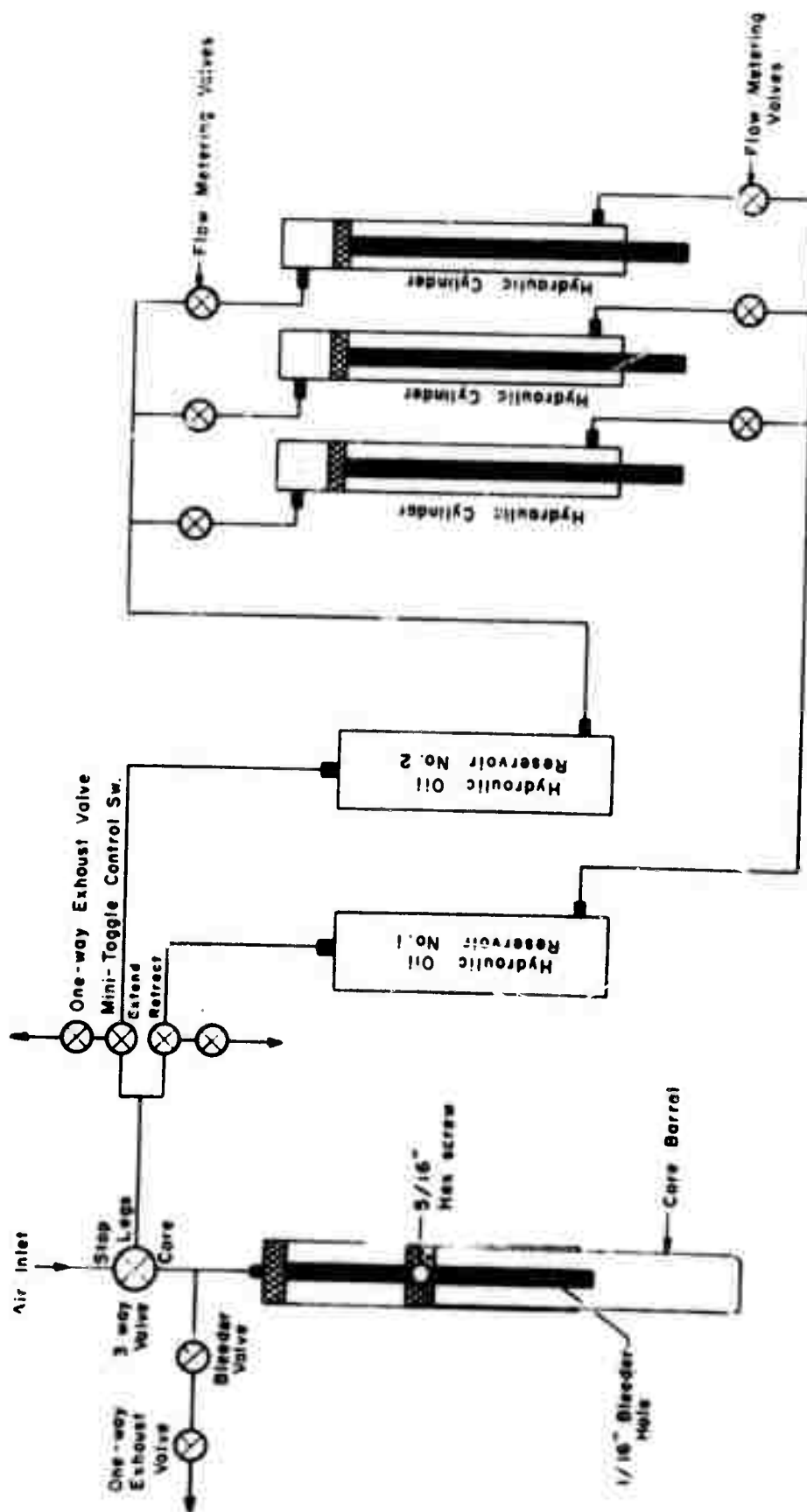


Figure 3-34. Diver operated corer piping diagram.

A complete cycle of sampling, excluding ship positioning and 2-point mooring time, takes approximately 10-20 minutes in water 40-60 feet deep. The corer is capable of sampling both semi-consolidated (clays) as well as unconsolidated sediments.

3.2.7 Research Vessel

All the field operations mentioned in this experiment were conducted from the R/V Doodlebug, a 40-foot converted launch (figure 3-35). The vessel is equipped with standard shipboard equipment consisting of a compass, single side band radio, radar, fathometer, a 4 KW diesel-electric generator to supply 110/220 VAC power to the recorders as well as a separate 7.5 KW, 110/220 VAC diesel-electric generator to operate the sparker seismic system. The vessel is powered by two 197 hp diesel engines with twin screws for easy maneuverability. Cruising speed is about 9 knots, although normally survey speeds average 4 to 5 knots. A 1/2-ton portable hoist with 600 feet of 3/16" stainless steel cable is mounted in the aft section for handling loads up to 1000 pounds or towing vehicles containing instruments.

Precision Navigation and Positioning System.

The precision radio location system is manufactured by Hastings-Raydist, Inc. (subsidiary of Teledyne, Inc.). It is used in referencing ship's position to geodetic control and for automatic real-time tracking during survey operations. Incorporated in the system is an electronic subsystem which enables real-time, on-line digital and graphical conversion of lane identification coordinates derived from the Raydist range-range mode system to x-y grid coordinates. The subsystem was developed by the Marine Minerals Technology Center. Diagrams and hardware



Figure 3-35. R/V DOODLEBUG.

components of the total system are shown in figures 3-36 and 3-37.

The ship's position and track are accurately located to within ± 10 feet based on daily repeatability checks of the calibrate value (geodetic control point). Details concerning the system and electronic subsystem may be found in a report by Barnes and Newman (1971).

3.2.8 Field Operations

The field test site selected for this investigation was originally intended for Monterey Bay, California; however time and circumstances prevented accomplishing this objective. The investigation reported herein is confined to a site in San Francisco Bay which had been intended for use as a preliminary site for shakedown tests of the systems and procedures prior to the Monterey Bay study. Although a thorough and detailed study as programmed for the Monterey Bay work was not conducted in the San Francisco Bay experiment, it is felt the data obtained is significant and representative of the goals desired and worthwhile documenting in this report (section 3.2.9).

Target Site.

An area immediately south and west of Red Rock in the northern reaches of San Francisco Bay and south of the San Rafael-Richmond Bridge was selected for the test site (figure 3-38). The bottom sediments in the survey area are of several types. Mud, silt, sand, rock and clays indurated with shells comprise some of the types of materials dredged from the bottom in earlier work by the National Ocean Survey (formerly U. S. Coast and Geodetic Survey -- refer to chart USC&GS No. 5532). The wide variability of sediment/rock type, shallow water, estuarine environment, and logistics were factors influencing the selection of

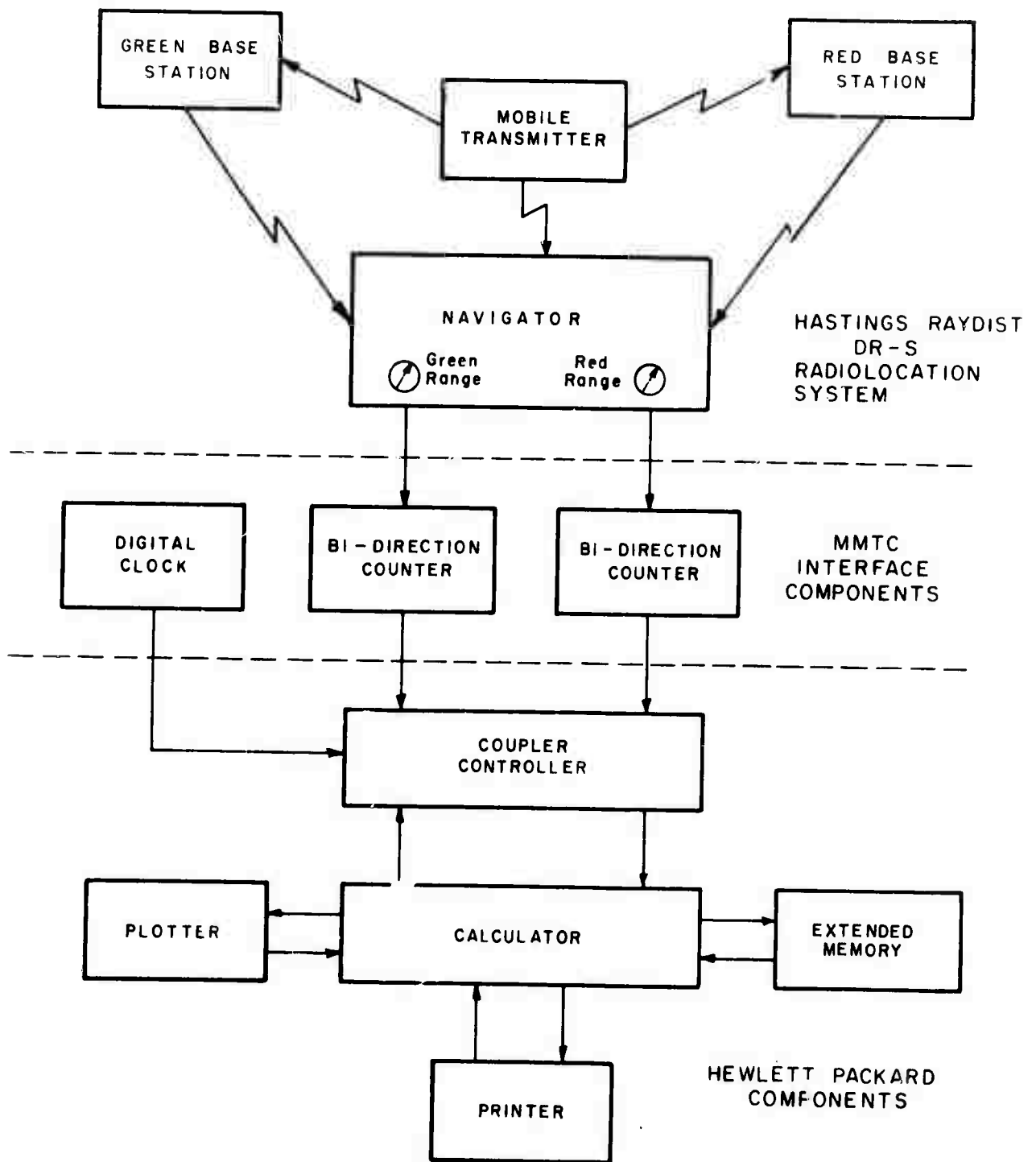


Figure 3-36. Block diagram basic navigation system and subsystem.

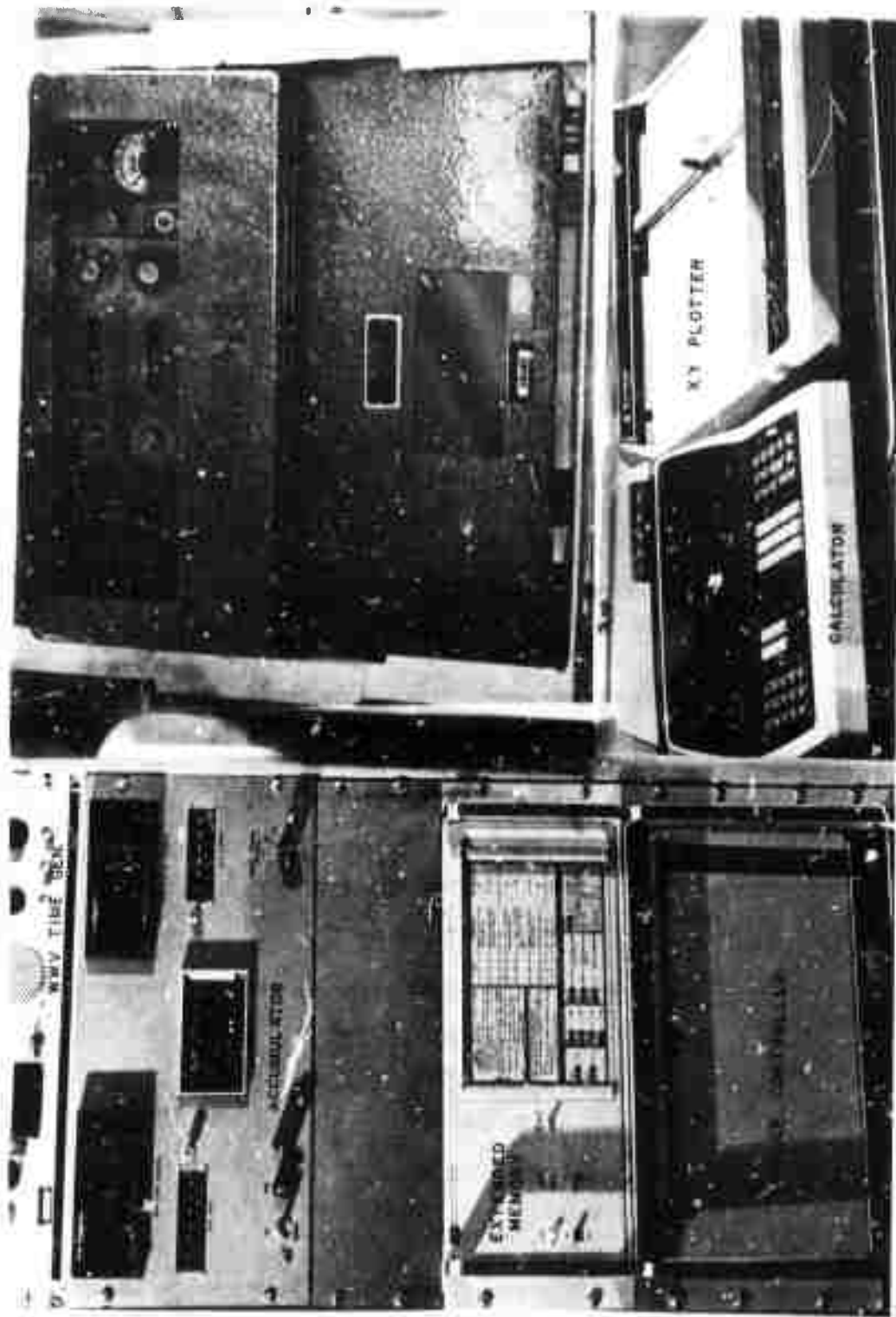


Figure 3-37. Hardware - navigation positioning system.

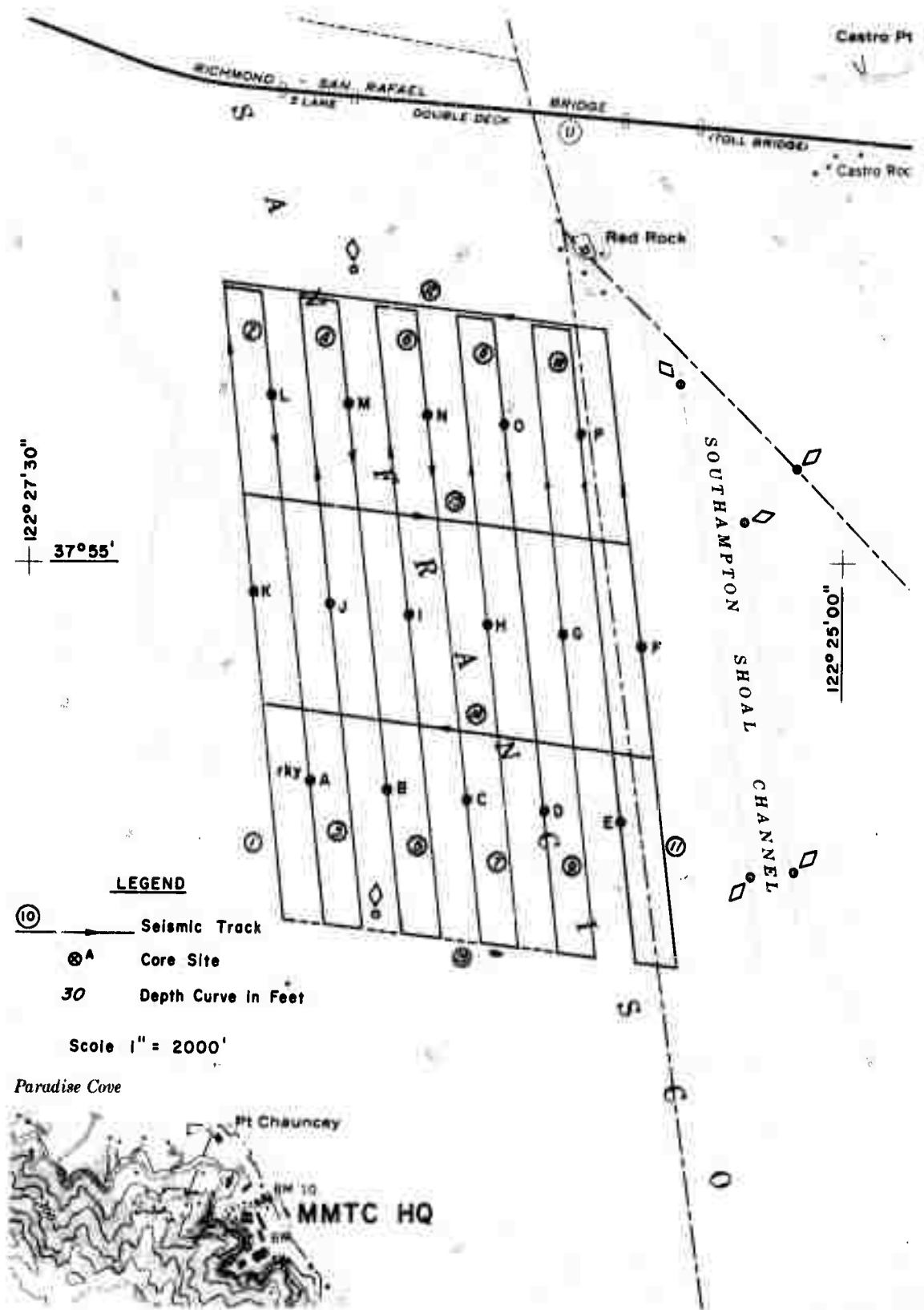


Figure 3-38. San Francisco Bay test site (proposed program).

the area and determining the core sites (see Appendix - Sect. 4.5)

A program was drawn to apply a dense grid pattern of 600 foot line spacing over an area of 1-1/2 square miles (figure 3-38). Core locations were designated at 16 sites, each located approximately 900 feet apart. The actual program proposed was completed almost in total and as programmed. Two separate seismic surveys were made at different times in August 1971 and September 1971. Figure 3-39 reflects the latter survey covering the actual work. Most of the reflectivity data was derived from the second survey. Seismic production amounted to about 26.5 miles of continuous seismic profiling. Sixteen core locations were occupied and at least one core was taken at each site. At several core sites two or more cores were taken. Core retention averaged about 90% for all sites. Water depth ranged from 26 to 41 feet (uncorrected), averaging about 33 feet. The bottom topography is generally uniform with only minor changes occurring in the western edge of the area in the vicinity of the Richmond Channel (figure 3-38).

Navigation Positioning.

The Raydist Model DR-S High Accuracy Short-to-Medium Range Radio-location system was used to provide precise positioning and guidance for the vessel (section 3.2.7.1). Two shore-based stations are required for the range-range system. The north station, designated "Red", is located at the University of California Field Station in Richmond and the south station, designated "Green", is located at the Treasure Island Naval Base in the center of San Francisco Bay mid-span of the Oakland-San Francisco Bay Bridge.

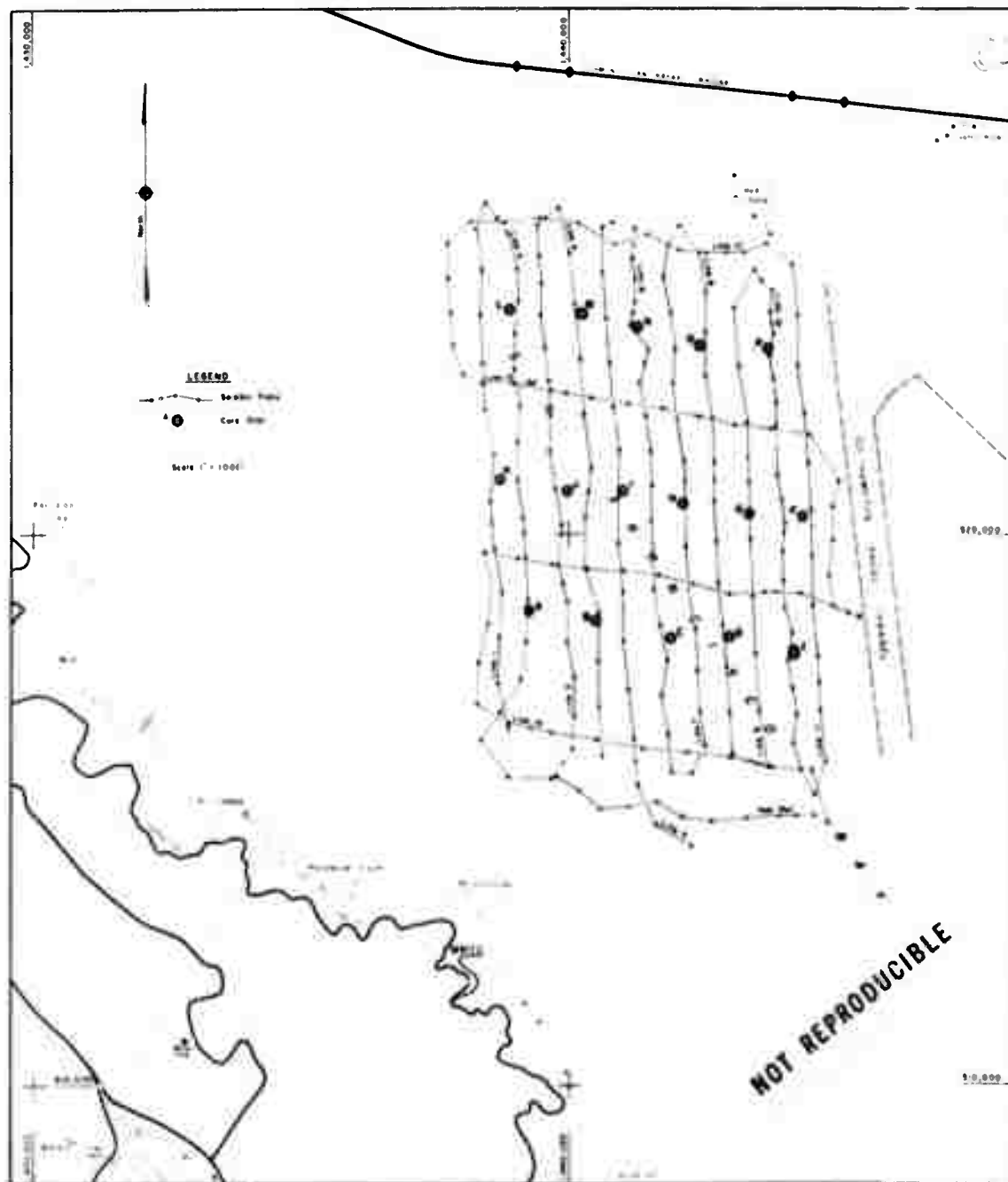


Figure 3-39. San Francisco Bay test site - actual survey.

140a

Pre-plots of profile track lines are drawn on transparent reusable overlays made from conventional maps using the California Grid system (Lambert Coordinates) as a reference. The boat operator uses the x-y plotter with preplotted track to guide him onto the desired course and to pre-designated core sites. The scale of the overlays is large enough to provide high resolution plotting capability (1 inch = 1000 feet). A Hewlett-Packard Model 9100A programmable calculator automatically converts the range-range "red" and "green" lane counts that reflect distance from each of the respective shore stations to the vessel (each lane equals 148.2282 feet) to x and y Lambert grid coordinates (California State Grid Coordinate System). The Hewlett-Packard Model 9125A digital plotter is fed these coordinates approximately every 1.3 seconds to provide a real-time automatic plotting navigation positioning system. A digital printer is commanded through the program to print out on-line the "red" and "green" lane counts, x and y coordinates and the time of print out. There is also a provision for digital depth data to be printed if it is required. Greenwich Mean Time is used as the reference for all events recorded in the navigation-positioning operation, and for ancillary recorders associated with the acoustic and magnetic tape recording systems.

The average position error for the runs made on a daily basis was .06 lane on the "red" count (8.9 feet) and .08 lanes on the "green" count (11.9 feet). The Raydist is a non line-of-sight system using ground wave transmission. Errors are felt to be caused by changes in velocity of wave propagation, not positioning the boat in the exact position when it is originally calibrated and recalibrated, or insufficient warmup time prior to commencing operations.

The subsystem interface also contains a digital clock with 5 selectable time outputs ranging from 1 minute to 30 minutes. This timer controls a marker interface which simultaneously marks the records of the fathometer, seismic recorder, Raydist strip chart recorder, and controls the Raydist digital printer (auxiliary unit to the HP printer). The vessel's location in lane counts is sequentially assigned station numbers that are used for annotation in addition to the time reference. The operator periodically annotates the records with the station number and time. The marker interface can also be manually operated to index significant events, such as occur during maneuvering, amplifier gain changes, calibration points, coring events, and so forth.

Survey and Sampling Operations.

The total complement of crew and project staff consists of a boat operator, an electronics technician and a geophysicist during seismic operations. The sampling work requires three divers and a geologist in addition to the boat operator and electronics technician.

Once the navigation system is calibrated, at a preselected geodetic control point, the vessel proceeds to the test area. The acoustic source and receiver units are deployed and towed in a side-by-side configuration approximately 65 feet astern of the vessel. Vessel speed during survey operations is maintained at about 4 - 5 knots. The seismic source is electronically detonated once every second and the received signal is recorded both in graphic form (variable density) and onto magnetic tape (section 3.2.5.3). Voice annotation on the tape, and written logs are maintained throughout the operations.

During sampling operations, the vessel is anchored and position movement is monitored on the x-y plotter readout (scale 1" = 50'). Coring is accomplished at slack tide to allow safe operations for the divers. Core production was limited to two per day mainly because of the strong currents produced by the changing tide. Details of the coring operation are noted in section 3.2.6.2.

3.2.9 Data Analysis

Core Sample Analysis.

The object of the core sample analysis phase of this investigation is to determine the character of the sediments in the area where the acoustic measurements are made. The analyses are directed toward obtaining grain-size and mass characteristics of the sediments. These measurements are used directly for correlation with the acoustic reflectivity measurements. Due to the shortage of time and personnel, only cursory mineralogical examinations have been made of the samples at the time of this report.

The samples were obtained with the MRTC-developed, diver-operated, bottom-sitting coring drill, which is capable of obtaining a core 70 centimeters long and 7.9 centimeters in diameter (sections 3.2.6 and 3.2.8.3). Most of the cores obtained during this investigation were between 60 and 65 centimeters in length. When the sample is taken, the core-barrels are sealed under water, brought to the surface, and stored in a vertical position during transit to the Tiburon laboratory. Usually, the laboratory processing begins within 2 to 4 hours after the sample is taken from the floor of San Francisco Bay.

Upon arrival in the laboratory, the exterior of the core-barrel is

cleaned and wiped dry, and the whole assembly (core-barrels, seals and contained sample) weighed. The seal is then removed and the excess water carefully siphoned off and its weight recorded. The depth to the solid material is then measured and recorded, and the volume, wet weight, and wet density of the sample calculated. The core-barrel is then placed in the horizontal core-extruder and extrusion of the core starts.

Samples for water content determinations are obtained by taking six slices 1 cm thick from the core as it is extruded from the barrel. These slices are caught in pre-weighed glass Petri dishes, and each set of six samples is weighed immediately, placed in a calibrated drying oven, and dried to constant weight. The process of obtaining the slices, weighing, and placing the samples in the drying oven consumes approximately 3 minutes per set of 6 samples. After the material for the water content determinations is obtained, Torvane^{2/} and Penetrometer^{2/} measurements are made on the face of the core remaining in the core-barrel. The core is extruded another 14 centimeters, cut off, and stored in plastic containers for future mineralogical analysis. This routine is repeated until no further core remains in the core-barrel.

Specific gravity (dry density) determinations are made on the water-content samples after they have been dried and weighed. A 50 - 60 gram split of the dried material is taken, crushed, and ground to approximately minus 100-mesh size and the specific gravity is obtained with a

^{2/}The Torvane and Penetrometer data are not included in this report because of suspected instrument malfunction.

Beckman Model 930 Air Comparison Pycnometer for each of three levels in the core; 0-6 cm, 20-26 cm, and 40-46 cm with 0 corresponding to the surface of the bay floor. The average of the three determinations is used as the dry density for the core sample.

The remainder of the water-content material is placed in a 200-mesh sieve and the minus 200-mesh material is washed from the sample into a 3-gallon plastic bucket, allowed to settle, and the clear water carefully decanted. The slurry remaining in the bucket is washed into a drying pan with a minimum amount of water and dried. The dried minus 200-mesh material is weighed, and a 35 gram split taken for sub-sieve analysis. Sub-sieve analysis is accomplished by the hydrometer method using 1000 ml graduate cylinders in a constant temperature water bath. Meanwhile, the plus 200-mesh material is dried and sieved through selected sieves using a mechanical sieve shaker. A 10- minute shaking cycle is used for the sieve analysis. A per cent finer cumulative curve is constructed from the sieving and hydrometer analyses and the median grain size, 25 per cent quartile, and the 75 per cent quartile picked off the curve. The arithmetic quartile deviation, the geometric quartile deviation (sorting coefficient of Trask) and the \log_{10} Sorting Coefficient are then calculated. A tabulation of the grain size and mass characteristics of all the sediment samples is presented in the Appendix (section 4.6).

Correlation of Mass Physical Properties to Reflectivity.

The grain size and mass properties data are correlated with the acoustic data using a linear regression program on a Hewlett-Packard Model 9100A Programmable Desk Top Calculator. The program calculates the equation of the straight line of best fit of a set of data points.

The best fit is determined by minimizing the sum of the squares of the deviations of the data points from the line. The program also calculates a correlation coefficient, r , an indication of goodness of fit. If $r = 0$, there is no correlation. If $r = \pm 1$, there is perfect correlation or a perfect fit. Correlations were run, where data available, on the 0-6 cm fraction, 20-26 cm fraction, 40-46 cm fraction, and also on the average value for the whole core of each of the grain size and mass characteristics obtained. The results of these correlations are shown in Tables 3-3 and 3-4, as well as the standard error per correlation.

3.2.10 Results and Conclusions

The magnitude of the correlation coefficients presented in Tables 3-3 and 3-4 corroborate Breslau's (1967) conclusion that a significant correlation exists between bottom loss and certain physical characteristics of the sediments. Most notable are the relationships between bottom loss and the sediment's porosity, grain size, and fine material (silt-clay) content. A comparison of the correlative values obtained in this investigation and those obtained by Breslau's (1967) much more extensive investigation is presented in Table 3-5. It should be noted that Breslau's data were obtained, for the most part, in the offshore marine environment where relatively uniform sediments prevail over large areas, whereas this investigation was conducted in essentially an estuarine environment wherein the character of the bottom sediments is extremely variable over very short distances. The comparability of the two sets of data is therefore rather remarkable and seemingly indicates a high degree of validity for the technique. Also, the improvement must, in part, be attributed to the use of precision radiolocation positioning and navigation equipment

Table 3-3. Correlation Between Bottom Loss ^{10/}
and Sediment Grain-Size

Sediment Grain Size (core interval)	Correlation Coefficient (r)	Standard Error ^{11/} dB/Unit
Median Grain Size (0-6cm)	.87	\pm .325
Median Grain Size (20-26cm)	.83	\pm .367
Median Grain Size (40-46cm)	.91	\pm .276
Median Grain Size (av for ea core)	.92	\pm .227
% (Silt & Clay) (0-6cm)	.93	\pm .252
% (Silt & Clay) (20-26cm)	.75	\pm .450
% (Silt & Clay) (40-46cm)	.89	\pm .308
% (Silt & Clay) (av for ea core)	.89	\pm .305
Shell content (0-6cm)	.004	\pm .643
Shell content (20-26cm)	.27	\pm .692
Shell content (40-46cm)	.13	\pm .609
Shell content (av for ea core)	.69	\pm .4651
Sorting Coefficient (0-6cm)	.89	\pm .291
Sorting Coefficient (20-26cm)	.78	\pm .395
Sorting Coefficient (40-46cm)	.83	\pm .356
Sorting Coefficient (av for ea core)	.92	\pm .252

^{10/} Bottom loss calculations are based on peak pressure amplitude measurements and Rayleigh Reflection Coefficient determinations.

^{11/} The standard error of estimate (S) is the standard deviation about a line of average relationship. Assuming a normal distribution, 68 per cent of all cases will lie within a range of $\pm S$, 95 per cent will fall within $\pm 2S$, and 99.7 per cent will fall within $\pm 3S$. In this instance, the relationship of bottom loss to the other variable is of interest. The values of S are therefore in terms of decibels (db) per unit of paired variable.

and developing a sampler that can obtain relatively undisturbed core samples.

Figures 3-40 and 3-41 provide graphic illustration of the practical value of the investigation. The 3-component diagram (figure 3-40) shows a marked propensity toward finer grained material in the San Francisco Bay test site. It is significant to also note the coincidence of the data along the western edge to the large area designated for dumping of spoils indicated in the nautical chart (USC&GS Chart 5532). The high degree of fines may be associated with the dump area (figure 3-41).

In producing maps from acoustic measurements such as represented by figure 3-41, it is important to realize how meaningful the distribution factors are. The lithologic designations (i.e., sand, clay, silt, etc.) illustrated on the map would appear at first sight to reflect only gross classification, without regard to their respective mass physical properties. However, the addition of bottom loss (dB) characterizes much more than lithology. Within the zone of influence there is an added dimension that can provide the practical-oriented engineer meaningful data regarding soil and rock properties. The combination can yield valuable information leading up to the prediction of parameters such as stability, bearing strengths, compressibility, etc.

Last, but not least, this knowledge can provide the ability to understand how disturbance of these materials (i.e., through turbidity, transportation of fines in solution) will affect the environment and influence the ecologic balance.

Table 3-4. Correlation Between Bottom Loss ^{12/}
and Sediment Mass Physical Properties

	Correlation Coefficient (r)	Standard Error of Estimate ^{13/}
Dry Density	.03	\pm .679
Wet Density	.70	\pm 4.166
Water Content (0-6cm)	.90	\pm .295
Water Content (20-26cm)	.84	\pm .374
Water Content (40-46cm)	.86	\pm .352
Water Content (average for each core)	.88	\pm .328
Void Ratio	.68	\pm .452
Porosity	.73	\pm .455

Table 3-5. Comparison of Correlative Values of MMTC vs Breslau (1967)

	Correlation Coefficient		Standard Error ^{13/} dB/Unit	
	MMTC	Breslau	MMTC	Breslau
Porosity	.73	.70	\pm .455	\pm .039
Grain Size	.92	.646	\pm .227	\pm .292
Sorting	.92	.343	\pm .252	\pm .660
Fine Material (Silt & Clay)	.89	.786	\pm .305	\pm .015

^{12/} Bottom loss calculations are based on peak pressure amplitude measurements and Rayleigh Reflection Coefficient determinations.

^{13/} The standard error of estimate (S) is the standard deviation about a line of average relationship. Assuming a normal distribution, 68 per cent of all cases will lie within a range of \pm S, 95 per cent will fall within \pm 2S, and 99.7 per cent will fall within \pm 3S. In this instance, the relationship of bottom loss to the other variable is of interest. The values of S are therefore in terms of decibels (db) per unit of paired variable.

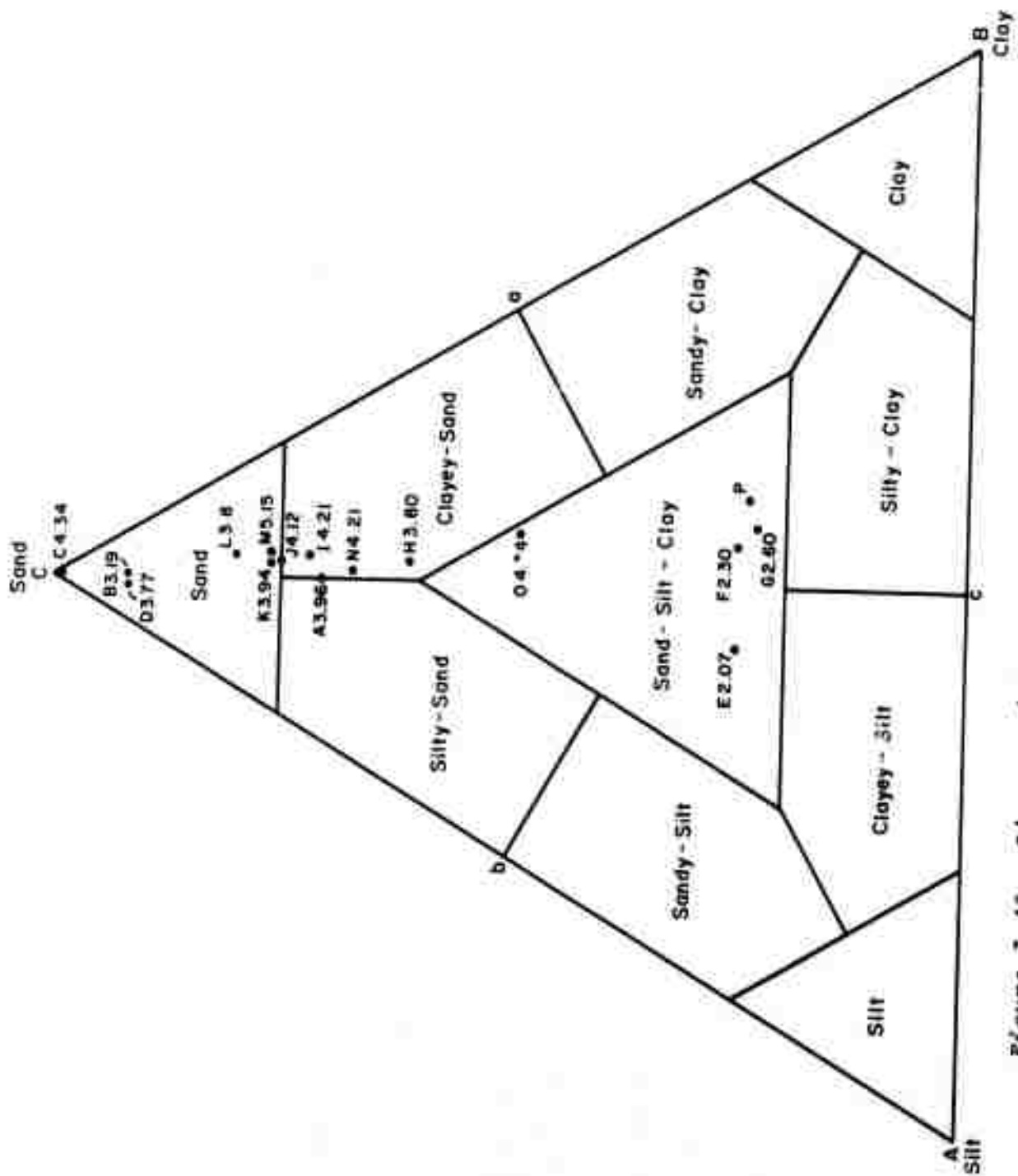


Figure 3-40. Diagram with associated bottom loss values (dB).

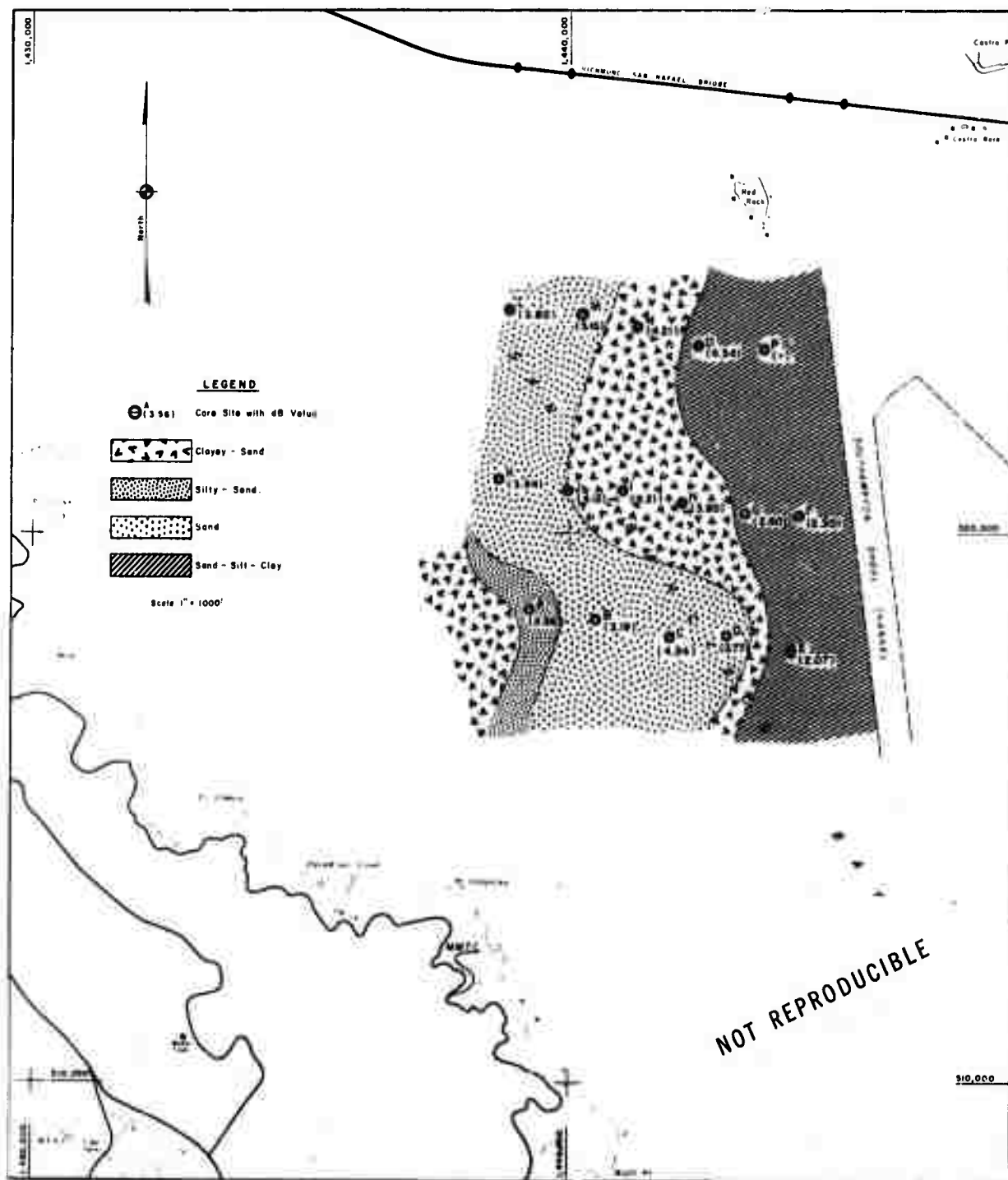


Figure 3-41. Bottom sediments composition - San Francisco Bay test area.

4. ACKNOWLEDGEMENTS

The authors wish to express their appreciation to several people for their assistance in the project. The work reported herein is a good example of team effort utilizing the abilities of several highly qualified technicians. Our special thanks go to the technical services staff of the Marine Minerals Technology Center, particularly Mr. Larry Jackson, Mr. Walter Takeyama, and Mr. Leai Kimrey, who directed much of the work entailing the seismic instrumentation and sediment sample operation and analysis. Credit for the line drawings and illustrations goes to Mr. Yok S. Gee, Cartographer. Mr. Richard Kessler directed the precision navigation and positioning operations. The conscientious attention to details in this report is one of the reasons the reflectivity experiment was so successful. The coring operations were directed by Mr. Richard Jenkins and supported by the diving group from MMTTC. Appreciation goes to the operators of the R/V DOODLEBUG, Captain Frank Pepper and Engineer Robert Matteson.

Acknowledgement is made to the University of California (Berkeley), Department of Engineering Geoscience, whose cooperation made the project possible. The advice and technical assistance given by the faculty in this Department played an important part in the overall project and the successful results of this report.

Finally, a special appreciation goes to Mrs. Ione Davis who painstakingly edited the text and also to Mrs. Virginia Jensen and Mrs. Helen McGarry who typed the draft and assisted in the final preparation of the report.

5. REFERENCES

- Archie, G. E. (1942), The electrical resistivity log as an aid in determining some reservoir characteristics; AIME, 146, 54-62.
- Barnes, B. B., and R. Newman (1971), A subsystem for electronic positioning and navigation at sea. Paper in Proceedings of the IEEE Conference on Engineering in the Ocean Environment, 121-146.
- Biot, M. A. (1962), Mechanics of deformation and acoustic propagation in porous media, J. Appl. Phys., 33, 1482-1498.
- Birch, F., V. F. Schairer, and H. C. Spicer (1942), Handbook of physical constants, Geological Soc. of Am., Special Paper 36, 325 pp.
- Bodholt, H. (1969), Scientific echo sounding systems--measuring target strength and back scattering strength, SIMRAD Tech. Bull. No. 5, SIMRAD, Inc., Kew Gardens, N.Y., 11 pp.
- Bouma, A. H., W. E. Sweet, F. B. Chmelik, and G. L. Huebner (1971), Ship-board and in situ electrical resistivity logging of unconsolidated marine sediments, in Proceedings, Third Annual Offshore Technology Conference, Houston, Texas, Vol. 1, Paper No. 1351, 253-268.
- Breslau, L. R. (1967), The normally-incident reflectivity of the sea floor at 12 KC and its correlation with physical and geological properties of naturally occurring sediments, Woods Hole Oceanographic Institution Reference No. 67-16, 131 pp.
- Breslau, L. R. (1964), Classification of sea-floor sediments with a ship-borne acoustic system, Woods Hole Oceanographic Contribution No. 1678 in *Le Petrole Et Mer*, Section 1, No. 132 (printed in France--English translation), 9 pp. Also in *La Revue Petroliere*, 1965 (reprint).
- Bucker, H. P. (1964), Normal-mode sound propagation in shallow water, J. Acoust. Soc. Am., 36, 251-258.
- Coggon, J. H., and H. F. Morrison (1970), Electromagnetic investigation of the sea floor, Geophys., 35, No. 3, 476-489.
- Connors, D. N., and K. Park (1967), The partial equivalent conductances of electrolytes in seawater, a revision; Deep-Sea Res., 14, 481-484.
- Cooley, J., P. Lewis, and P. Welch (1967), Historical notes on the FFT, IEEE Trans. on Audio and Electroacoustics, AV-15, No. 2, 76-79.
- Dakhnov, V. N. (1959), Geophysical well logging, Quarterly of the Colorado School of Mines, 57, No. 2, 445 pp.

- Davies, D. (1965), Dispersed Stonely waves on the ocean bottom, *Bull. Seismol. Soc. Am.*, 55, 903-918.
- Erchul, R. A., and V. A. Nacci (1971), The use of electrical resistivity measurements to predict porosity of marine sediments, in *Proceedings, The International Symposium on the Engineering Properties of Sea-Floor Soils and their Geophysical Identification*, Seattle, Washington, 296-308.
- Ewing, W. M., W. S. Jardetzky, and F. Press (1957), *Elastic Waves in Layered Media* (McGraw-Hill, New York), 380 pp.
- Flügge, W. (1967), *Viscoelasticity* (Blaisdell Press).
- Fung, Y. C. (1965), *Foundations of Solid Mechanics* (Prentice-Hall, Inc.).
- Garrels, R. M., and M. E. Thompson (1962), A chemical model for sea water at 25°C and one atmosphere total pressure, *Am. J. Sci.*, 260, 57-66.
- GE Transistor Manual (1964), 338.
- Grant, F. S., and G. F. West (1965), *Interpretation Theory in Applied Geophysics* (McGraw-Hill, New York), 584 pp.
- Griffiths, D. H., and R. King (1965), *Applied Geophysics for Engineers and Geologists* (Pergamon Press, Oxford), 78-82.
- Hamilton, E. L., and H. W. Menard (1956), Density and porosity of sea-floor surface sediments off San Diego, *The Bulletin of the Am. Assoc. of Petrol. Geol.* 40, 754-761.
- Hamilton, E. L. (1969), Sound velocity, elasticity and related properties of marine sediments, North Pacific, I, sediment properties, environmental control and empirical relationships; Naval Undersea Res. Develop. Center Tech. Publ. 143.
- Hamilton, E. L., H. P. Buckner, and D. L. Kein (1970a), Velocities of compressional and shear waves in marine sediments determined in situ from a research submersible; *J. Geophys. Res.*, 75, 4039-4049.
- Hamilton, E. L. (1970), Sound velocity and related properties of marine sediment, North Pacific, *J. Geophys. Res.*, 75, 4423-4446.
- Hamilton, E. L. (1970b), Reflection coefficients and bottom losses at normal incidence computed from Pacific sediment properties, *Geophys.*, 35, 995-1004.

- Hamilton, E. L. (1971), Elastic properties of marine sediments, J. Geophys. Res., 76, 579-603.
- Harvey, H. W. (1960), *The Chemistry and Fertility of Sea Waters* (Cambridge University Press), 4.
- Horn, D. R., B. M. Horn, and M. N. Delacy (1968), Correlation between acoustical and other physical properties of deep sea coes, J. Geophys. Res., 73, 1939-1957.
- International Oceanographic Tables (1966), National Institute of Oceanography of Great Britain and UNESCO.
- Jenkins, R., and W. Takeyama (1971), Bottom-sitting diver-operated core sampler, NOAA Report ERL-MMTC Tech. Memo. (in press), 13 pp.
- Jones, J. L., C. B. Leslie, and L. E. Barton (1964), Acoustic characteristics of underwater bottoms, J. of the Acous. Soc. of Am., 36, 154-163.
- Keller, G. H. (1965), Deep-sea nuclear sediment density probe, Deep-Sea Res., 12, 373-376.
- Keller, G. V., and F. C. Frischknecht (1966), *Electrical Methods in Geophysical Prospecting* (Pergamon Press, Oxford), 519 pp.
- Kermabon, A., C. Gehin, and P. Blavier (1969), A deep-sea electrical resistivity probe for measuring porosity and density of unconsolidated sediments, Geophysics, 34, No. 4, 554-571.
- Lewis, L. (1971), An investigation of ocean sediments using the deep ocean sediment probe, PhD thesis, Dept. of Ocean Engineering, Univ. of R.I., 76 pp.
- Li, W. N., and D. Taylor-Smith (1966), Identification of sea-floor sediments by a ship underway, Geophys. Prospecting, 19, No. 1, 45-47.
- Lieberman, L. N. (1948), Reflection of sound from coastal sea bottoms, The J. of the Acous. Soc. of Am., 20, 305-309.
- Longworth, L. G. (1932), Transference numbers of aqueous solutions of potassium chloride, sodium chloride, lithium chloride and hydrochloric acid at 25°C by the moving boundary method, J. Am. Chem. Soc., 54, 2751-2758.
- Lyman, J., and R. H. Fleming (1940), Composition of sea water, J. Marine Res., 3, 134-146.

- Mackenzie, K. V. (1960), Reflection of sound from coastal bottoms, *The J. of the Acous. Soc. of Am.*, 32, 221-231.
- Marke, P. A. B. (1965), The development and use of off-shore mineral exploration techniques, PhD thesis, Geophysics Dept., Imperial College, London, S.W. 7., 166-278.
- McKinney, C. M., and C. D. Anderson (1964), Measurements of backscattering of sound from the ocean bottom, *J. of the Acous. Soc. of Am.*, 36, 158-163.
- Mika, Thomas (1971), Personal Communication, Univ. of California, Berkeley.
- Mooney, H. M., and W. W. Wetzel (1956), *The Potentials about a Point Electrode and Apparent Resistivity Curves for a Two-, Three-, and Four-Layered Earth* (The University of Minnesota Press), 150 pp. (Available from University Microfilms, A Xerox Company, Ann Arbor, Michigan, U.S.A.).
- Nafe, J. E., and C. L. Drake (1963), Physical properties of marine sediments, 794-815, in Hill, M. N., Editor, *The Sea*, 3 (John Wiley and Sons, Inc., New York, London), 963 pp.
- Officer, C. B. (1958), *Introduction to the Theory of Sound Transmission* (McGraw-Hill Book Co., Inc., New York, Toronto, London), 284 pp.
- Parasnis, D. S. (1962), *Principles of Applied Geophysics* (Methuen, London; Wiley, New York), 176 pp.
- Park, K. (1964), Partial equivalent conductance of electrolytes in seawater, *Deep-Sea Res.*, 11, 729-736.
- Physics of Sound in the Sea, Part 1 - Transmission, Summary Technical Report of the National Defense Research Committee (1946), Section on Sound Transmission Studies.
- Preiss, K. (1967), Non-destructive measurement of the water content and density of sediment using radionuclides, in *Marine Geotechnique*, A. Richards, ed. (Univ. Illinois Press), 307-318.
- Preiss, K. (1968), In situ measurement of sediment density by gamma radiation, *Deep-Sea Res.*, 15, 637-641.
- Rayleigh, J. W. S. (1945), *The Theory of Sound*, 2 (Dover Publications, New York), 504 pp.
- Richards, A. F. (1962), Investigations of deep-sea sediment cores, Part 2, mass physical properties, U. S. Navy Hydrographic Office, Tech. Report TR-106, 146 pp.

- Rijkswaterstaat, The Netherlands (1969), Standard Graphs for Resistivity Prospecting; European Association of Exploration Geophysicists.
- Sarmiento, R., and R. A. Kirby (1962), Recent sediments of Lake Maracaibo, *J. of Sed. Pet.*, 32, 698-724.
- Schopper, J. (1966), A theoretical investigation of formation factor/permeability/porosity relationship using a network model, *Geophys. Prospect.*, 14, 301-341.
- Schreiber, B. C. (1968), Sound velocity in deep-sea sediments, *J. Geophys. Res.*, 73, 1259-1268.
- Shumway, G. (1960), Sound speed and absorption studies of marine sediments by a resonance method, Parts 1 and 2, *Geophysics*, 25, 451-467 and 659-682.
- Strick, E., and A. S. Ginzberg (1956), Stoneley-wave velocities for a fluid-solid interface, *Bull. Seism. Soc. Am.*, 46, 281-292.
- Sutton, G.H., H. Berkheimer, and J. E. Nafe (1957), Physical analysis of deep-sea sediments, *Geophysics*, 22, 779-812.
- Taylor-Smith, D., and W. N. Li (1966), Echo-sounding and sea-floor sediments, *Marine Geol.*, 4 (Elsevier Publishing Co., Amsterdam. Printed in The Netherlands), 353-364.
- Taylor-Smith, D. (1968), Physics and sea-floor minerals, *Contemp. Phys.*, 9, No. 6, 565-585.
- Terekhin, E. I. (1962), Theoretical basis of electrical probing with an apparatus immersed in water, in *Applied Geophysics U.S.S.R.*, ed. by N. Rast (Pergamon Press, MacMillan, New York), 169-195.
- Urick, R. J. (1954), The backscattering of sound from a harbour bottom, *The J. of the Acous. Soc., of Am.*, 26, 231-235.
- Urick, R. J., and D. S. Saling (1962), Backscattering of explosive sound from the deep sea bed, *The J. of the Acous. Soc. of Am.*, 34, 1721-1724.
- Van Nostrand, R. G., and K. L. Cook (1966), Interpretation of resistivity data, *Geol. Sur. Professional Paper 499*, U. S. G.P.O., Washington, D. C., 310 pp.
- Van'yan, L. L. (1956), Theoretical curves for electrical sea probing with a sea-bottom apparatus, *Applied Geophysics No. 50*, Gostoptekhlizdat.

- Vees, E., and H. F. Winterkorn (1967), Engineering properties of several pure clays as functions of mineral type, exchange ions, and phase composition; Highway Research Board No. 198, 68-70.
- Volker, A., and L. Dijkstra (1955), Determination des salinités des eaux dans le Sous-Sol du Zuiderzee par prospection géophysique, *Geophysical Prospecting*, 111, No. 2, 111-125.
- Von Arz, W. S. (1962), *Introduction to Physical Oceanography* (Addison-Wesley, Reading, Massachusetts), 422 pp.
- White, J. E. (1965), *Seismic Waves; Radiation, Transmission and Attenuation* (McGraw-Hill, New York), 302 pp.
- Wilde, P. (1969), Tables of formalities and p ion in sea water of total Cl, Na, K, Mg, Ca, Sr, Br, and SO₄ for the salinity range of 28 to 40 percent assuming dittemarian conservancy; University of California, Berkeley, 62-63.
- Wood, A. B. (1941), *A Textbook of Sound* (G. Bell, London), 578 pp.
- Wyllie, M. P. J., and A. R. Gregory (1953), Formation factors of unconsolidated porous media: influence of particle shape and effect of cementation, *Pet. Trans.*, 198, 103-110.

APPENDIX

A-1 Data for Resistivity vs Porosity Measurements

Sample I.D.	Water Conductivity mho/m	Porosity %	Resistivity ohm-m	Conductivity mho/m	Formation Factor
35x48 sand	4.70	42.8	0.757	1.32	3.56
		41.2	.782	1.28	3.68
		39.8	.807	1.24	3.79
		38.1	.836	1.20	3.94
48x65 sand	4.40	42.7	.806	1.24	3.55
		39.7	.900	1.11	3.96
		37.3	.945	1.06	4.33
100x150 sand	4.70	46.2	.674	1.48	3.12
		43.7	.713	1.41	3.35
		42.7	.723	1.38	3.40
		40.8	.802	1.25	3.77
		39.3	.812	1.23	3.82
4x6 dolomite	4.40	49.6	.683	1.46	3.00
		47.2	.718	1.39	3.16
		45.0	.757	1.32	3.33
		40.0	.811	1.23	3.57
9x10 dolomite	4.40	49.3	.732	1.37	3.22
		47.0	.786	1.27	3.46
		44.0	.846	1.18	3.86
14x20 dolomite	4.25	51.0	.743	1.35	3.17
		49.3	.786	1.27	3.34
		47.4	.832	1.20	3.53
65x103 dolomite	4.65	55.3	.584	1.71	2.72
		54.2	.594	1.68	2.83
		52.8	.634	1.58	2.97
		50.8	.673	1.49	3.12
		49.3	.678	1.47	3.15

Sample I.D.	Water Conductivity mho/m	Porosity %	Resistivity ohm-m	Conductivity mho/m	Formation Factor
35x48 sand	3.40	42.5	1.00	1.00	3.40
		40.7	1.04	0.980	3.55
		39.0	1.12	0.893	3.79
		36.5	1.19	0.840	4.05
		36.1	1.20	0.833	4.08
48x65 sand	3.43	43.9	0.965	1.04	3.30
		42.2	1.01	0.990	3.47
		40.3	1.07	0.934	3.68
		38.3	1.14	0.877	3.89
100x150 sand	3.47	44.7	0.955	1.05	3.32
		43.1	0.990	1.01	3.44
		41.3	1.04	0.962	3.63
		38.8	1.11	0.901	3.85
4x6 dolomite	3.48	49.0	0.842	1.19	2.93
		47.4	.881	1.135	3.07
		46.2	.895	1.12	3.13
		44.4	.955	1.05	3.23
9x10 dolomite	3.48	50.3	.881	1.135	3.07
		48.5	.935	1.07	3.26
		47.3	.970	1.03	3.38
		45.6	1.02	0.980	3.57
		44.3	1.05	.953	3.68
14x20 dolomite	3.48	51.6	.891	1.12	3.11
		50.0	.945	1.06	3.30
		48.4	1.01	0.990	3.51
		46.1	1.06	.943	3.71
65x100 dolomite	3.48	54.5	.827	1.21	2.88
		52.0	.852	1.17	2.97
		50.8	.881	1.135	3.07
		48.3	.955	1.05	3.33

Sample I.D.	Water Conductivity mho/m	Porosity %	Resistivity ohm-m	Conductivity mho/m	Formation Factor
35x48 sand	1.67	42.7	2.05	0.488	3.43
		40.6	2.16	.463	3.56
		38.3	2.32	.432	3.87
		36.3	2.46	.407	4.12
48x65 sand	1.67	44.6	1.93	.518	3.23
		42.6	2.08	.482	3.46
		40.7	2.18	.458	3.64
		37.4	2.42	.413	4.05
100x150 sand	1.67	46.3	1.79	.559	2.99
		43.4	1.91	.524	3.20
		42.2	1.98	.505	3.30
		39.2	2.28	.438	3.81
4x6 dolomite	1.67	50.0	1.66	.603	2.77
		48.5	1.72	.582	2.87
		47.0	1.78	.562	2.97
		43.5	1.98	.505	3.30
9x10 dolomite	1.67	50.3	1.73	.578	2.89
		48.7	1.84	.543	3.07
		47.2	1.95	.513	3.24
		43.7	2.15	.465	3.59
14x20 dolomite	1.74	53.3	1.63	.613	2.84
		51.9	1.69	.592	2.93
		50.3	1.78	.562	3.10
		48.7	1.88	.533	3.28
		46.5	1.98	.505	3.45
65x100 dolomite	1.76	55.9	1.43	.700	2.61
		54.1	1.53	.654	2.69
		53.2	1.55	.645	2.73
		51.8	1.62	.617	2.84
		50.0	1.73	.578	3.03

A-2 Calculation of the Potential Field Due to a Point Source of Current over a Two-layered Sea Floor

A-2-1 Introduction

In order to develop curves such as those shown in figures 2-14 and 2-15, the potentials about a point source of current on the sea floor must be known. Terekhin (1962) has derived a general method for calculating the potentials over a bottom with any number of layers, and Van'yan (1956) has developed curves for a limited number of cases. Marke (1965) has done a more detailed study of a Wenner array on the sea floor over a single submarine layer. In this section, equations for a point source of current over a one- or two-layered bottom will be developed and a computer program for calculating these potentials will be presented.

The necessary relationships between current density, conductivity, charge density, potential, and time are:

$$\text{Ohm's law: } \vec{J} = \sigma \vec{E} = \vec{E} / \rho \quad (4.1)$$

$$\text{Continuity equation: } \vec{\nabla} \cdot \vec{J} = -\partial \rho / \partial t \quad (4.2)$$

$$\text{Electric field intensity: } \vec{E} = -\vec{\nabla} V \quad (4.3)$$

where \vec{J} is current density

σ is electrical conductivity

ρ is electrical resistivity

$\vec{\nabla}$ is the gradient operator,

(In rectangular coordinates)

t is time

V is potential

Combining these, and assuming the medium to be homogeneous and isotropic, gives

$$\sigma \nabla^2 V = \partial \rho / \partial t$$

or

$$\nabla^2 V = I \rho \quad (4.4)$$

where I is the current generated at a point

$$\nabla^2 \text{ is the Laplacian operator, } \left(\frac{\partial^2}{\partial x^2} + \frac{\partial^2}{\partial y^2} + \frac{\partial^2}{\partial z^2} \right)$$

(in rectangular coordinates)

if no current is being generated at the point,

$$\nabla^2 V = 0 \quad (4.5)$$

The potential V at any point in a region in which current is flowing is given by (4.4), and, if no current is being generated at the point, the potential is given by (4.5). For the special case of a whole space containing a point source of current, the solution to (4.4) is

$$V = I \rho / 4\pi R \quad (4.6)$$

where R is the distance from the current source.

A-2-2 General Solution

In cylindrical coordinates (4.5) may be expressed as

$$\nabla^2 V(r, \theta, z) = \frac{\partial^2 V}{\partial r^2} + \frac{1}{r} \frac{\partial V}{\partial r} + \frac{\partial^2 V}{\partial z^2} + \frac{1}{r^2} \frac{\partial^2 V}{\partial \theta^2} = 0 \quad (4.7)$$

In our problem, we will have no θ dependence so (4.7) may be simplified to

$$\frac{\partial^2 V}{\partial r^2} + \frac{1}{r} \frac{\partial V}{\partial r} + \frac{\partial^2 V}{\partial z^2} = 0 \quad (4.8)$$

By separating variables, the solution to (4.8) is shown to be

$$V(r, z) = \int_0^\infty [A(\lambda)e^{\lambda z} + B(\lambda)e^{-\lambda z}] J_0(\lambda r) d\lambda \quad (4.9)$$

where

A and B are constants

λ is a dummy variable

J_0 is the Bessel function of order zero

A-2-3 Particular Solution

The two-layer case analyzed is shown in figure 4-1. In any layer not containing the current source, the potential is given by:

$$V_i(r, z) = \int_0^\infty [A_i(\lambda)e^{\lambda z} + B_i(\lambda)e^{-\lambda z}] J_0(\lambda r) d\lambda \quad (4.9)$$

where i is 2, 1, or -1. In layer zero, the particular solution (4.6) must be added:

$$V_0 = \frac{I\rho_0}{4\pi R} + \int_0^\infty [A_0(\lambda)e^{\lambda z} + B_0(\lambda)e^{-\lambda z}] J_0(\lambda r) d\lambda ,$$

where $R = \sqrt{r^2 + z^2}$

$$\text{Letting } q_0 = \frac{I\rho_0}{4\pi} , \quad (4.10)$$

the complete solution to the problem may be expressed by the following set of equations:

$$V_2 = \int_0^\infty [A_2(\lambda)e^{\lambda z} + B_2(\lambda)e^{-\lambda z}] J_0(\lambda r) d\lambda \quad (4.11)$$

$$V_1 = \int_0^\infty [A_1(\lambda)e^{\lambda z} + B_1(\lambda)e^{-\lambda z}] J_0(\lambda r) d\lambda \quad (4.12)$$

$$V_0 = \frac{q_0}{R} + \int_0^\infty [A_0(\lambda)e^{\lambda z} + B_0(\lambda)e^{-\lambda z}] J_0(\lambda r) d\lambda \quad (4.13)$$

$$V_{-1} = \int_0^\infty [A_{-1}(\lambda)e^{\lambda z} + B_{-1}(\lambda)e^{-\lambda z}] J_0(\lambda r) d\lambda \quad (4.14)$$

The boundary conditions at each interface are:

$$\left. \begin{aligned} V_i &= V_{i-1} \\ \frac{1}{\rho_i} \frac{\partial V_i}{\partial z} &= \frac{1}{\rho_{i-1}} \frac{\partial V_{i-1}}{\partial z} \end{aligned} \right\} \quad i = 2, 1, 0 \quad (4.15)$$

$$(4.16)$$

and

$$V_2 \rightarrow 0 \quad \text{as } z \rightarrow +\infty \quad (4.17)$$

$$V_{-1} \rightarrow 0 \quad \text{as } z \rightarrow -\infty \quad (4.18)$$

Grant and West (1965) derive equations (4.15) and (4.16) on pages 404-405, and Van Nostrand and Cook (1966) treat the problem outlined above for the land case in detail.

By using the Weber-Lipschitz identity,

$$\frac{1}{R} = \int_0^{\infty} e^{-\lambda z} J_0(\lambda r) d\lambda ; z \geq 0 \quad (4.19)$$

$$\frac{1}{R} = \int_0^{\infty} e^{\lambda z} J_0(\lambda r) d\lambda ; z \leq 0 \quad (4.20)$$

defining

$$k_{01} = (\rho_0 - \rho_1)/(\rho_0 + \rho_1) \quad (4.21)$$

$$k_{21} = (\rho_2 - \rho_1)/(\rho_2 + \rho_1) \quad (4.22)$$

$$k_{-10} = (\rho_{-1} - \rho_0)/(\rho_{-1} + \rho_0) \quad (4.23)$$

and doing the necessary algebra, we arrive at the desired solution for V_1 , the potential in the water layer:

$$V_1 = q_0 \int_0^{\infty} \frac{(F_0 C_2 + 1) + C_3 (F_0 + 1)}{(1 + C_1)} \left[\frac{C_1}{C_2} e^{\lambda z} + e^{-\lambda z} \right] J_0(\lambda r) d\lambda \quad (4.24)$$

where

$$F_0 = \frac{k_{01} - C_1 - C_3 (C_1 - k_{01})}{C_2 (C_1 k_{01} - 1) + C_3 (C_1 - 1)} \quad (4.25)$$

$$C_1 = k_{21} e^{-2\lambda h} \quad (4.26)$$

$$C_2 = e^{2\lambda b} \quad (4.27)$$

$$C_3 = k_{-10} e^{-2\lambda \ell} \quad (4.28)$$

For the case of practical interest, where medium 2 is air, the source and measuring electrodes are both on the sea floor, $b = 0$, $Z = 0$, and

$\rho_2 \rightarrow \infty$, $C_1 = e^{-2\lambda h}$, and $C_2 = 1$. Then, letting

$$F_0 = \frac{(k_{01} - e^{-2\lambda h})(1 + C_3)}{(e^{-2\lambda h} k_{01} - 1) + C_3(e^{-2\lambda h} - 1)} \quad (4.29)$$

leads to

$$V_1 = q_0 \int_0^\infty (F_0 - 1) J_0(\lambda r) d\lambda \quad (4.30)$$

For the simplest case, where $h \rightarrow \infty$ and there is only a single sediment layer, $C_3 \rightarrow 0$, and

$$V_{1/z=0} = V_{0/z=0} = \frac{q_0}{r} + q_0 \int_0^\infty \left[\frac{k_{01} - e^{-2\lambda h}}{e^{-2\lambda h} k_{01} - 1} \right] J_0(\lambda r) d\lambda \quad (4.31)$$

For the case where $(r/h) \rightarrow 0$ (the water is very deep, or the array very small),

$$V \rightarrow \frac{q_0}{r} + q_0 \int_0^\infty -k_{01} J_0(\lambda r) d\lambda,$$

or

$$V \Big|_{r/h \rightarrow 0} \rightarrow \frac{q_0}{r} \left[\frac{2\rho_1}{\rho_0 + \rho_1} \right] \quad (4.32)$$

if $(r/h) \rightarrow \infty$ (the array is very large, or the water very shallow),

$$V \rightarrow \frac{q_0}{r} + q_0 \int_0^\infty \left[\frac{k_{01} - 1}{k_{01} + 1} \right] J_0(\lambda r) d\lambda,$$

or

$$V \Big|_{r/h \rightarrow \infty} \rightarrow \frac{Zq_0}{r} = \frac{I\rho_0}{2\pi r} \quad (4.33)$$

which is the correct value for a point source over a half space.

A-2-4 Deep Water, Single-Layer Approximation

In many actual situations, the water depth and the thickness of the first layer of sediments will be much greater than the electrode spacing a . For this case, a useful formula relating the formation factor, $\rho_{\text{sediment}} / \rho_{\text{water}}$, to the measured parameters a , $\Delta V / I$, and ρ_w may be derived from equation (4.32) as shown below.

From equation (4.32), with h and l in figure 4-1 much greater than a ,

$$V_r \rightarrow \frac{I \rho_s}{4\pi r} \left[\frac{2 \rho_w}{\rho_w - \rho_s} \right]$$

where ρ_w is the resistivity of the water, and ρ_s is the resistivity of the sediment. For the Wenner array,

$$\Delta V = 2(V_a - V_{2a})$$

or

$$\Delta V \left| \begin{array}{l} h \gg a \\ l \gg a \end{array} \right. = \frac{I \rho_s \rho_w}{2\pi a (\rho_s + \rho_w)} \quad (4.34)$$

solving for ρ_s / ρ_w ,

$$\rho_s / \rho_w = \frac{1}{\frac{\rho_w}{2\pi a \frac{\Delta V}{I}} - 1} \quad (4.35)$$

This is the formula used in plotting figure 2-20.

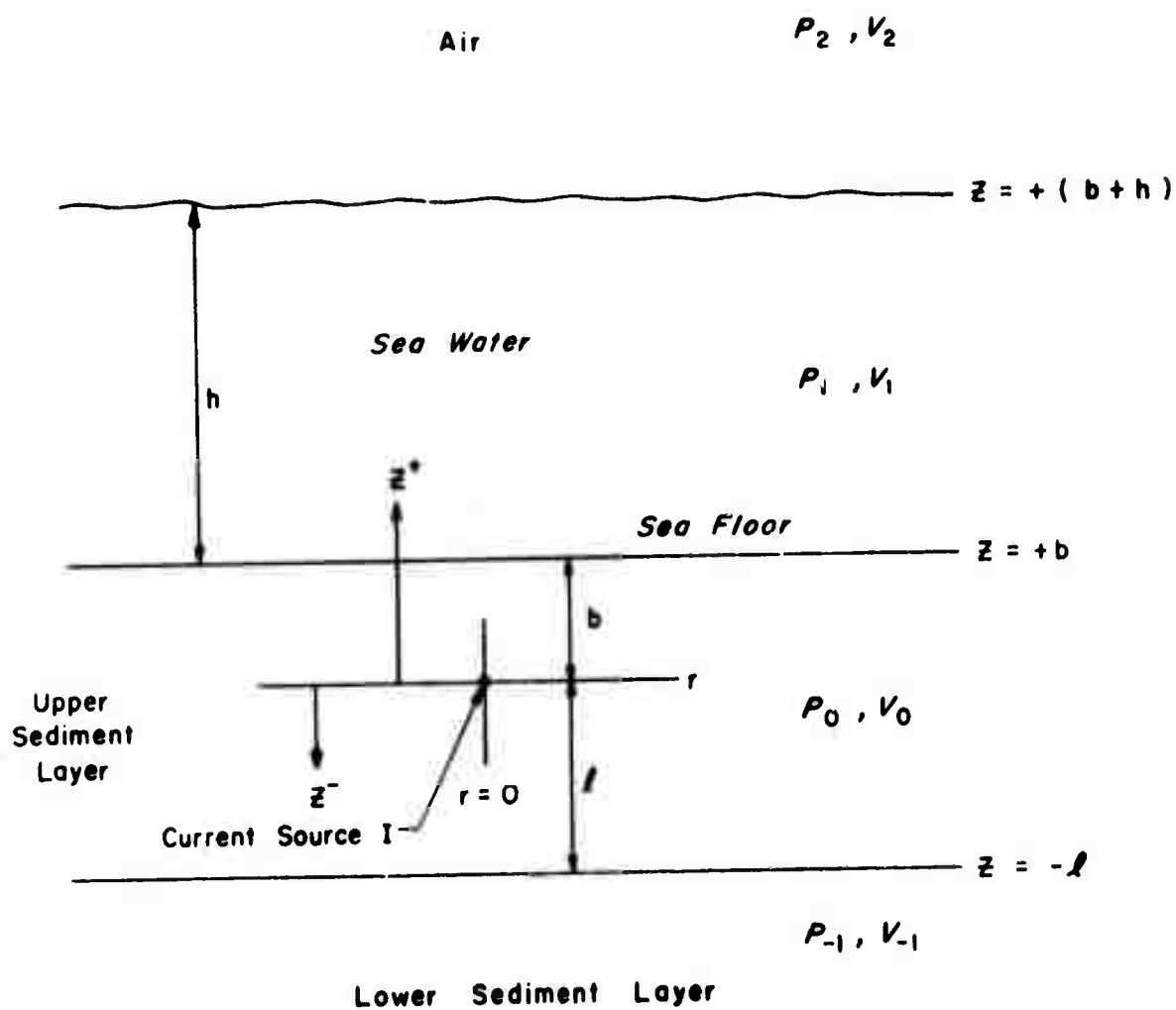


Figure 4-1. General two-layer case.

A-2-5 Computer Solution

Equations (4.24), (4.30) and (4.31) cannot be expressed in a closed form suitable for calculation by hand. It was decided, therefore, to set up a computer program to solve these equations by numerical integration. Only the programming for equation (4.31) will be described in detail here. Programs for the more general cases are more complex, but similar in general approach.

The integral part of equation (4.31) is in the form of a Bessel function multiplied by the modulating function F , where

$$F = \frac{k_{01} - e^{-2\lambda h}}{e^{-2\lambda h} k_{01} - 1} \quad (4.36)$$

$$\text{i.e.,} \quad V_1 = \frac{q_0}{r} + q_0 \int_0^{\infty} F(k_{01}, \lambda, h) J_0(\lambda r) d\lambda \quad (4.37)$$

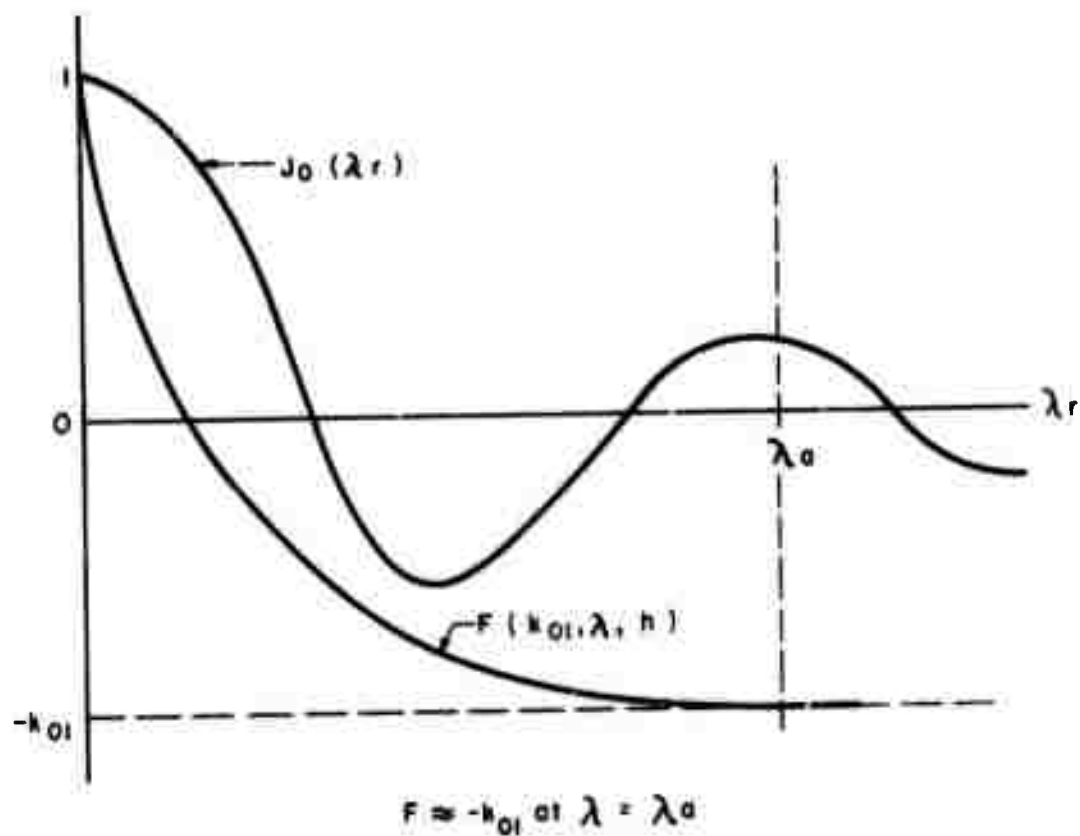
These two functions are shown graphically in figure 4-2.

$J_0(\lambda r)$, approaches zero and F approaches $-k_{01}$, as λr approaches infinity.

The program finds λ_a , the value of λ at which F is equal to $-k_{01}$ with some small specified error. It then evaluates the integral portion of (4.31) numerically by using the equation

$$\int_0^{\infty} F J_0(\lambda r) d\lambda \approx \int_{\lambda=0}^{\lambda=\lambda_a} F J_0(\lambda r) d\lambda - k_{01} \left[\frac{1}{r} - \int_0^{\lambda_a} J_0(\lambda r) d\lambda \right] \quad (4.38)$$

The program used to calculate the values of V for figure 2-15 is included as section 4.2.6.



Not to scale

Figure 4-2. Modulated Bessel function.

A-3 Relationships for Viscoelastic Model

A-3-1 Notation Summary

<u>Symbol</u>	<u>Description</u>
a_s	Shear-wave attenuation coefficient
a_p	Compressional-wave attenuation coefficient
E	Young's modulus
K_I	Bulk modulus representing wave energy damping
K_{R-I}	Bulk modulus representing elastic response
Q_{s-I}	Shear-wave dissipation function
Q_p	Compressional-wave dissipation function
v_s	Shear-wave velocity
v_p	Compressional-wave velocity
ϕ	Bulk density
λ_I	Lamé constant representing wave energy damping
λ_R	Lamé constant representing elastic response
μ_I	Rigidity representing wave energy damping
μ_R	Rigidity representing elastic response
σ	Poisson's ratio
ω	Angular frequency

A-3-2 Measured Parameters

Property	Symbol	Definition
Shear-wave dissipation function	Q_s^{-1}	$Q_s^{-1} = \frac{\mu_I}{\mu_R} = \frac{\frac{2\omega a s}{V_s}}{\left(\frac{w}{V_s}\right)^2 - a_s^2}$

Compressional-wave dissipation function	Q_p^{-1}	$Q_p^{-1} = \frac{K_I + \frac{4}{3}\mu_I}{K_R + \frac{4}{3}\mu_R} = \frac{\frac{2\omega a p}{V_p}}{\left(\frac{w}{V_p}\right)^2 - a_p^2}$
---	------------	---

Shear-wave velocity	V_s	$V_s = \left[\operatorname{Re} \sqrt{\frac{\phi}{\mu}} \right]^{-1} = \sqrt{\frac{\mu_R}{p}} \sqrt{\frac{2(1 + Q_s^{-2})}{\sqrt{1 + Q_s^{-2}} + 1}}$
---------------------	-------	---

Compressional-wave velocity	V_p	$V_p = \left[\operatorname{Re} \sqrt{\frac{\phi}{K + \frac{4}{3}\mu}} \right]^{-1} = \sqrt{\frac{K_R + \frac{4}{3}\mu_R}{\phi}} \sqrt{\frac{2(1 + Q_p^{-2})}{\sqrt{1 + Q_p^{-2}} + 1}}$
-----------------------------	-------	--

A-3-3 Sediment Properties

Property	Symbol	Method of Calculation
shear-wave dissipation function	Q_s^{-1}	$Q_s^{-1} = \frac{2\omega a_s}{V_s} \left/ \left(\frac{\omega}{V_s} \right)^2 - a_s^2 \right.$
compressional- wave dissipation function	Q_p^{-1}	$Q_p^{-1} = \frac{2\omega a_p}{V_p} \left/ \left(\frac{\omega}{V_p} \right)^2 - a_p^2 \right.$
rigidity representing elastic response	μ_R	$\mu_R = \phi V_s^2 \left[\frac{\sqrt{1 + Q_s^{-2} + 2}}{2(1 + Q_s^{-2})} \right]$
rigidity representing wave energy damping	μ_I	$\mu_I = \mu_R Q_s^{-1}$
bulk modulus representing elastic response	K_R	$K_R = V_p^2 \phi \left[\frac{\sqrt{1 + Q_p^{-2} + 1}}{2(1 + Q_p^{-2})} \right] - \frac{4}{3} \mu_R$
bulk modulus representing wave energy damping	K_I	$K_I = Q_p^{-1} (K_R + \frac{4}{3} \mu_R) - \frac{4}{3} \mu_I$
Lamé constant representing elastic response	λ_R	$\lambda_R = K_R - \frac{2}{3} \mu_R$

A-3-3 Sediment Properties (cont'd)

Property	Symbol	Method of Calculation
Lamé constant representing wave energy damping	λ_I	$\lambda_I = K_I - \frac{2}{3} \mu_I$
Poisson's Ratio	σ	$\sigma = \frac{\left[\frac{V_P \sqrt{\frac{2(1 + Q_s^{-2})}{1 + Q_s^{-2} + 1}}}{V_S \sqrt{\frac{2(1 + Q_p^{-2})}{1 + Q_p^{-2} + 1}}} \right]^{-2}}{2 \left[\frac{V_P \sqrt{\frac{2(1 + Q_s^{-2})}{1 + Q_s^{-2} + 1}}}{V_S \sqrt{\frac{2(1 + Q_p^{-2})}{1 + Q_p^{-2} + 1}}} \right]^{-2} - 2}$
Young's modulus	E	$E = \phi V_s^2 (1 + \sigma) \left[\frac{1 + Q_s^{-2} + 1}{1 + Q_s^{-2}} \right]$

A-4 Derivations of Rayleigh Reflection Coefficient Equations and Bottom Loss

The intensity of an echo which is specularly reflected in the simple model of the sea floor described previously is given by:

$$I_R = I_S \cdot K \cdot \frac{(1)}{(2D)^2} e^{-\alpha 2D} \quad (\text{Eq. 1})$$

where:

I_R = echo intensity

I_S = source intensity

K = fractional loss of intensity at the sea floor

$\frac{1}{(2D)^2}$ = transmission loss due to spherical spreading
 $e^{-\alpha 2D}$ = transmission loss due to dissipative attenuation of sound in seawater

furthermore;

$$I_R = \frac{P_R^2}{\rho_1 c_1} \quad (\text{Eq. 2}) \text{ and, } I_S = \frac{P_S^2}{\rho_1 c_1} \quad (\text{Eq. 3})$$

where:

P_R = pressure of the echo pulse

P_S = pressure of the source pulse

ρ_1 = density of seawater

c_1 = velocity of seawater

Eq. 1 becomes:

$$\frac{P_R^2}{\rho_1 c_1} = \frac{P_S^2}{\rho_1 c_1} \cdot K \cdot \frac{1}{(2D)^2} e^{-\alpha 2D} \quad (\text{Eq. 4})$$

assuming P_S is pressure estimated at $D = 1$.

Taking the integral with respect to time of both sides of Eq. 4 gives:

$$\text{where: } \frac{1}{\rho_1 c_1} \int_T^{T+\tau} P_R^2 dt = \frac{1}{\rho_1 c_1} K \frac{1}{(2D)^2} e^{-\alpha 2D} \int_0^\tau P_S^2 dt \quad (\text{eq. 5})$$

T = echo arrival time

τ = time duration of transmitted pulse

Since the source generates α sine wave,

$$\int_0^T P_S^2 dt = P_S^2(\text{RMS}) \cdot T \quad (\text{Eq. 6})$$

where the root mean square (RMS) of the pressure is equal to the peak pressure divided by the square root of two, Eq. 5 becomes:

$$\frac{1}{\rho_1 c_1} \int_T^{T+T} P_R^2 dt = \frac{1}{\rho_1 c_1} K \frac{1}{(2D)^2} e^{-\alpha 2D} P_S^2(\text{RMS}) \cdot T \quad (\text{Eq. 7})$$

It is seen that K may be defined on a peak pressure basis through Eq. 4 thusly;

$$K = \frac{P_R^2}{P_S^2} (2D)^2 \frac{1}{e^{-\alpha 2D}} \quad (\text{Eq. 8})$$

If P_{INC} represents pressure of the wave front incident on the seafloor and P_{REF} represents the pressure of the wave front reflected from the seafloor, then, K, the fractional loss of intensity at the seafloor is given by;

$$K = \frac{P_{\text{REF}}^2 / \rho_1 c_1}{P_{\text{INC}}^2 / \rho_1 c_1} = \left(\frac{P_{\text{REF}}}{P_{\text{INC}}} \right)^2 \quad (\text{Eq. 9})$$

For the model and incident plane waves, the ratio of the pressure of the wave front incident on the seafloor to the pressure of the wave front reflected from the seafloor is given by the Rayleigh Reflection Coefficient (17) (18) thusly;

$$R = \frac{P_{\text{REF}}}{P_{\text{INC}}} = \frac{\frac{\rho_2}{\rho_1} - \frac{\sqrt{c_1^2/c_2^2 - \sin^2 \theta}}{\sqrt{1 - \sin^2 \theta}}}{\frac{\rho_2}{\rho_1} + \frac{\sqrt{c_1^2/c_2^2 - \sin^2 \theta}}{\sqrt{1 - \sin^2 \theta}}} \quad (10)$$

where:

ϕ = the angle of incidence (for normal incidence $\phi = 0$;

which was the case for this investigation)

The Rayleigh Equation (Eq.10) is simplified for the case in hand thusly;

$$R = \frac{\rho_2 c_2 - \rho_1 c_1}{\rho_2 c_2 + \rho_1 c_1} \quad (\text{Eq. 11})$$

where the expression ρc is called the acoustic impedance of the medium and is designated as Z . Eq. 11 becomes by substitution:

$$R = \frac{Z_2 - Z_1}{Z_2 + Z_1} \quad (\text{Eq. 12})$$

where

Z_2 = acoustic impedance of seawater

Z_1 = acoustic impedance of the sediment

The relationship between the fractional loss of intensity at the seafloor, K , and the Rayleigh Reflection Coefficient, R , is shown by Eq. 9 to be:

$$K = R^2 \quad (\text{Eq. 13})$$

Since it is convenient to express hydroacoustic measurements in decibel form, taking ten times the logarithm of both sides of Eq. 8 gives;

$$10 \log K = -20 \log P_S + 20 \log P_R + 20 \log 2D + 10 \alpha 2D \log e \quad (\text{Eq. 14})$$

which may be expressed as

$$BL = S_{PL} - E_{PL} - TL_S - TL_A \quad (\text{Eq. 15})$$

where:

BL = Bottom loss (in dB) and is equal to $-10 \log K$

S_{PL} = pressure level of the source pulse (in dB//1 dyne/cm²)
and is equal to $20 \log P_S$

E_{PL} = pressure level of the echo pulse (in dB//1 dyne/cm²) and is
equal to $20 \log P_R$

TL_S = spreading loss (in dB) and is equal to $20 \log 2D$

TL_A = attenuation loss (in dB) and is equal to $10 \alpha 2D \log e$

Finally taking Eq. 13 and stating it in dB gives:

$$10 \log K = 20 \log R \quad (\text{Eq. 16})$$

which may be expressed as:

$$BL = 20 \log R$$

(Eq. 17)

where;

BL = Bottom loss in dB

R = Rayleigh Reflection Coefficient

A-5 Core Site Locations

Core Site	Sample No.	d _w (ft)	Time (GMT)	Raydist Coordinates		Lambert Coordinates	
				Red	Green	x	y
A	1	40	1611	210.38	266.95	1439279.424	518634.575
	2	40	1631	210.42	266.98	1439274.959	518635.635
B	1	37	1724	202.13	261.29	1440507.802	518442.381
	2 ^{14/}						
C	1	32	1724	193.05	254.67	1441868.575	518126.137
	2	32	1748	192.62	254.96	1441927.754	518222.873
D	1	30	1830	186.02	251.12	1442911.054	518143.581
	2	31	1900	185.81	251.01	1442949.558	518145.261
E	1	26	1945	177.83	245.56	1444141.465	517888.568
	2	30	2124	177.79	244.55	1444159.179	517710.842
F	1	27	1706	176.46	259.04	1444304.657	520229.775
	2	27	1720	176.40	259.04	1444309.120	520230.355
G	1	28	1811	183.21	263.04	1443305.041	520380.028
	2	28	1821	183.24	263.04	1443300.518	520377.636
H	1	32	1759	191.39	268.02	1442097.923	520561.401
	2	32	1816	191.47	268.02	1442087.389	520557.192
I	1	31	1856	198.90	273.08	1440994.416	520792.279
	2	30	1918	198.97	273.07	1440982.243	520785.110
J	1	36	1802	205.70	276.42	1439982.869	520761.861
	2	37	1818	205.97	276.53	1439942.586	520756.106
K	1	42	1900	214.36	282.31	1438707.668	520986.808

^{14/} Bucket Sample

Core Site	Sample No.	d _w (ft)	Time (GMT)	Raydist Coordinates		Lambert Coordinates	
				Red	Green	x	y
L	1	39	1657	215.06	299.24	1438892.253	524055.829
	2	39	1711	215.02	299.19	1438900.723	524052.237
M	1	34	1751	206.07	293.92	1440217.857	523912.057
	2	34	1806	206.01	294.46	1440241.186	524020.239
N	1	34	1736	199.09	289.66	1441240.192	523752.573
	2	34	1750	199.04	289.65	1441251.291	523756.840
O	1	27	1833	191.11	284.07	1442385.654	523415.116
	2	27	1846	191.08	284.04	1442389.989	523414.000
P	1	26	2029	182.87	280.05	1443612.313	523356.853
	2	28	2047	182.70	280.03	1443639.124	523366.384

A-6 SEDIMENT SAMPLE PROCESSING SUMMARY AND RELATED ACOUSTIC DATA

Sample	Vol. Wet. Smpl. cc	Ga wet	Ga dry	Water. Cont. %	Void Ratio	Poros.	(Gravel) %	Coarse %	Medium Sand %	Fine Sand %	Silt (Silt & Clay) %	Clay %	Shell %
A-1 Top	3664	1.91	2.72	30.20	0.28	47.09			20.4	46.4	14.48	14.42	4.3
A-1 Middle				37.90					17.0	41.6	11.03	13.47	16.9
A-1 Bottom				39.10					23.88	35.51	15.01	10.28	15.32
A-2 Top	3520	2.00	2.74	29.90	.69	40.80			22.43	40.82	16.81	17.51	2.32
A-2 Middle				32.9					21.56	37.27	16.63	16.77	7.77
A-2 Bottom				37.1					23.34	31.26	13.86	15.27	16.27
B-1 Top	3137	1.94	2.72	29.1	.83	45.35			30.74	29.38	(4.65)	Comb silt-clay	35.23
B-1 Middle				32.3					37.25	17.38	(5.07)		40.29
B-1 Bottom				32.0					52.38	21.52	(8.48)		17.62
—													
C-1 Top	3542	1.96	2.80										
C-1 Middle				31.79	.88	46.67			70.25	11.97	(0.23)		17.55
C-1 Bottom				31.94					72.46	20.66	(0.21)		6.68
C-2 Top	3122	2.04	2.66	28.04					71.84	20.57	(0.28)		7.31
C-2 Middle				38.41	.50	37.35			54.37	37.38	(0.65)		7.37
C-2 Bottom				32.44					46.37	48.43	(0.89)		4.31
D-1 Top	3360	2.15	2.79	32.50					31.42	45.37	12.62	5.44	4.15
D-1 Middle				27.3	.56	35.75			57.71	21.58	(2.78)		17.93
D-1 Bottom				33.6			6.0		53.51	31.14	(4.96)		4.39
D-2 Top	3493	2.12	2.78	33.4					62.98	24.07	(2.75)		10.19
D-2 Middle				31.90	.59	37.08			71.11	16.38	(3.83)		8.66
D-2 Bottom				32.28					44.28	38.80	(7.86)		9.06
				33.04					19.02	54.00	9.30	15.31	2.37

Sample	Other	Nd mm	Q75 mm	Q25 mm	QD _a	QD _g (S _o)	Log10 S _o	Rayleigh Reflection Coefficient	Bottom Loss (dB)
A-1									
Top		0.20	0.26	0.024	0.1180	3.2914	1.1913		
Middle		0.21	0.35	0.076	0.1370	2.1460	0.7636	0.634	-3.96
Bottom		0.21	0.36	0.076	0.1420	2.1764	0.7777		
A-2									
Top		0.19	0.26	0.017	0.1190	3.8730	1.3540		
Middle		0.20	0.28	0.017	0.1315	4.0584	1.4008	0.634	-3.96
Bottom		0.22	0.36	0.019	0.1705	4.3529	1.4708		
B-1									
Top		0.40	1.20	0.230	0.4850	2.2842	0.8260		
Middle		0.46	1.30	0.265	0.5175	2.2149	0.7952	0.693	-3.19
Bottom		0.36	0.55	0.230	0.1600	1.5464	0.4359		
B-2									
Top									
Middle									
Bottom									
C-1									
Top		0.38	0.55	0.290	0.1300	1.3772	0.3200		
Middle		0.22	0.24	0.185	0.0300	1.1508	0.1404	0.607	-4.34
Bottom		0.33	0.40	0.270	0.0650	1.2172	0.1965		
C-2									
Top		0.29	0.38	0.230	0.0750	1.2854	0.2510		
Middle		0.26	0.36	0.210	0.0725	1.3002	0.2625		
Bottom		0.22	0.31	0.165	0.0725	1.3707	0.3153		
D-1									
Top		0.34	0.45	0.255	0.0975	1.3284	0.2840		
Middle		0.30	0.40	0.225	0.0925	1.7777	0.5753	0.648	-3.77
Bottom		0.32	0.41	0.250	0.0800	1.2806	0.2473		
D-2									
Top		0.33	0.42	0.270	0.0750	1.2469	0.2207		
Middle		0.27	0.39	0.185	0.1025	1.4519	0.3729	0.648	-3.77
Bottom		0.19	0.26	0.077	0.0915	1.8375	0.6084		

Sample	Vol. Wet. Smpl. cc	Ga wet	Ga dry	Water. Cont. %	Void Ratio	Poros.	Gravel %	Coarse %	Medium Sand %	Fine Sand %	Silt (Silt & Clay) %	Clay %	Shell %
E-1 Top	3454	1.77	2.78	34.04	1.31	56.74		4.23	4.06	8.33	37.99	32.03	
E-1 Middle				77.57				0.68	0.74	13.74	55.55	27.49	13.36
E-1 Bottom				86.27				0.48	6.01	23.54	32.43	36.67	1.00
E-2 Top	1696	1.79	2.73	36.79	1.19	54.34							0.87
E-2 Middle				69.27									
E-2 Bottom	Insufficient Sample												
F-1 Top	3697	1.64	2.70										
F-1 Middle				65.40	1.89	65.35			1.02	11.89	42.21	44.54	
F-1 Bottom				92.00						21.41	38.10	38.83	1.34
F-2 Top	3162	1.56	2.72	83.80					1.26	27.98	33.41	36.85	
F-2 Middle				82.80	2.07	67.44				24.31	33.79	41.48	
F-2 Bottom				100.00						33.32	29.27	36.10	
G-1 Top	3763	1.72	2.75	85.70						22.81	27.55	47.01	
G-1 Middle				78.90	1.43	58.86			0.92	14.50	18.19	64.48	1.01
G-1 Bottom				51.40					0.56	14.13	45.99	37.81	1.51
G-2 Top	2890	1.96	2.77	90.40						12.21	40.13	45.94	0.93
G-2 Middle				50.60	.84	45.76			0.78	19.16	31.64	40.87	7.55
G-2 Bottom				71.10					1.53	90.99	(4.08)		3.40
H-1 Top	3300	2.02	2.70	43.60					5.36	33.98	26.60	31.48	2.58
H-1 Middle				49.50	.67	40.00			6.16	59.26	14.74	17.11	2.73
H-1 Bottom				67.19					14.86	75.11	(5.80)		4.23
H-2 Top	3592	1.79	2.71	38.35					2.65	32.92	29.31	32.79	2.33
H-2 Middle													
H-2 Bottom				34.44	1.16	53.80			14.87	56.09	(2.87)		26.18
				24.50					9.99	50.16	10.35	14.39	15.11
				49.78					2.36	82.41	(8.68)		6.54

Sample	Other	Md mm	Q ₇₅ mm	Q ₂₅ mm	QD _a	QD _g (So)	Log10 So	Rayleigh Reflection Coefficient	Bottom Loss (dB)
E-1									
Top		0.022	0.175	0.0015	0.0867	10.8012	2.3796		
Middle		0.028	0.066	0.0013	0.0323	7.1252	1.9636	0.788	-2.07
Bottom		0.017	0.175	0.0014	0.0868	11.1803	2.4142		
E-2									
Top									
Middle									
Bottom									
F-1									
Top	0.34	0.0082	0.049	0.0017	0.0236	5.3687	1.6805		
Middle	0.32	0.0135	0.096	0.0018	0.0471	23.0940	3.1396	0.773	-2.23
Bottom	0.50	0.026	0.115	0.0013	0.0568	9.4053	2.2413		
F-2									
Top	0.42	0.0082	0.074	0.0012	0.0364	7.8528	2.0609		
Middle	2.31	0.0175	0.100	0.0018	0.0491	7.4535	2.0087	0.773	-2.23
Bottom	2.63	0.0105	0.074	0.0013	0.0364	7.5447	2.0209		
G-1									
Top		0.0025	0.0098	0.0009	0.0045	3.3371	1.2051		
Middle		0.0127	0.055	0.0007	0.0272	8.8641	2.1820	0.741	-2.60
Bottom	0.79	0.0087	0.046	0.0007	0.0229	8.1504	2.0981		
G-2									
Top		0.0150	0.147	0.0009	0.0731	13.0740	2.5706		
Middle		0.2150	0.280	0.1750	0.0525	1.2649	0.2350	0.741	-2.60
Bottom		0.0490	0.215	0.0022	0.1071	15.9041	2.7666		
H-1									
Top		0.2400	0.360	0.0130	0.1735	5.2623	1.6606		
Middle		0.290	0.390	0.2050	0.0925	1.3792	0.3215	0.646	-3.80
Bottom		0.0275	0.197	0.0012	0.0979	13.0883	2.5717		
H-2									
Top		0.370	1.200	0.2650	0.4675	2.1279	0.7551		
Middle		0.265	0.417	0.0780	0.1695	2.3121	0.8382	0.646	-3.80
Bottom		0.220	0.315	0.1700	0.0725	1.3612	0.3084		

Sample	Vol. Wet. Smpl. CC	Ga wet	Ga dry	Water. Cont. %	Void Ratio	Poros. %	Gravel %	Coarse %	Medium Sand %	Fine Sand %	Silt (Silt & Clay) %	Clay %	Shell %
I-1	3664	1.95	2.74										
Top				34.66	.83	45.40			6.70	51.90	14.11	23.15	4.14
Middle				39.15					5.67	67.63	8.47	13.83	4.40
Bottom				47.12					1.51	39.35	25.25	26.87	7.33
I-2	3544	1.72	2.74										
Top				49.10	1.42	58.62			8.39	63.94	8.27	11.24	8.18
Middle				33.71				1.96	9.13	70.55	6.66	9.58	2.11
Bottom				39.06					7.59	58.25	7.88	12.51	13.77
J-1	3686	1.99	2.72										
Top				27.72	.74	42.44			12.37	57.99	(5.24)	24.41	
Middle				31.90					13.14	53.79	9.68	13.62	9.77
Bottom				37.07					2.36	58.35	14.03	18.45	6.79
J-2	3818	1.92	2.75										
Top				29.20	.90	47.43			8.15	63.00	10.85	11.91	6.11
Middle				41.06					4.83	65.73	11.34	13.82	4.26
Bottom				45.30					8.52	51.19	11.09	12.67	16.54
K-1	3890	1.81	2.69										
Top				28.49	1.09	52.07			4.14	65.91	7.99	12.26	9.71
Middle				40.77					0.47	68.51	12.38	16.04	2.58
Bottom				40.54				1.43	0.36	73.65	14.01	10.53	
K-2													
L-1	3874	1.88	2.75										
Top				32.45	.99	49.71			2.23	65.59	10.12	14.10	7.97
Middle				45.98					3.05	61.20	9.88	13.35	12.52
Bottom				46.16						76.94	8.05	12.57	2.43
L-2	3868	1.88	2.75										
Top				39.08	.99	49.71			2.86	66.09	7.97	11.48	11.59
Middle				46.09					12.22	62.29	7.00	12.12	5.35
Bottom				42.14				0.36	0.90	83.99	5.42	8.16	1.16

Sample	Other	Mid mm	Q75 mm	Q25 mm	QD _a	QD _g (S ₀)	Log10 S ₀	Rayleigh Reflection Coefficient	Bottom Loss (dB)
I-1 Top		0.255	0.370	0.1470	0.1115	1.5865	0.4615		
I-1 Middle		0.270	0.365	0.1770	0.0940	1.4360	0.3619	0.616	-4.21
I-1 Bottom		0.240	0.390	0.1400	0.1250	1.6690	0.5122		
I-2 Top		0.2500	0.375	0.1600	0.1075	1.5309	0.4259		
I-2 Middle		0.2700	0.360	0.1800	0.0900	1.4142	0.3466	0.616	-4.21
I-2 Bottom		0.2770	0.390	0.1480	0.1210	1.6233	0.4845		
J-1 Top		0.3500	1.115	0.2400	0.4375	2.1554	0.7680		
J-1 Middle		0.2050	0.350	0.1050	0.1225	1.8257	0.6020	0.622	-4.12
J-1 Bottom		0.1000	0.300	0.0165	0.1418	4.2640	1.4502		
J-2 Top		0.2300	0.350	0.1170	0.1165	1.7296	0.5479		
J-2 Middle		0.2070	0.312	0.0600	0.1260	2.2804	0.8243	0.622	-4.12
J-2 Bottom		0.2350	0.417	0.1050	0.1560	1.9928	0.6896		
K-1 Top		0.204	0.320	0.130	0.0950	1.5689	0.4504		
K-1 Middle		0.170	0.226	0.056	0.0852	2.0089	0.6976	0.635	-3.94
K-1 Bottom		0.155	0.195	0.075	0.0595	1.6018	0.4711		
K-2 Top									
K-2 Middle									
K-2 Bottom									
L-1 Top		0.167	0.232	0.080	0.0760	1.7029	0.5323		
L-1 Middle		0.193	0.310	0.105	0.1025	1.7182	0.5413	0.646	-3.80
L-1 Bottom		0.197	0.270	0.120	0.0750	1.5000	0.4055		
L-2 Top		0.190	0.295	0.120	0.0875	1.5679	0.4497		
L-2 Middle		0.220	0.360	0.120	0.1200	1.7321	0.5493	NG	
L-2 Bottom		0.195	0.222	0.160	0.0310	1.1779	0.1638		

Sample	Vol. Wet. Smp l. cc	Ga wet	Ga dry	Water. Cont. %	Void Ratio	Poros.	Gravel %	Coarse %	Medium Sand %	Fine Sand %	Silt (Silt & Clay) %	Clay %	Shell %
M-1	3875	1.93	2.75										
Top				32.06	.88	46.89			15.38	46.25	6.97	9.98	21.42
Middle				38.39				2.90	5.02	64.93	9.05	10.61	7.49
Bottom				32.06					3.14	61.94	8.41	12.27	14.24
M-2	3881	1.97	2.80										
Top				26.50	.86	46.11			9.65	45.89	6.85	14.55	23.05
Middle				41.66					5.61	64.17	6.27	9.72	14.22
Bottom				33.66					3.11	58.18	20.15	28.48	15.75
N-1	3614	1.94	2.77										
Top				30.68	.88	46.89			6.48	50.23	6.75	11.42	25.13
Middle				46.36					0.60	52.72	20.77	22.31	3.58
Bottom				59.15					0.94	72.84	12.40	13.50	2.31
N-2	3554	1.81	2.75										
Top				34.67	1.16	53.71			8.30	59.56	4.94	6.03	21.16
Middle				48.10						40.58	28.31	30.01	1.08
Bottom				54.72					0.25	58.08	19.89	21.26	0.53
O-1	3879	1.71	2.73										
Top				85.37	1.44	58.96				50.69	17.90	31.39	
Middle				63.43						48.18	19.10	32.18	0.53
Bottom				82.08						45.17	26.99	27.43	
O-2													
Top													
Middle													
Bottom													
P-1													
Top													
Middle													
Bottom													
P-2	3492	1.51	2.82										
Top				87.08	2.55	71.82							
Middle				127.25									
Bottom				101.57									
										36.91	(62.41)		0.67
										19.10	(79.51)		1.38

Sample	Other	Md mm	Q75 mm	Q25 mm	QDa	QDg (So)	Log10 So	Rayleigh Reflection Coefficient	Bottom Loss (dB)
M-1									
Top		0.310	0.450	0.170	0.1400	1.6270	0.4867		
Middle		0.202	0.375	0.120	0.1275	1.7678	0.5697	0.553	-5.15
Bottom		0.205	0.340	0.116	0.1120	1.7120	0.5377		
M-2									
Top		0.270	0.900	0.120	0.3900	2.7386	1.0074		
Middle		0.205	0.365	0.142	0.1115	1.6031	0.4719	0.553	-5.15
Bottom		0.205	0.355	0.107	0.1240	1.8214	0.5996		
N-1									
Top		0.245	1.20	0.15	0.5250	2.8284	1.0397		
Middle		0.11	0.188	0.01	0.0890	4.3359	1.4569	0.616	-4.21
Bottom		0.20	0.295	0.095	0.1000	1.7622	0.5665		
N-2									
Top		0.275	0.75	0.18	0.2850	2.0412	0.7136		
Middle		0.028	0.135	0.003	0.0660	6.7082	1.9033	0.616	-4.21
Bottom		0.16	0.21	0.01	0.1000	4.5826	1.5223		
O-1									
Top	0.38	0.08	0.18	0.0025	0.0888	8.4853	2.1383		
Middle		0.065	0.15	0.065	0.0425	1.5191	0.4181	0.607	-4.34
Bottom	0.41	0.04	0.16	0.0038	0.0781	6.4889	1.8701		
O-2									
Top									
Middle	Not completed								
Bottom									
P-1									
Top									
Middle								0.742	-2.59
Bottom									
P-2									
Top									
Middle									
Bottom									